| Title | Computational Materials Design of d0 Ferromagnets |
|---|---|
| Author(s) | Seike, Masayoshi |
| Citation | 大阪大学, 2012, 博士論文 |
| Version Type | VoR |
| URL | https://hdl.handle.net/11094/2523 |
| rights | |
| Note | |

# Computational Materials Design of $d^0$ Ferromagnets

A dissertation submitted to
THE GRADUATE SCHOOL OF ENGINEERING SCIENCE
OSAKA UNIVERSITY
in partial fulfillment of the requirements for the degree of
DOCTOR OF PHILOSOPHY IN SCIENCE

BY

MASAYOSHI SEIKE

MARCH 2012

## Abstract

$d^0$ ferromagnetism refers to a new class of magnetism, wherein the ferromagnets contain no magnetic elements, and has created significant interest in dilute magnetic semiconductors (DMSs). Based on first-principles calculations, this study demonstrates that materials such as Si- or Ge-doped $K_2S$ and C- or N-doped CaO, MgO, or SrO can exhibit ferromagnetism. Thereafter, experimental work has validated that ferromagnetic behavior is exhibited by N-doped MgO. In addition, Monte Carlo simulations of the dopant distribution based on the calculated chemical pair interactions between dopants revealed that Mg(O,N), Ca(O,N), Sr(O,N) and (Mg,$V_{Mg}$)O can form nanoscale super-paramagnetic clusters of dopants with strong ferromagnetic coupling in the clusters, and these materials can exhibit high blocking temperatures (high-$T_B$). Furthermore, by considering estimated Curie temperatures under a condition of homogeneous dopant distribution, the room-temperature magnetic hysteresis in MgO thin films with 13% N impurities and a few percent of Mg vacancies observed in previous experimental reports is shown to originate from the super-paramagnetic blocking phenomenon resulting from self-organized nanostructures. Finally, this study reveals that the origin of $d^0$ ferromagnetism can be understood as follows: local magnetic moments are spontaneously formed by narrow $p$ bands, and the ferromagnetic states are stabilized due to the kinetic energy gain from itinerant spin-polarized electrons, which result from the partial occupation of the $p$ bands. The significance of this study is in (i) pioneering the computational materials design of $d^0$ ferromagnets, which has greatly contributed to developments in this novel research field, (ii) presenting the materials design of $d^0$ ferromagnets to achieve high-$T_B$ and (iii) elucidating the magnetic properties and mechanisms associated with $d^0$ ferromagnetism. These research outcomes not only provide an essential understanding of $d^0$ ferromagnetism but also open a new route to create environmentally friendly materials for spintronics without the use of magnetic elements.

# Contents

Contents

# Chapter 1

# Introduction

## 1.1 Computational Materials Design of Dilute Magnetic Semiconductors (DMSs)

Semiconductor-based spintronics are the next generation of electronics and aim to manipulate both the charge and spin degrees of freedom of electrons in semiconducting devices in an integrated manner [1]. Semiconductor spintronics as a practical technology was triggered by the discovery of ferromagnetism in dilute magnetic semiconductors (DMSs), such as Mn-doped InAs [2] or GaAs [3]. DMSs are traditionally defined as semiconductors that exhibit magnetism due to the presence of magnetic impurities of transition or rare-earth metals. Because manipulation of electron spin in semiconducting devices can improve conventional semiconductor technology, semiconductor spintronics are expected to become a new technology with advantages such as non-volatility, increased data processing speed, increased integration density and decreased power consumption.

Computational materials design (CMD) based on first-principles calculations has been an important building block in this field. One of the primary goals in the field is to develop a ferromagnetic semiconductor wherein the local magnetic moments are ordered well above room temperature. In the most frequently cited work, Dietl et al. systematically estimated the Curie temperatures ($T_C$s) in various Mn-doped semiconductors and proposed that wide-bandgap semiconductors such as GaN and ZnO are suitable host materials for ferromagnetic DMSs with high $T_C$ [4]. Sato and Katayama-Yoshida also presented beneficial CMDs of novel II-VI-based DMSs (ZnO [5, 6], ZnS [7], ZnSe [7], ZnTe [7]) and III-V-based DMSs (GaN [8, 9], GaP [8], GaAs [9], GaSb[8]) doped with $3d$ transition metals (TMs) [10]. Many of their CMDs were experimentally validated; i.e., ferromagnetism was observed in designed DMSs, such as (Zn,Co)O [11],

(Zn,V)O [12], (Zn,Cr)Te [13] and (Ga,Cr)N [14].

Thereafter, a more accurate framework has been presented for the estimation of $T_C$. In the traditional picture of exchange interaction in DMS materials, exchange interactions are treated as long-range interactions [4, 7, 8, 9]. In those early studies, $T_C$s of DMSs were estimated based on the mean field approximation (MFA). However, in calculations based on density functional theory (DFT), for most DMSs, the exchange interactions were observed to be much more short-ranged, and also reflected the orbital character of the atoms composing the lattice. The MFA greatly overestimates $T_C$ for such DMSs where the exchange interactions are short-ranged and the impurity concentration is smaller than the magnetic percolation limit. The reason for the overestimation is that, in this approximation, all exchange interactions are counted as significant interactions, regardless of whether they are strong enough to contribute to the $T_C$ under thermal fluctuations. To abandon the mean-field description and account for the percolation effect, the so-called two-step approach was presented for the estimation of $T_C$ [15, 16, 17]. In this framework, first, the effective exchange coupling constants are calculated based on a first-principles calculation using Liechtenstein's formula [18]. Second, using the calculated exchange interactions, the $T_C$s are estimated using Monte Carlo (MC) simulations [19]. The $T_C$s estimated by the two-step approach were observed to be lower than those estimated by the MFA, and good agreement was obtained between theory and experiments in DMSs such as (Ga,Mn)As [16, 17, 20].

The $T_C$s of DMSs reported by different experimental groups are often in disagreement. For instance, the $T_C$ of ferromagnetic (Ga,Mn)N samples was observed to be in the range of 220 to 940 K [21, 22]. However, paramagnetic behavior of (Ga,Mn)N samples has also been reported [23, 24]. Some of the heterogeneity may be explained by clustering of the dopant magnetic elements in the host materials which exhibit super-paramagnetic behavior with relatively high blocking temperature (high-$T_B$), even at small impurity concentrations [25, 26, 27, 28]. In general, DMS systems undergo phase separation at thermal equilibrium due to a solubility gap, and thus, DMS systems can be created experimentally by using nonequilibrium crystal growth techniques. This fact implies that when significant attractive interactions exist between impurities, the homogeneity may be an unrealistic assumption, depending on the experimental conditions. In fact, inhomogeneous impurity distributions have been observed in several DMS systems, such as (Ga,Cr)N [29], (Al,Cr)N [29], (Ga,Mn) [30] and (Zn,Cr)Te [31]. This inhomogeneous impurity distribution is now used not only to explain the discrepancies between experiments but also to enhance the blocking temperature ($T_B$) or $T_C$. When super-paramagnetic clusters are formed via spinodal decomposition, a super-

paramagnetic blocking phenomenon has been shown to dominate the magnetization process, and a high-$T_B$ can be realized even at low impurity concentrations, such as 5%. In addition, at high impurity concentrations, such as above 20%, a network of percolating clusters can enhance the $T_C$, which holds promise to create DMS materials with room-temperature ferromagnetism [25, 26, 27, 28].

Because strongly correlated systems, such as wide-bandgap materials, are often used as hosts for DMSs, it is worth noting the importance of the self-interaction correction for their electronic structure calculations. For a wide variety of materials, the local density approximation (LDA) provides reasonable predictions. However, it often fails to predict the electronic structure of strongly correlated systems, such as ZnO [32]. This error arises mostly from self-interaction, which results from the LDA of the exchange-correlation potential and refers to the fictitious interaction of an electron charge with the Columbic and exchange-correlation potential generated by the same electron. The error can be significantly improved by introducing a simple correction called the pseudopotential-like self-interaction correction (pseudo-SIC or PSIC) to the LDA calculation scheme [32, 33, 34] (see Appendix for more details).

## 1.2    $d^0$ Ferromagnets

Is it possible to create DMSs without using a 3$d$ TM? To answer this question, we conducted an investigation based on first-principles calculations. In general, a local magnetic moment cannot be induced by 4$d$- or 5$d$-TM doping due to excessive hybridization between the 4$d$ or 5$d$ orbital of the impurities and the orbital of a host material. We initially determined that DMSs can be created in 4$d$-TM-doped $K_2S$ using cationic substitutions [35, 36]. Our calculation showed that the 4$d$ orbital can be used to create local magnetic moments and that ferromagnetic states can be stabilized by Zener's double exchange mechanism in $K_2S$. This process involves narrowing of the partially filled impurity bands by the use of the large lattice spacing of the host material [35, 36]; this idea was generalized and applied to 4$d$- or 5$d$-TM-doped alkaline chalcogenides [37, 38].

After the discovery that spatially broad orbitals, such as 4$d$ and 5$d$ orbitals, can create local magnetic moments, we speculated that $p$ bands may spontaneously polarize to provide a ferromagnetic state. Following this speculation, we theoretically demonstrated the existence of $p$ bands in $K_2(S,Si)$ and $K_2(S,Ge)$ in which deep impurity bands consisting of 3$p$ orbitals were introduced in the bandgap with partially filled 3$p$ shells stabilizing a ferromagnetic state [39]. This principle was applied to 2$p$ orbitals

in Ca(O,C) and Ca(O,N) [40].  Furthermore, many DMSs containing no magnetic elements, such as alkaline-chalcogenide- [41], alkaline-earth-chalcogenide- [41, 42, 43], SiO$_2$- [44] and diamond-based [45] $d^0$ ferromagnets, were similarily designed.

This new class of magnetism has been called $d^0$ ferromagnetism [46] and has attracted significant interest in the field of DMSs [47, 48, 49].  For example, after our aforementioned series of CMD of $d^0$ ferromagnets, many experimental works also reported the existence of ferromagnetism in materials such as N-doped MgO [50], C- or N-doped ZnO [51, 52], HfO$_2$ [53], TiO$_2$ [54], In$_2$O$_3$ [54], ZnO [54] and SnO$_2$ [55].

Although significant works have demonstrated the potential route to $d^0$ ferromagnetism, the origin of the magnetism is not yet fully understood.  In particular, most of the theoretical studies on $d^0$ ferromagnetism have assumed that the distribution of dopants in a system is homogeneous, and the potential contribution of phase separation has not been investigated.

In this thesis, a series of materials designs of $d^0$ ferromagnets as well as a unified picture of the mechanism for $d^0$ ferromagnetism are presented based on first-principles calculations [20].  In the following chapters, starting with an introduction of the CMD of non-3$d$-TM-doped DMSs [35, 36, 37, 38] that foreshadows the later CMD of $d^0$ ferromagnets, the pioneering CMDs of $d^0$ ferromagnets presented in 2004 [39, 40, 41] and the latest comprehensive analysis of magnetic properties in alkaline-earth-metal-oxide-based $d^0$ ferromagnets [56, 57, 58] are reviewed.  The potential contributions of phase separation and the formation of ferromagnetic clusters are also discussed.

# Chapter 2

# Materials Design of Non-3$d$-Transition-Metal-Doped DMSs

In this chapter, the CMD of non-3$d$-TM-doped DMSs [35, 36, 37, 38] is reviewed. The important discovery made in this review, which led to the later design of $d^0$ ferromagnets, is that spatially broad orbitals, such as 4$d$ and 5$d$ orbitals, can create local magnetic moments. Compliance with the splitting condition, defined as $U \geq W$, is an important guideline for the formation of a localized magnetic moment in materials without 3$d$ TM elements. $U$ is the effective correlation energy caused by the intra-atomic Coulomb repulsion in the localized orbital of magnetic sites, and $W$ is the bandwidth responsible for the formation of the magnetic moment. The effective correlation energy is defined as $U = E(N+1) + E(N\text{-}1) - 2E(N)$, where $E(N)$ is the total energy of the states in the bands with $N$ electrons. The hybridization of the 4$d$ or 5$d$ orbital of the impurities with an orbital of the host material is known to be much larger than that of the 3$d$ TM in semiconductors since the 4$d$ and 5$d$ orbitals are more delocalized than the 3$d$ orbital. Thus, optimizing the splitting condition in the CMD of materials without 3$d$ TM elements is critical.

## 2.1 4$d$- or 5$d$-Transition-Metal-Doped Alkaline Chalcogenides

The large magneto-optical effect is expected in non-3$d$-TM-doped DMSs since the spin-orbit coupling in the ferromagnetic states exhibted by 4$d$ and 5$d$ TMs is larger than that exhibited by 3$d$ TMs. Such ferromagnetic materials that exhibit a large

magneto-optical effect are beneficial for the application of magneto-optical devices to semiconductor spintronics since 3$d$ TMs are used in most DMSs. However, in general, a local magnetic moment cannot be induced by 4$d$- or 5$d$-TM doping because of excessive hybridization between the 4$d$ or 5$d$ orbital of the impurities and an orbital of the host material. For instance, in GaN and ZnO, which are popular host materials for the study 3$d$-TM-doped DMSs, a non-magnetic solution is obtained for many 4$d$-TM doped DMSs over a wide range of impurity concentrations (5 $\sim$ 25%) due to excessive $p$-$d$ hybridization between the impurity 4$d$ orbital and the ligand 2$p$ orbital of N or O.

To create local magnetic moments by non-3$d$-TM doping, the impurity band should be designed to be narrow in the bandgap in order to satisfy the splitting condition ($U \geq W$), which can be optimized by changing the lattice spacing and impurity concentration. Alkaline chalcogenides of I$_2$-VI compounds with an anti-CaF$_2$ structure (Fig. 2.1) can be used for this purpose. Alkaline chalcogenides have large lattice spacing due to the large ionic radius of their cations and are often transparent wide-bandgap semiconductors. Figure 2.2 presents the experimental lattice constants and calculated bandgaps of these compounds (the method used to determine these values is described in the next section). It should be noted that calculated bandgaps tend to be smaller (often by approximately 30%) than the experimentally determined bandgaps. Since these compounds have large lattice spacing and wide bandgap, a narrow non-3d-impurity band in the bandgap can be achieved. Hereafter, we will discuss how local magnetic moments are created and how a ferromagnetic state is stabilized in non-3$d$-TM-doped alkaline chalcogenides.
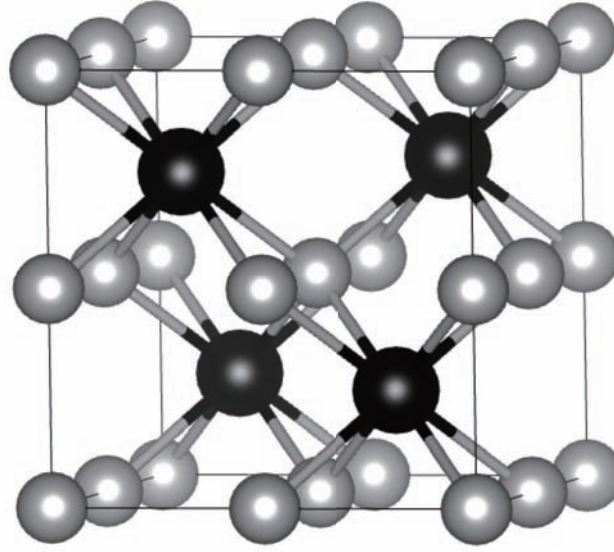
Figure 2.1: Atomic configuration of the anti-CaF$_2$ structure. Large and small spheres represent anions and cations, respectively. The VESTA visualization program [59] was used to prepare this image.
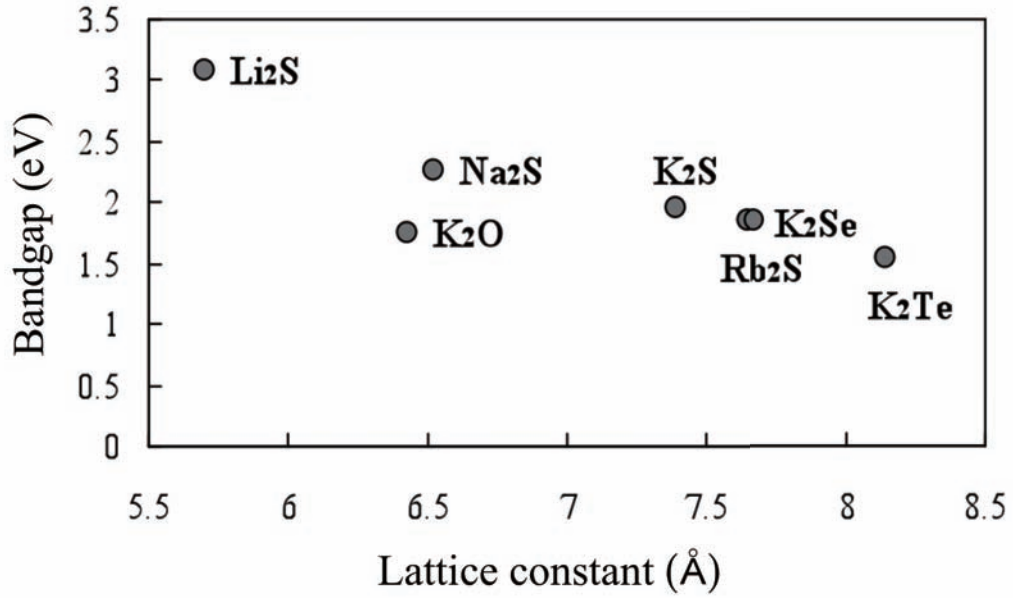


Figure 2.2: Experimental lattice constants and calculated bandgaps of alkaline chalcogenides.

## 2.2   Formation of Local Magnetic Moments

The stability of local magnetic moments was evaluated through the calculation of electronic structures based on first-principles. The first-principles calculations in this chapter were performed using the Korringa-Kohn-Rostoker coherent potential approximation (KKR-CPA) [60, 61] within the context of local density approximation (LDA). The KKR-CPA can be conveniently applied to describe the configuration average of a homogeneously disordered system in which magnetic impurities are randomly distributed. The MACHIKANEYAMA [62], KKR-CPA-LDA package, was used. The experimentally determined lattice constants of the $K_2O$, $K_2S$, $K_2Se$, $K_2Te$, $Li_2S$, $Na_2S$, and $Rb_2S$ host materials (a = 6.44, 7.39, 7.68, 8.15, 5.71, 6.53 and 7.65 Å, respectively), which have an anti-$CaF_2$ structure, were used. Lattice relaxation and the Jahn-Teller-distortion mechanism were not taken into account. Finally, the form of the potential was restricted to the muffin-tin type.

The present calculation showed that 4d-TM-doped alkaline chalcogenides of $K_2O$, $K_2S$, $K_2Se$, $K_2Te$, $Na_2S$ (except Zr-doped $Na_2S$) and $Rb_2S$ formed local magnetic moments and that even 5d TMs could create moments in some materials such as $(K,Ta)_2S$ and $(K,Os)_2S$. The density of states (DOS) of the $K_2S$-based systems are shown in Figs. 2.3 - 2.7. The $d\varepsilon$ orbital $(xy, yz, zx)$ of the TMs hybridized strongly with the $p$ orbital of anions in anti-$CaF_2$ I-VI compounds with $T_d$ symmetry and also formed bonding states in the valence band. In addition, the anti-bonding ($t^a$) impurity-band was pushed up into the band-gap. The $d\gamma$ orbital $(3z^2 - r^2, x^2 - y^2)$ also weakly hybridized with the $s$ orbital of the cations and, as a result, formed the bonding and anti-bonding states. The exchange-splitting energy between a majority (up) and minority (down) spin state was larger than the crystal field splitting between the weakly anti-bonding $e^a$ states and the anti-bonding $t^a$ states, which resulted in high-spin ground states. A localized magnetic moment, consisting of the merged $e^a$ and $t^a$ states was created at the impurity site under the splitting condition $(U \geq W)$. With decreasing lattice constants, the hybridization between the $d$ orbital of the impurities and an orbital of the host material increased in strength, and the $d$-impurity bandwidth widened (Fig. 2.8). When the lattice spacing was insufficient, as was the case for $Li_2S$, a local magnetic moment could not be formed by the non-3d-TM doping.

Figure 2.3: Total (solid lines) and partial (dotted lines) densities of states of (a) $(K,Zr)_2S$ and (b) $(K,Hf)_2S$. Impurity concentration is 5%.

12
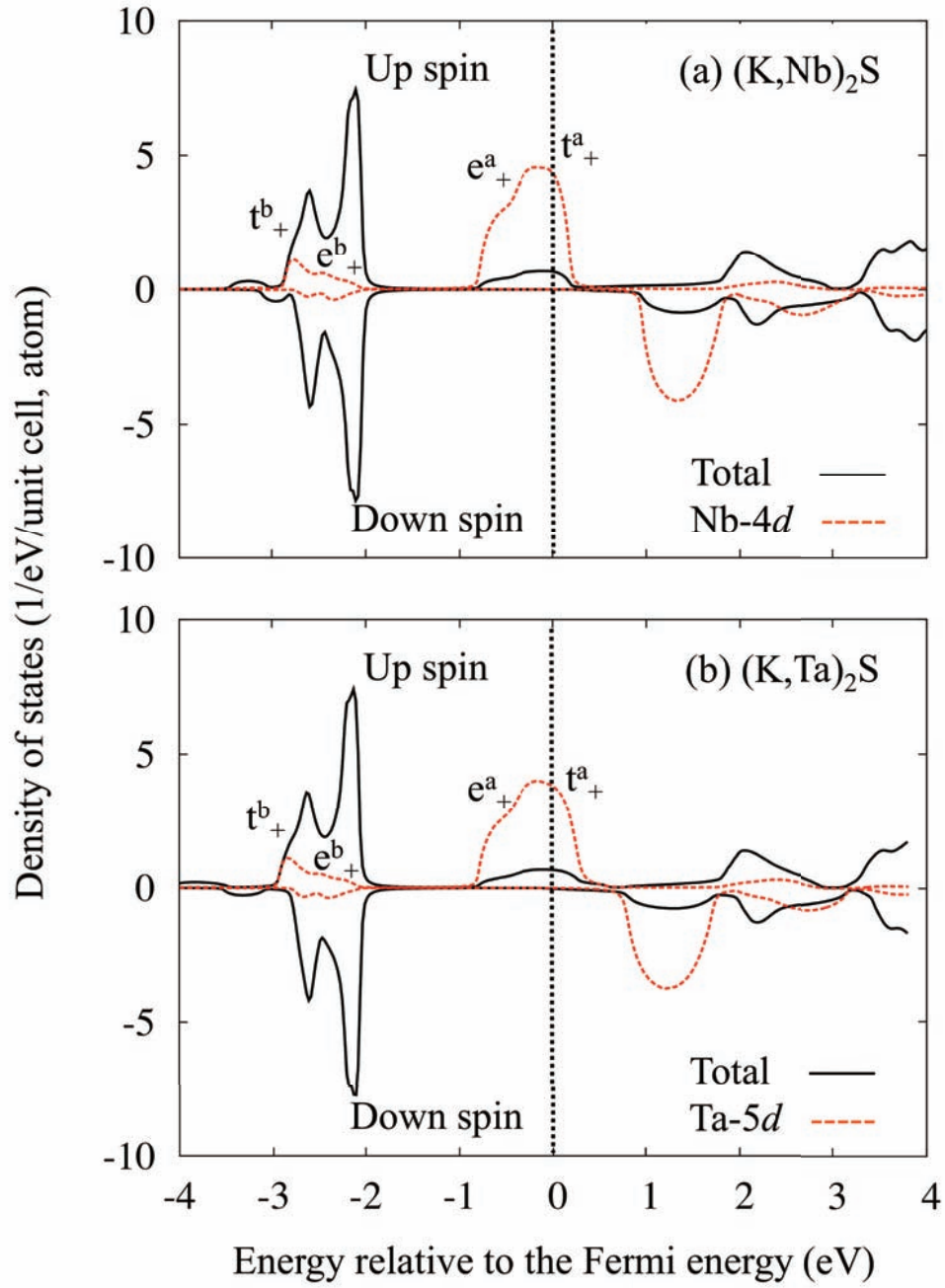
Figure 2.4:  Total (solid lines) and partial (dotted lines) densities of states of (a) (K,Nb)$_2$S and (b) (K,Ta)$_2$S. Impurity concentration is 5%.
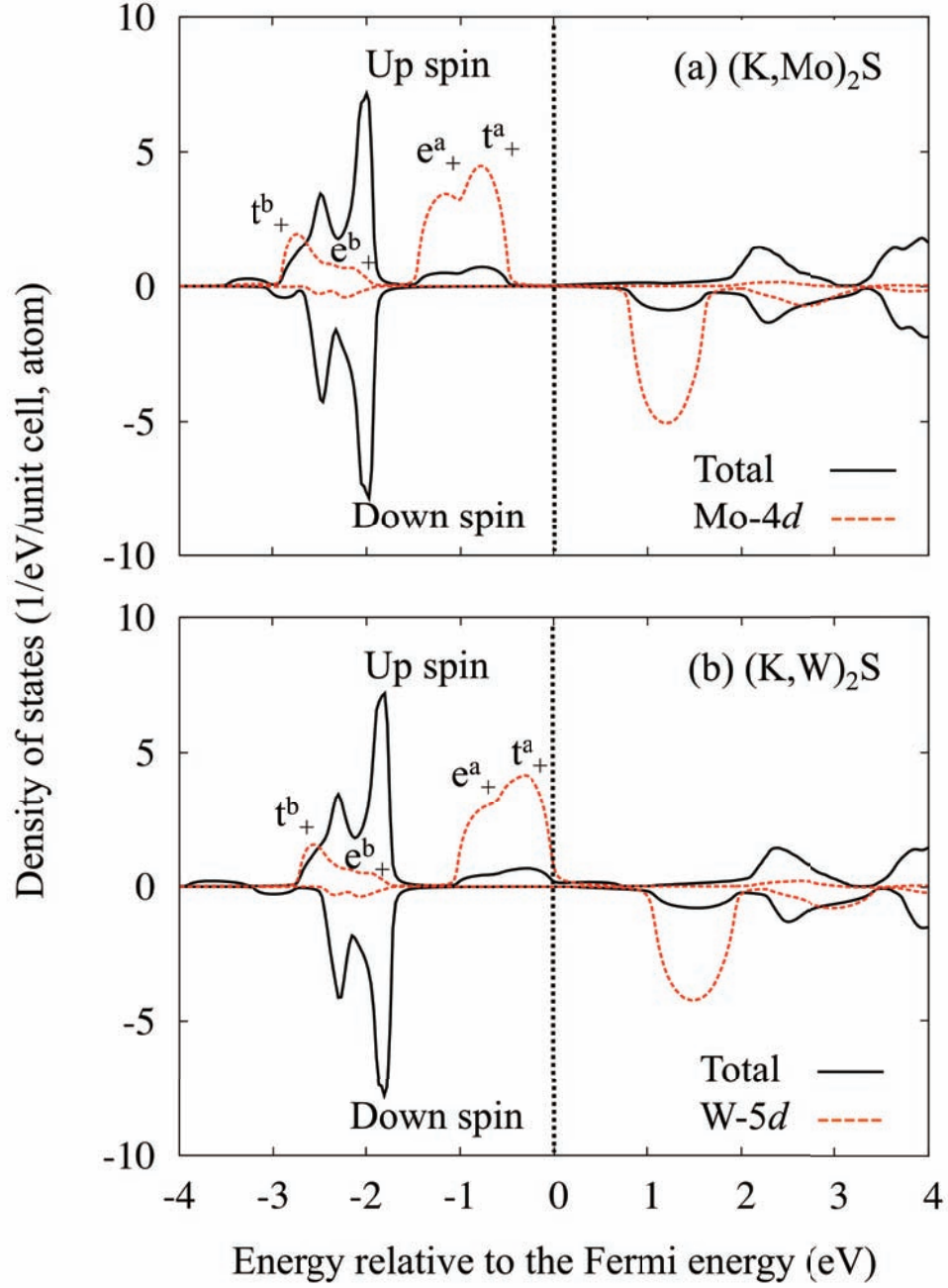
Figure 2.5: Total (solid lines) and partial (dotted lines) densities of states of (a) $(K,Mo)_2S$ and (b) $(K,W)_2S$. Impurity concentration is 5%.
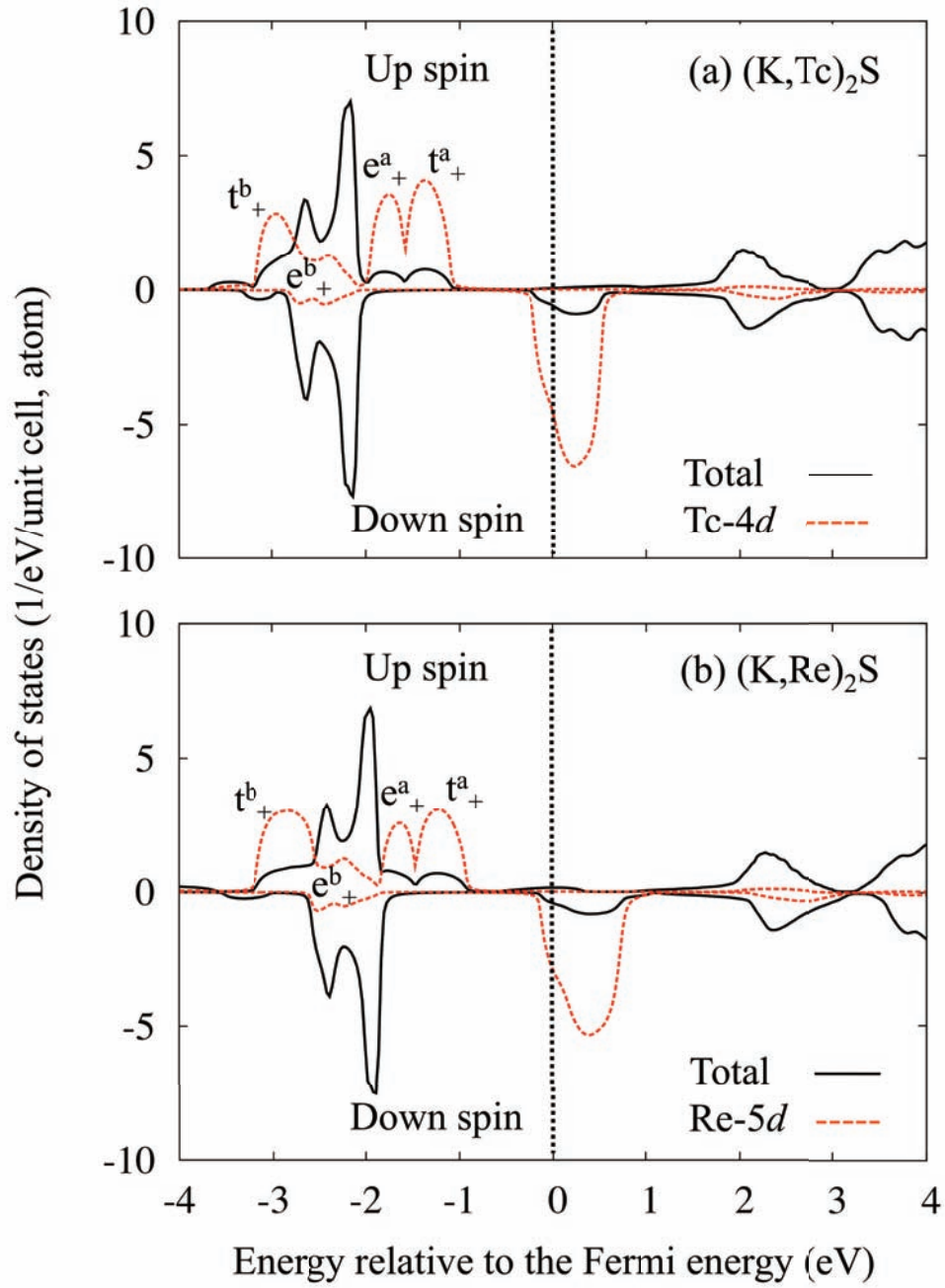
Figure 2.6: Total (solid lines) and partial (dotted lines) densities of states of (a) $(K,Tc)_2S$ and (b) $(K,Re)_2S$. Impurity concentration is 5%.
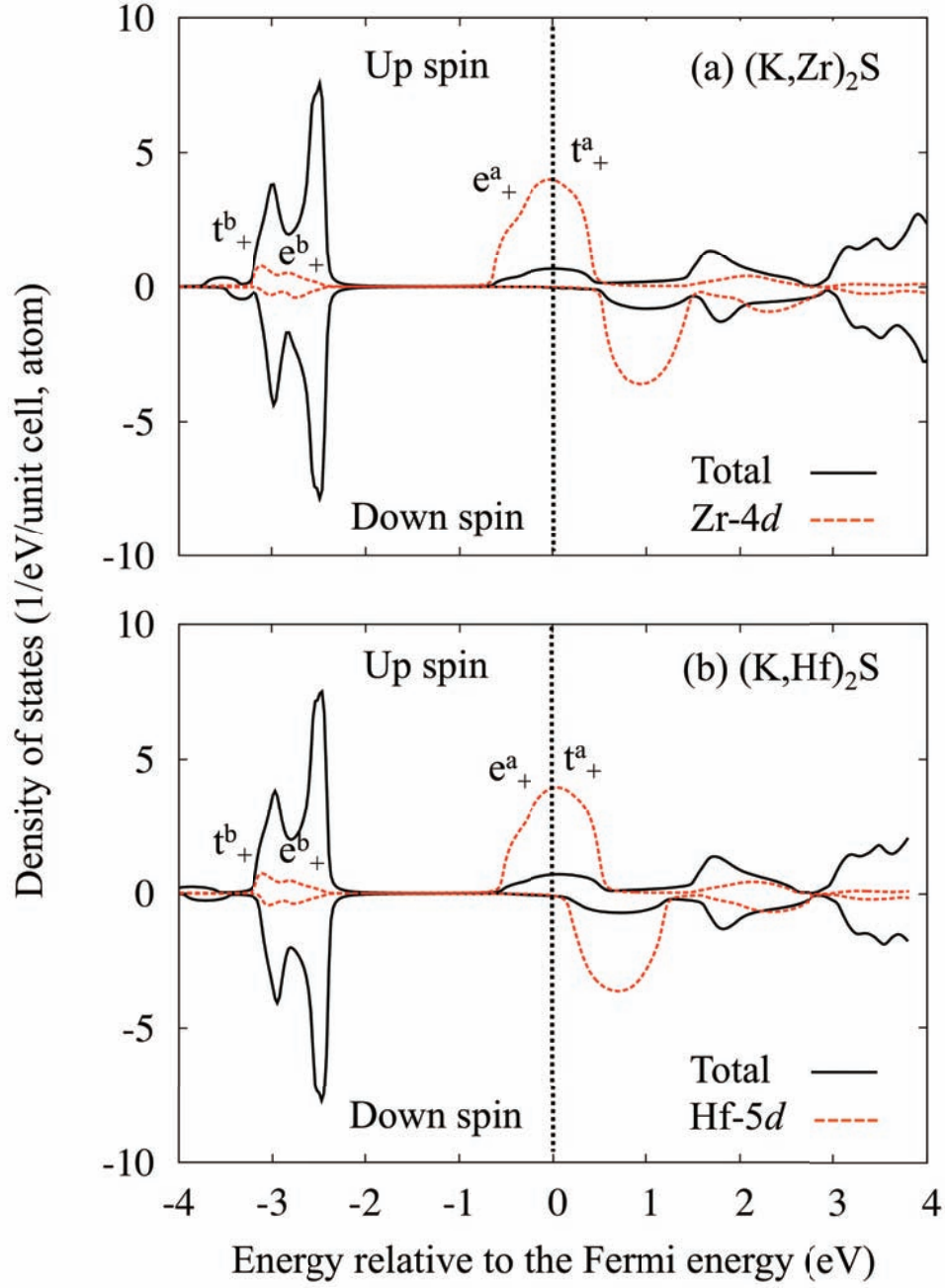
Figure 2.7: Total (solid lines) and partial (dotted lines) densities of states of (a) (K,Ru)$_2$S and (b) (K,Os)$_2$S. Impurity concentration is 5%.
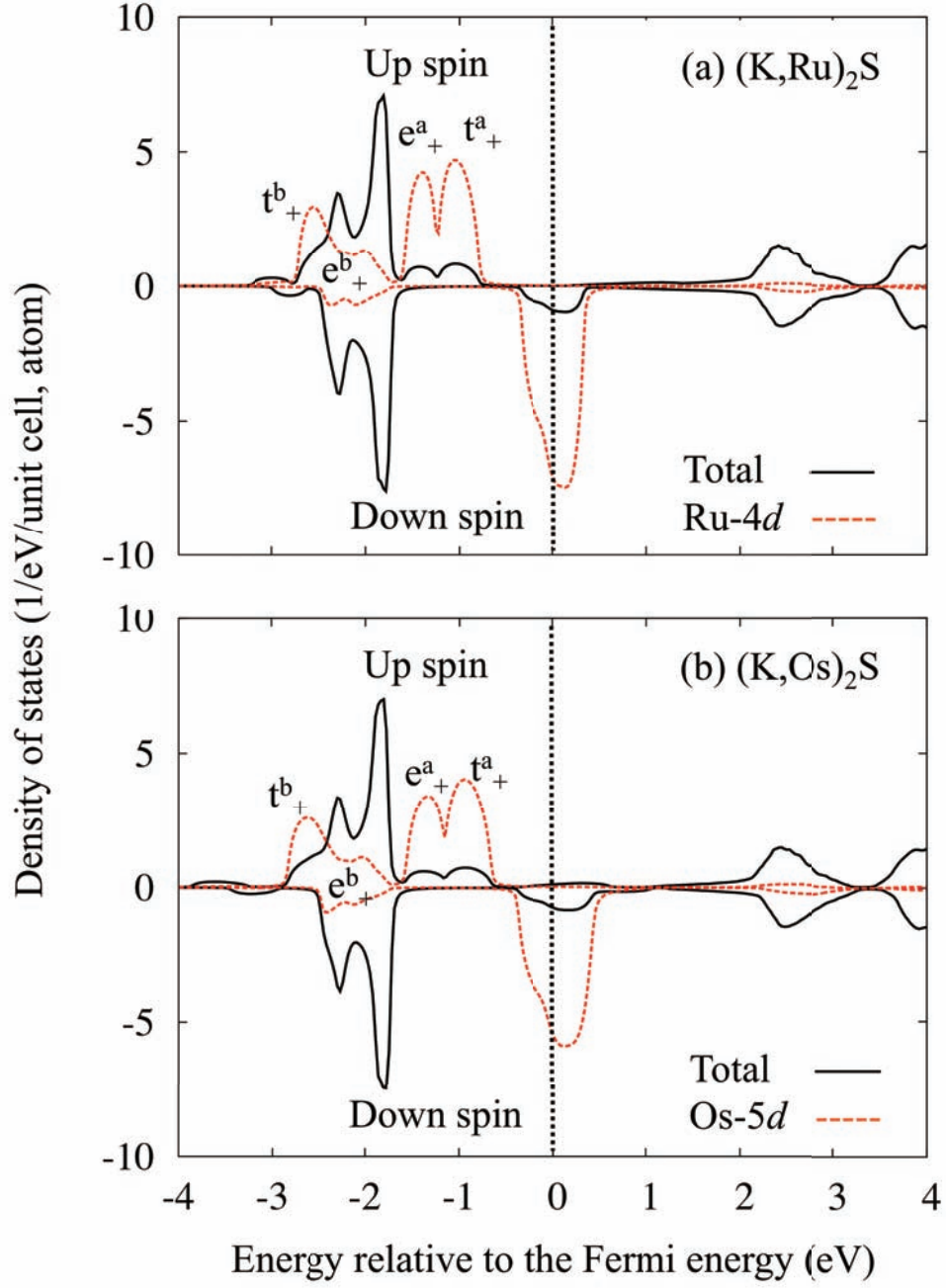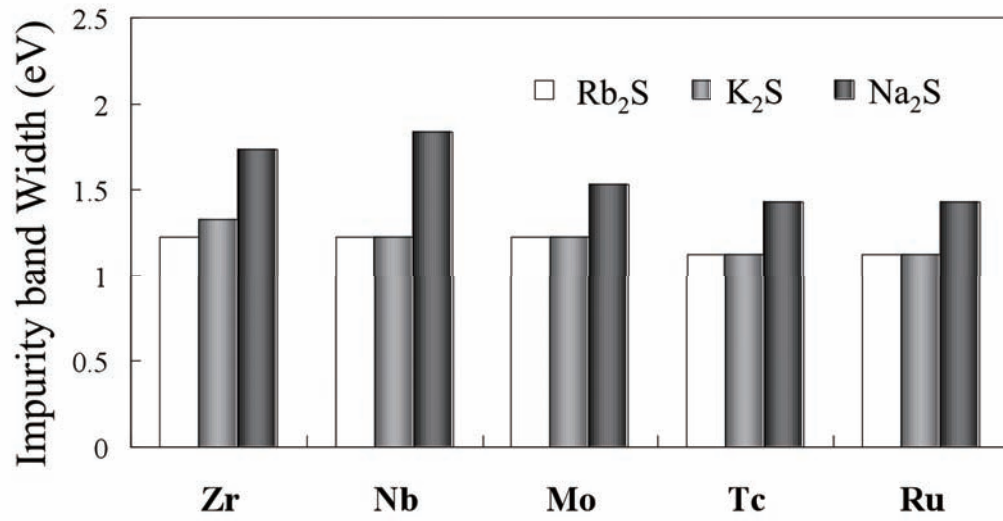
Figure 2.8: Impurity bandwidth, $W$, of Zr-, Nb-, Mo-, Tc- and Ru-doped Rb$_2$S (left), K$_2$S (middle) and Na$_2$S (right).

## 2.3 Stability of Ferromagnetic States

The stability of magnetic states was evaluated based on the total energy difference ($\Delta E$) between the disordered local moment (DLM) state and the ferromagnetic state, described as $\Delta E = E_{DLM}$ - $E_{FM}$, where $E_{DLM}$ and $E_{FM}$ represent the total energies of the DLM state and the ferromagnetic state, respectively. The DLM state was defined as a state where the local magnetic moments of the impurities are randomly set such that the total magnetic moment is zero. By definition, a positive $\Delta E$ implies that the system favors a ferromagnetic state, while a negative $\Delta E$ implies that the system favors a DLM state. The KKR-CPA-LDA package of MACHIKANEYAMA [62] was used for the calculation under the same conditions as in the previous section.

In the group of $4d$ TM dopants, Zr, Nb, Tc, Ru and Rh tended to stabilize a ferromagnetic state, while Mo tended to stabilize a DLM state (Figs. 2.9 and 2.10). In the group of $5d$ TM dopants, Hf, Ta, Re, Os and Ir tended to stabilize a ferromagnetic state, while W tended to stabilize a DLM state. Because the basic chemical trends were similar for $4d$- and $5d$-doped systems, only the results for $4d$ TM doping are presented in this section.

In Zr-, Nb-, Tc-, Ru-, Hf-, Ta-, Re- or Os-doped alkaline chalcogenides, Zener's double exchange interaction tends to be dominant since the $d$-impurity band in the bandgap was partially occupied by electrons (Figs. 2.3, 2.4, 2.6 and 2.7). The basic mechanism can be understood from a molecular model with two atomic states of energies, $\varepsilon_1 = \varepsilon_2$, and a hopping matrix element $t$. If only the bonding state is occupied and the Fermi level lies in the middle of the impurity band, an energy gain of $|t|$ occurs for ferromagnetically coupled impurities. In Mo- or W-doped chalcogenides (Fig. 2.5), the anti-ferromagnetic superexchange interaction is dominant (or competes with Zener's double exchange interaction), which results in stabilization of a DLM state (or reduces the stability of the ferromagnetic state).

Figure 2.11 presents the Curie temperature of $(K,Zr)_2S$ and $(K,Nb)_2S$ as a function of the concentration of impurities. $T_C$ was estimated by the mean field approximation (MFA), leading to $k_B T_C = \frac{2}{3} \Delta E / x$, where $x$ is the concentration of the $4d$ TM. $T_C$ increased at a rate approximately proportional to the square root of the impurity concentration for low impurity concentrations, but more or less saturated at high concentrations. In particular, for $(K,Zr)_2S$, $T_C$ gradually decreased at high concentrations. For both systems, room temperature ferromagnetism was predicted at an impurity concentration of about 5%.

Next, the effect of additional carrier doping was investigated in homogeneously Mo-

doped $K_2S$ with 5% Mo concentration. Hole carriers were introduced by substituting K with K vacancies in the compound. Electrons were introduced by substituting S with Cl in the compound. Interestingly, estimated $T_C$s increased with hole doping (Fig. 2.12) and gradually decreased with electron doping.

The dependence of the $T_C$ of $(K,Mo)_2S$ on carrier concentration can be understood by analyzing the DOS (Fig. 2.13). In Fig. 2.13, 5% K vacancies (a) and 10% Cl vacancies (c) were introduced into the 5%-Mo-doped $K_2S$. In Fig. 2.13 (b), no additional carrier doping treatment was performed. The DOS of the ferromagnetic states was plotted for all cases. As shown in Fig. 2.13 (a), holes were itinerant while maintaining their-*d*-character; therefore, the kinetic energy was reduced so efficiently that the ferromagnetic state was stabilized by Zener's double-exchange mechanism. According to the mechanism, the ferromagnetic interaction originated from the kinetic-energy gain of itinerant Mo-4*d* electrons. This explanation implied that the ferromagnetic state was the most stable when $E_F$ was located at the highest impurity density of state in the impurity band. With increasing hole concentration, $E_F$ was shifted to lower energies. However, the doped electrons never entered the Mo-4*d* states but rather the tail of the K-3*s* states in the host conduction band (Fig. 2.13 (c)); therefore, the double-exchange mechanism did not act to stabilize the ferromagnetism.
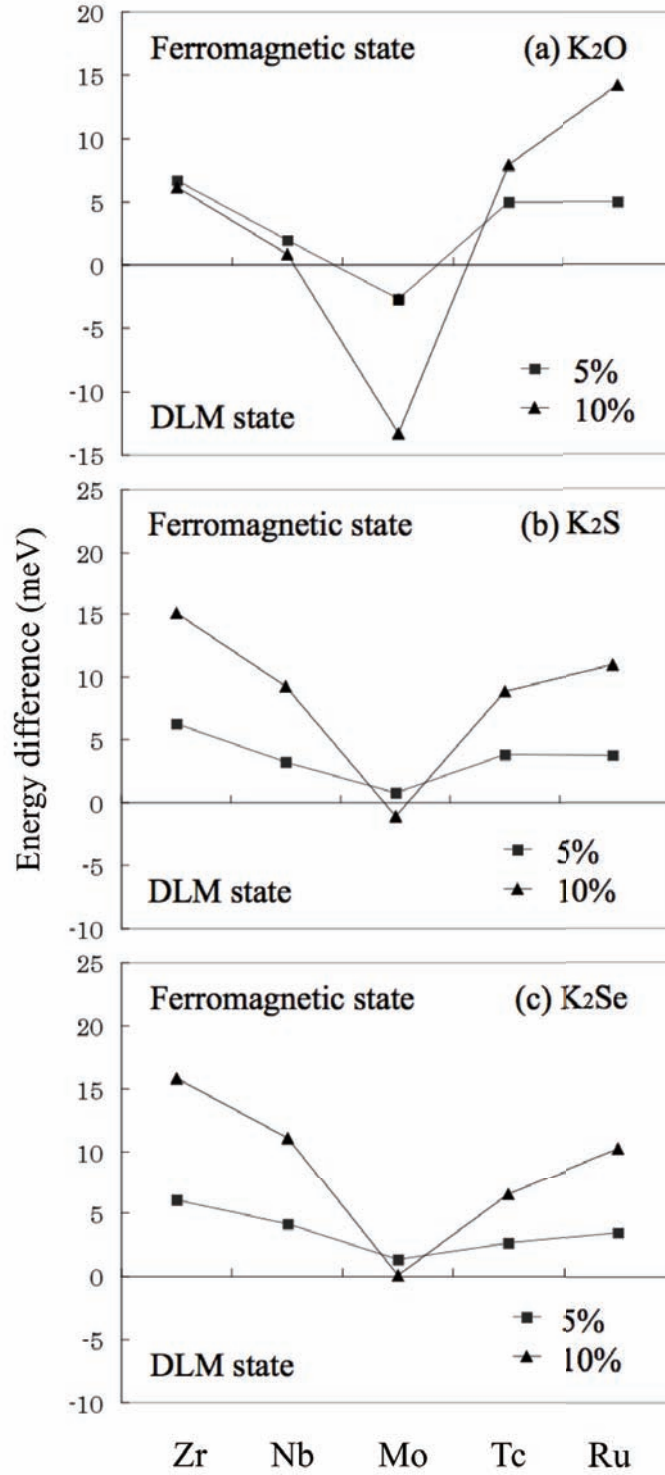
Figure 2.9: Total energy difference ($\Delta E$) per unit cell between ferromagnetic and DLM states for Zr-, Nb-, Mo-, Tc- and Ru-doped (a) $K_2O$, (b) $K_2S$ and (c) $K_2Se$ at substitutional cation site with 5% and 10% TM doping.
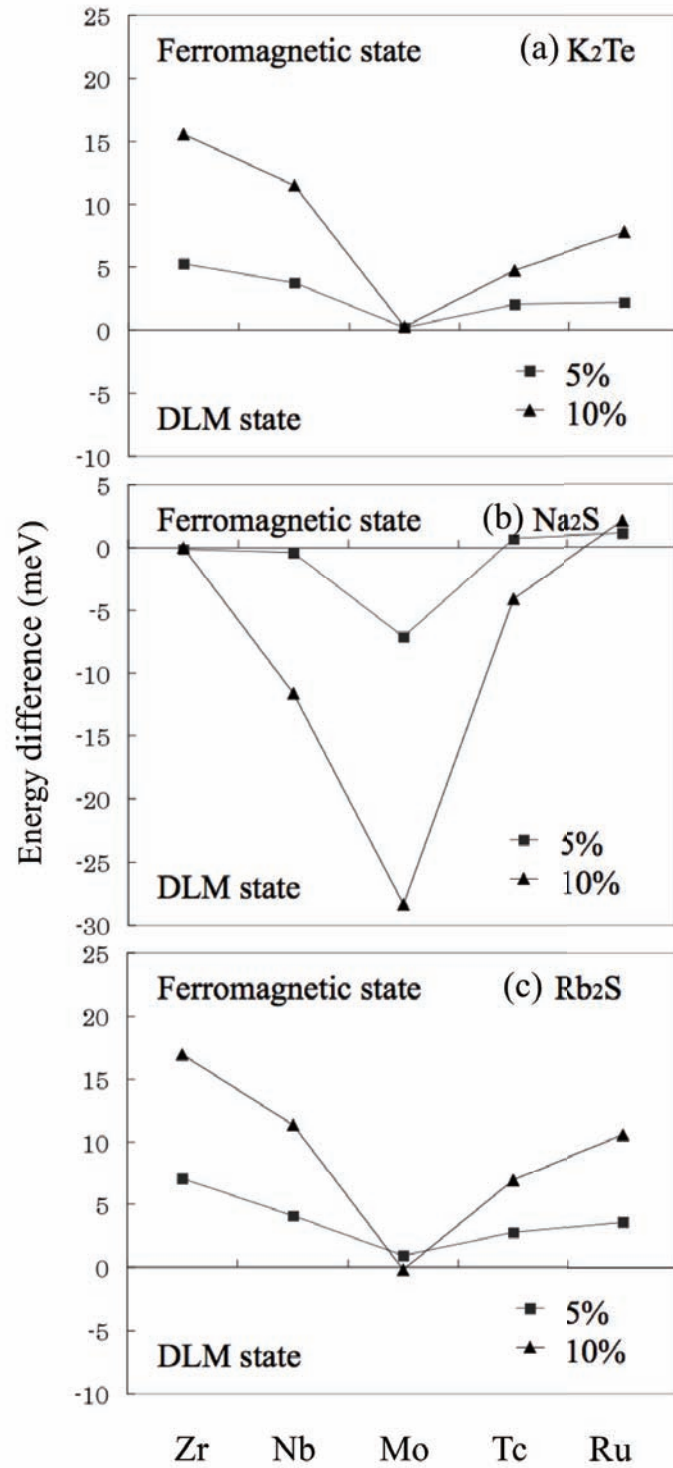
Figure 2.10: Total energy difference ($\Delta E$) per unit cell between ferromagnetic and DLM states for Zr-, Nb-, Mo-, Tc- and Ru-doped (a) $K_2Te$, (b) $Na_2S$ and (c) $Rb_2S$ at substitutional cation site with 5% and 10% TM doping. For 10%-Zr-doped $Na_2S$, a local magnetic moment cannot be formed, and a value of zero is plotted in the figure.
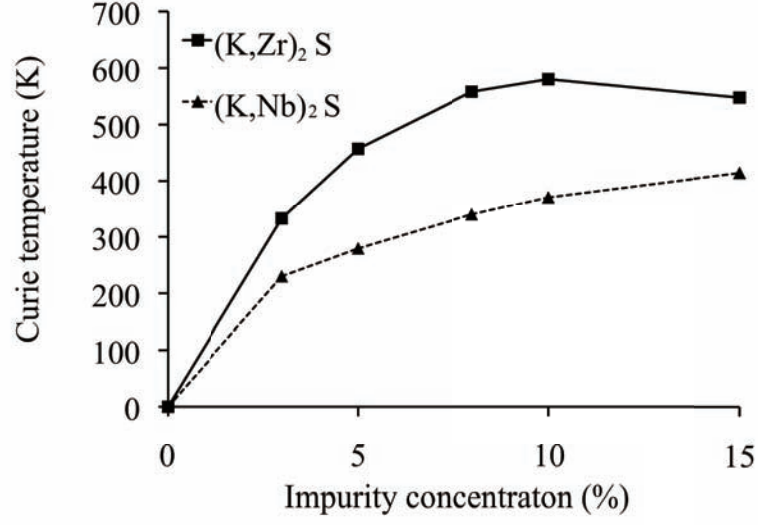
Figure 2.11: Curie temperature of $(K,Zr)_2S$ and $(K,Nb)_2S$ as a function of the dopant concentration of Zr and Nb. The dashed horizontal line indicates room temperature (300K).
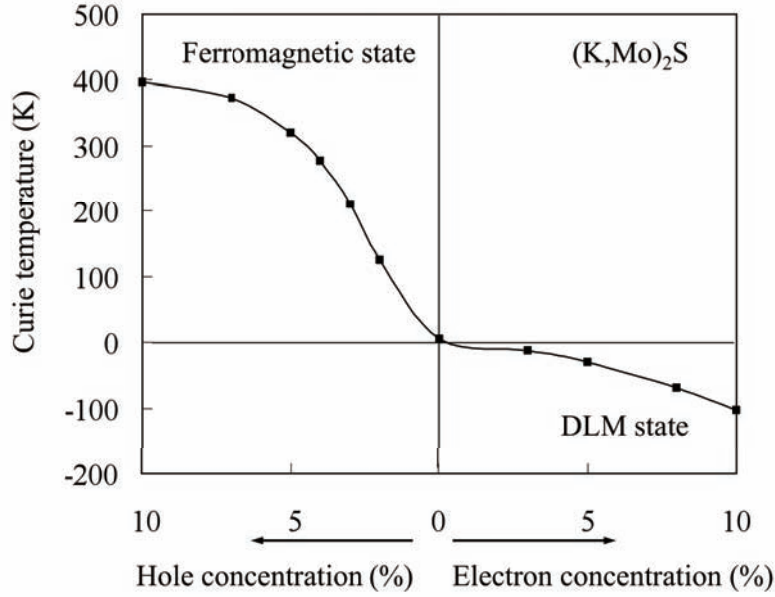


Figure 2.12: Curie temperature of $(K,Mo)_2S$ as a function of additional carrier concentration in the homogeneous system and inhomogeneous system. The Mo concentration is fixed at 5%. The hole carriers are additionally doped by substituting K with K vacancies and the electrons are doped by substituting S with Cl. The dashed horizontal line indicates room temperature (300K).
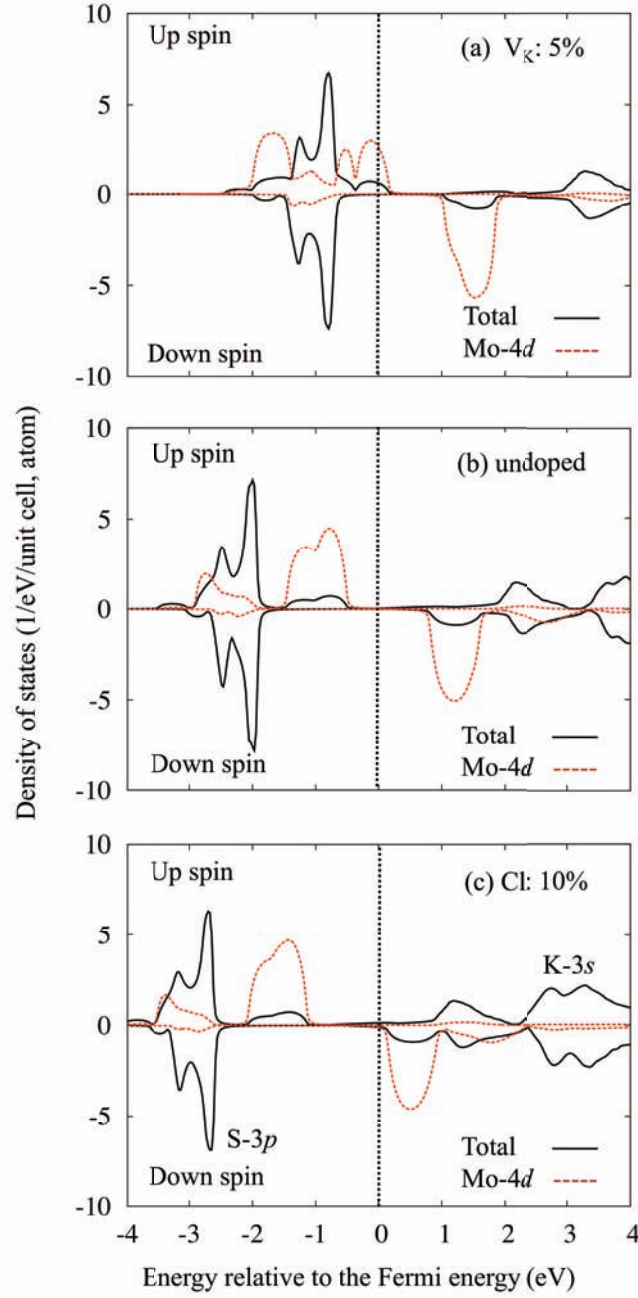
Figure 2.13: Total density of states per unit cell (solid line) and the partial density of the $4d$ states at the TM site per TM atom (dotted line) in ferromagnetic $(K,Mo)_2S$ in a homogeneous system. (a) 5% K vacancies ($V_K$) and (c) 10% Cl vacancies are introduced into 5%-Mo-doped $K_2S$. In (b), no additional carrier doping treatment is performed. The horizontal axis denotes the energy relative to the Fermi energy.

# Chapter 3

# Pioneering Materials Design of $d^0$ Ferromagnets in 2004

Within the field of DMSs, interest in the study of $d^0$ ferromagnetism significantly increased in 2004 [63]. Before 2004, reports relating to $d^0$ ferromagnetism in DMSs were quite rare and their validity remained an issue under discussion. For example, ferromagnetism was reported to be observed in calcium hexaboride ($CaB_6$) doped with lanthanum (La), a compound containing no magnetic elements [64]. Thereafter, high-temperature ferromagnetism in this $CaB_6$ system was argued as not intrinsic but, instead, caused by alien phases of iron and boride [65]. As another example, Elfimov et al. [66] proposed that CaO containing a small concentration of Ca vacancies could sustain a finite local magnetic moment when a model Hamiltonian with a tight-binding linear-muffin-tin-orbital (TB-LMTO) is used. However, stability of the ferromagnetism was not demonstrated. In 2004, pioneering computational materials design (CMD) was presented to open the route to $d^0$ ferromagnetism. In that year, $K_2(S,Si)$ and $K_2(S,Ge)$ were initially designed as potential candidates for $d^0$ ferromagnets, wherein deep impurity bands consisting of $3p$ orbitals were introduced in the bandgap, with the partially filled $3p$ shells and ferromagnetic states stabilized by Zener's double exchange mechanism [39]. Soon after, this idea was applied to $2p$ orbitals, and Ca(O,C) and Ca(O,N) were designed as $d^0$ ferromagnets in June 2004 [40]. Before the end of the year, the idea was generalized to design other alkaline-chalcogenide- or alkaline-earth-metal-chalcogenide-based $d^0$ ferromagnets [41], including C- or N-doped MgO, SrO and BaO [42]. Following this direction, many other CMDs of $d^0$ ferromagnets were presented, such as those for N-doped $SiO_2$ [44] and H-B- or H-P-codoped diamond [45]. In 2009, experimental work validated the ferromagnetic behavior exhibited by N-doped MgO [50]. It is worth noting that, in August 2004, $d^0$ ferromagnetism in

undoped HfO was experimentally reported soon after the initial series of the above materials design [53].

In this chapter, the pioneering CMDs of alkaline-chalcogenide-based $d^0$ ferromagnets and alkaline-earth-metal-oxides-based $d^0$ ferromagnets presented in 2004 are reviewed.

## 3.1   Alkaline-Chalcogenide-Based $d^0$ Ferromagnets

After the discovery that spatially broad orbitals, such as $4d$ and $5d$ orbitals, could create local magnetic moments [35, 36, 37, 38], we speculated that $p$ bands may spontaneously polarize to provide a ferromagnetic state. Following this speculation, we theoretically demonstrated the existence of $p$ bands in K$_2$(S,Si) and K$_2$(S,Ge), where deep impurity bands consisting of $3p$ orbitals were introduced in the bandgap with the partially filled $3p$ shells stabilizing a ferromagnetic state [39]. This principle was generalized and applied to design many other alkaline-chalcogenides-based $d^0$ ferromagnets [40, 41, 42, 44, 43, 45]. In this section, the materials design of ferromagnetic K$_2$(S,Si) and K$_2$(S,Ge) are introduced as the initial CMD among alkaline-chalcogenide-based $d^0$ ferromagnets.

To stabilize ferromagnetism via the $p$-impurity band in the bandgap of semiconductors, narrow $p$-impurity bands need to be designed in the bandgap. By changing the lattice spacing and $p$-impurity concentration to control the hybridization of the $p$ orbital of the dopants with an orbital of the host material, the splitting condition ($U \geq W$) for the ferromagnetism can be optimized. K$_2$S with an anti-CaF$_2$ crystal structure has a wide bandgap and large lattice spacing (a = 7.39 Å) due to the large ionic radii of K$^+$ and S$^{2-}$. Because of its wide bandgap and large lattice spacing, a narrow $p$-impurity band in the bandgap is achieved to stabilize the ferromagnetic state.

The calculation scheme used in this chapter was same as that described in the previous chapter for $4d$-TM-doped DMSs. First-principle calculations were performed using MACHIKANEYAMA [62], the KKR-CPA-LDA package. The stability of the ferromagnetic state was evaluated by calculating the energy difference between a ferromagnetic state and a DLM state within the MFA. The experimentally determined lattice constant of the K$_2$S host material (a = 7.39 Å) was used. Lattice relaxation was not taken into consideration.

K$_2$(S,Si) and K$_2$(S,Ge) were observed to exhibit high-spin and half-metallic ferromagnetic ground states with a narrow ($W \sim 0.6$eV) $p$-impurity band in the bandgap and total magnetic moments of 2.0 $\mu_B$ per impurity (Fig. 3.1). The $p$ states of S were repulsively perturbed by the $p$ orbital of Si or Ge and the $p$-impurity band was moved

into the bandgap. The exchange-splitting energy ($\Delta_X \sim 0.8$eV) between the majority (up) spin states and the minority (down) spin states was larger than the impurity-band width. The localized magnetic moment was created at the impurity site under agreement with the splitting condition ($U \geq W$) due to the large lattice spacing of $K_2S$ with its anti-$CaF_2$ structure. The calculated $T_C$s rapidly increased for lower concentrations, at a rate approximately proportional to the square root of the concentration of Si impurities, but more or less saturated at higher concentrations, due to the impurity screening effect (Fig. 3.2). In these $d^0$ ferromagnets, Zener's double exchange interaction was dominant because the $p$-impurity-band interaction in the bandgap was partially occupied by electrons.

Next, the effect of additional carrier doping was investigated in $K_2$(S,Si). Here, the Si concentration was fixed at 10%. Hole carriers were introduced by substitution of vacancies on K sites in the compound. Electrons were introduced by substituting S by Cl in $K_2$(S,Si). $T_C$s slightly decreased for electron-doped $K_2$(S,Si), and ferromagnetism disappeared at 18%, while for hole-doped $K_2$(S,Si), $T_C$s decreased with increasing hole concentration (Fig. 3.3).

The dependence of the $T_C$ of $K_2$(S,Si) on carrier concentration can be understood by analyzing their DOSs (Fig. 3.4). Their DOSs were plotted for the ferromagnetic states in Fig. 3.4 (a)-(c) and for the non-magnetic states in Fig. 3.4 (d). According to Zener's double-exchange mechanism, the ferromagnetic interaction originated from the kinetic-energy gain of the itinerant Si-$3p$ electrons. This explanation implied that the ferromagnetic state was most stable when $E_F$ was located at the higher impurity density of state in the impurity band. With increasing hole concentration, $E_F$ was shifted to lower energy (Fig. 3.4 (a)). As a result, $E_F$ approached the edge of the impurity band, and, simultaneously, $T_C$ decreased. The exchange-splitting energy between an up and down spin state decreased for electron-doped $K_2$(S,Si) (Fig. 3.4 (c)). However, at low concentration, $E_F$ was still located near the higher energy side of the impurity peak and the $T_C$s remained at approximately 300K. The non-magnetic solution was obtained at 18%-electron concentration because the splitting condition ($U \geq W$) was not satisfied (Fig. 3.4 (d)).
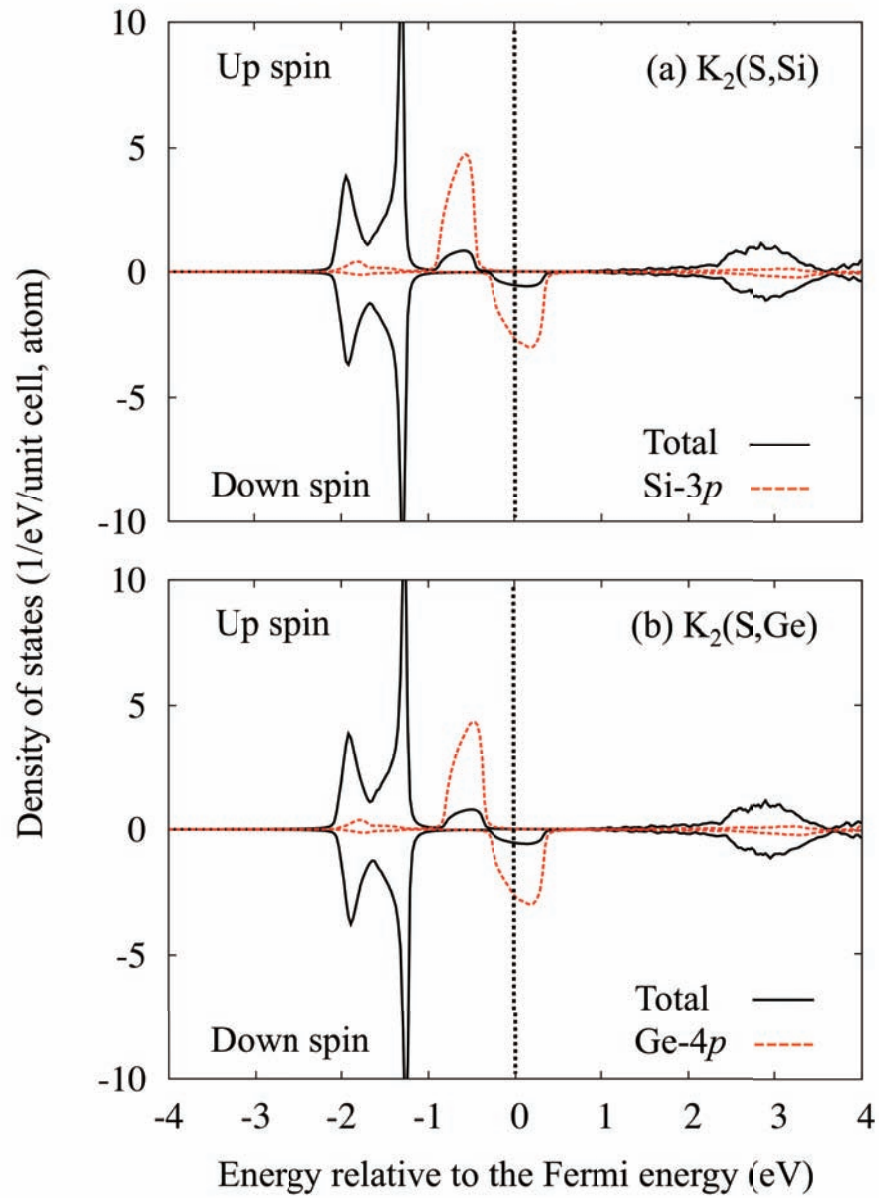
Figure 3.1: Total density of states per unit cell (solid line) and partial density of states at Si site per atom (dashed line) in (a) $K_2(S,Si)$ and (b) $K_2(S,Ge)$ in the ferromagnetic state, respectively. The impurity concentration is 10% and the horizontal axis denotes the energy relative to the Fermi energy.
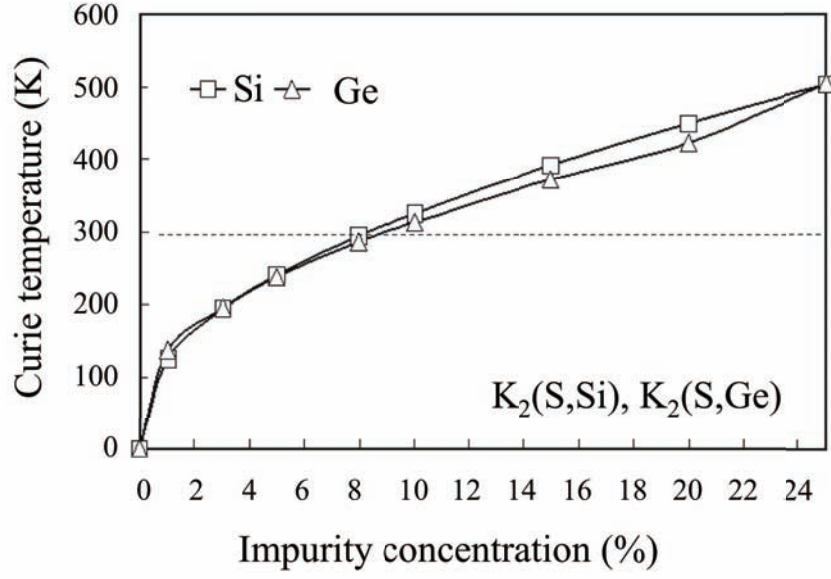
Figure 3.2: Curie temperature of $K_2$(S,Si) and $K_2$(S,Ge) as a function of the concentration of Si and Ge impurity. The dashed horizontal line indicates room temperature (300K).
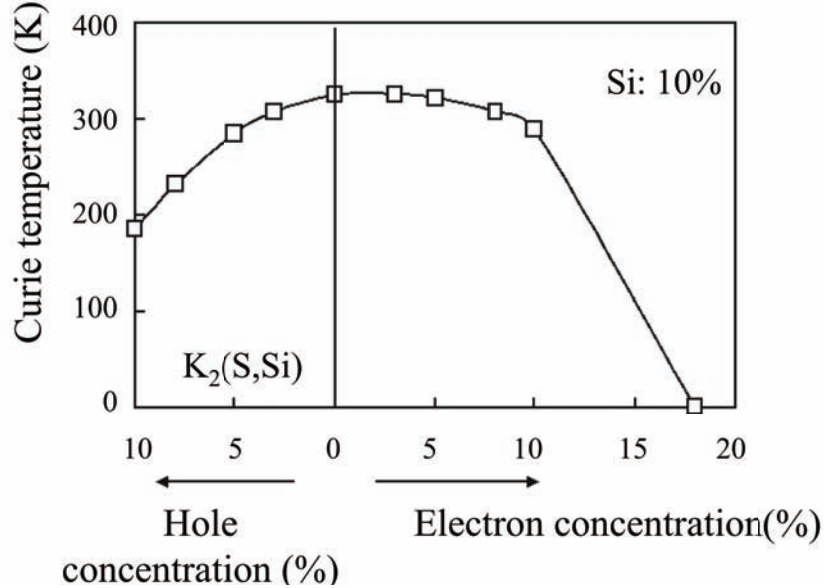


Figure 3.3: Curie temperature of $K_2$(S,Si) as a function of the additional carrier concentration. Hole carriers are introduced by substitutional vacancies on K, while electrons are introduced by substituting S by Cl.
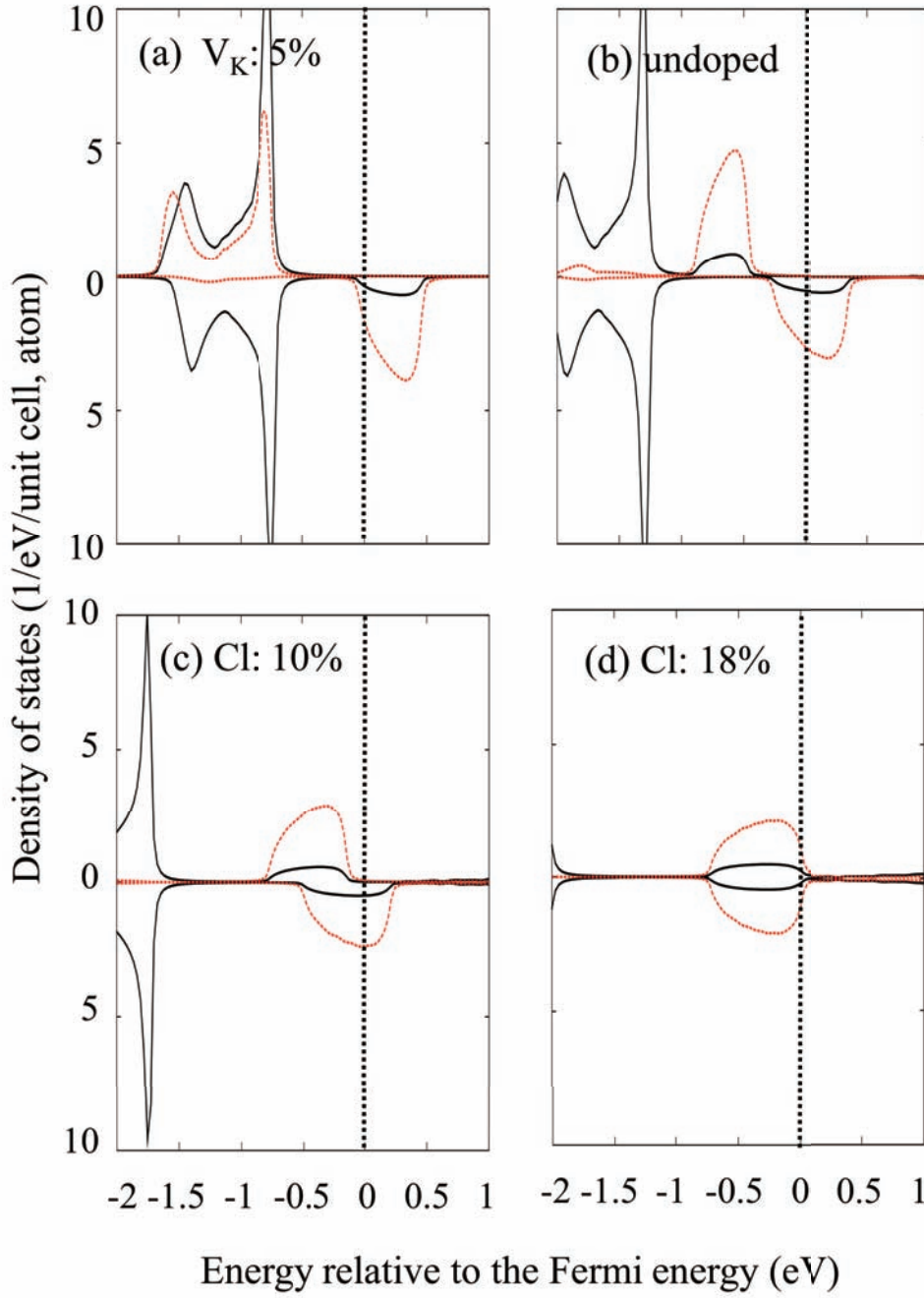
Figure 3.4: Total density of states per unit cell (solid line) and the partial density of Si-$3p$ states per Si atom (dashed line) in ferromagnetic K$_2$(S,Si). (a) K vacancy (V$_K$: 5%, (c) Cl: 10%, (d) Cl: 18% are additionally introduced into 10%-Si-doped K$_2$S. In (b) no additional carrier doping treatment is performed. Their DOSs are plotted for the ferromagnetic states in (a)-(c) and for the non-magnetic states in (d). The horizontal axis denotes the energy relative to the Fermi energy.

## 3.2 Alkaline-Earth-Metal-Chalcogenide-Based $d^0$ Ferromagnets

The principle used for the materials design of $K_2S$-based $d^0$ ferromagnets was also applied to the $2p$ orbitals in Ca(O,C) and Ca(O,N) [40], and to the design of many other alkaline-earth-metal-chalcogenides-based ferromagnets [41, 42, 44, 43], including C- or N-doped MgO, CaO, SrO, BaO, MgS and MgSe. In this section, the materials design of CaO-based $d^0$ ferromagnets is introduced as the initial CMD among the CMD of alkaline-earth-chalcogenide-based $d^0$ ferromagnets. CaO is an insulator with a wide band gap of 7 eV; its transparency to visible light permits its use in optical applications. Additionally, such DMSs are beneficial for the environment since they do not contain toxic elements.

The calculation scheme used in this chapter was the same as that used in the previous section. The experimentally determined lattice constant of the CaO host material for a rock-salt structure (Fig. 3.5, a = 4.81 Å, [67]) was used. The stability of the ferromagnetic state was evaluated by the calculated energy difference between a ferromagnetic state and a DLM state within the MFA.

To compare electronic structures in ferromagnetic states, we plotted the DOS of Ca(O,B), Ca(O,C) and Ca(O,N) with 5% doping concentration (Fig. 3.6). In the DOS, the deep-impurity band was moved up into the band gap of CaO. The exchange-splitting energy ($U$) between the majority (up) spin states and the minority (down) spin states was larger than $W$ for all cases (e.g., $\Delta_X = 1.12$ eV and $W = 0.45$ eV for 5%-C-doped CaO), which lead to a high-spin ground state. The splitting condition ($U \geq W$) was satisfied, and the localized magnetic moment was created at the deep-impurity site.

From calculation of $\Delta E$, the ferromagnetic state was observed to be more stable than the DLM state in Ca(O,C) and Ca(O,N) (Fig. 3.7). The origin of ferromagnetism in Ca(O,C) and Ca(O,N) is Zener's double-exchange mechanism because the narrow and highly-correlated deep-impurity bands are partially occupied. However, the spin-glass state was more stable than the ferromagnetic state in Ca(O,B) since the up spin states of the deep-impurity band were fully occupied and the down spin states were empty. As shown in Figs. 3.6 (b) and (c), Ca(O,C) and Ca(O,N) were half metallic; the total magnetic moments per impurity atom were 2.0 $\mu_B$ and 1.0 $\mu_B$, respectively.

For Ca(O,C), high-$T_C$ ferromagnetism at 340 K was predicted for a C-impurity concentration of about 5% (Fig. 3.7). According to Sato [9], $T_C$s increase approximately proportionally to the square root of the concentration of impurities when Zener's

double-exchange mechanism dominates. Therefore, a similar concentration dependence should appear for the cases of Ca(O,C) and Ca(O,N) in Fig. 3.7. However, due to the anti-ferromagnetic superexchange interaction, the $T_C$s were already saturated in the investigated concentration range.

Next, the effect of additional p- or n-type carrier doping was investigated in Ca(O,C). The C concentration was fixed at 5%. Additional hole carriers were introduced by substitutional K at Ca sites. Additional electrons were introduced by substitutional Sc at Ca sites. Calculated $T_C$s were plotted as a function of the additional hole and electron concentrations (Fig. 3.8). $T_C$ slightly increased with increasing electron concentration and reached a maximum at 2.5% additional electrons before decreasing. Ferromagnetism disappeared at 10%. For additional hole doping in Ca(O,C), $T_C$ decreased and ferromagnetism disappeared with 5% of additional holes.

As previously discussed, the dependence of $T_C$ on carrier concentration in Ca(O,C) can be understood from the viewpoint of Zener's double exchange mechanism (Fig. 3.9). According to the mechanism, the ferromagnetic interaction originated from the kinetic-energy gain in a partially-occupied deep-impurity-band of C-$2p$ electrons. This explanation implied that the ferromagnetic state was most stable when the $E_F$ was located at the center of the impurity band. At 2%-Sc concentration, $E_F$ was located at the center of the impurity band in Fig. 3.9 (c), and $T_C$ was maximized. The exchange-splitting energy between the up and down spin states decreased with increasing electron concentration. With 10% Sc, the impurity bands were completely occupied, and the system became non-magnetic (Fig. 3.9 (d)). With increasing K concentration, $E_F$ was shifted to the lower energy region (Fig. 3.9 (a)). As a result, the impurity band became almost empty, $T_C$ simultaneously decreased, and the DLM state became more stable than the ferromagnetic state.
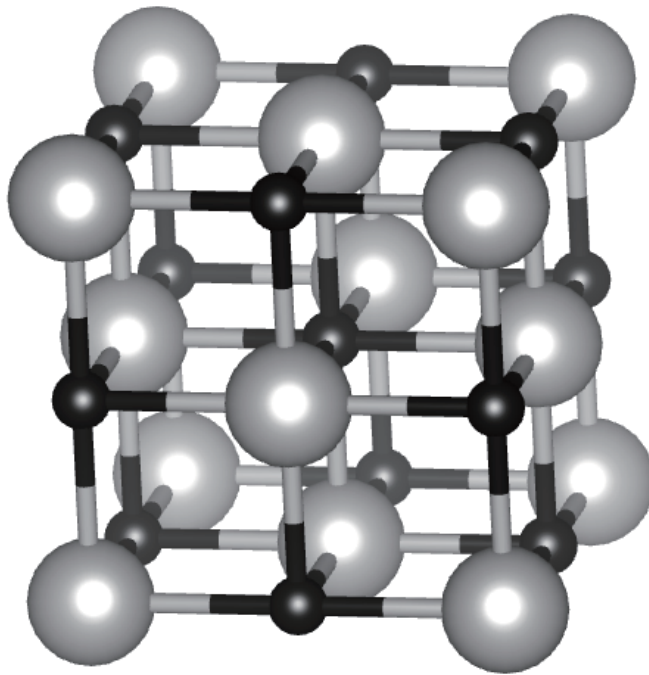
Figure 3.5: Atomic configuration of rock-salt structure. The large and small spheres represent cations and anions, respectively. The VESTA visualization program [59] was used to prepare this image.
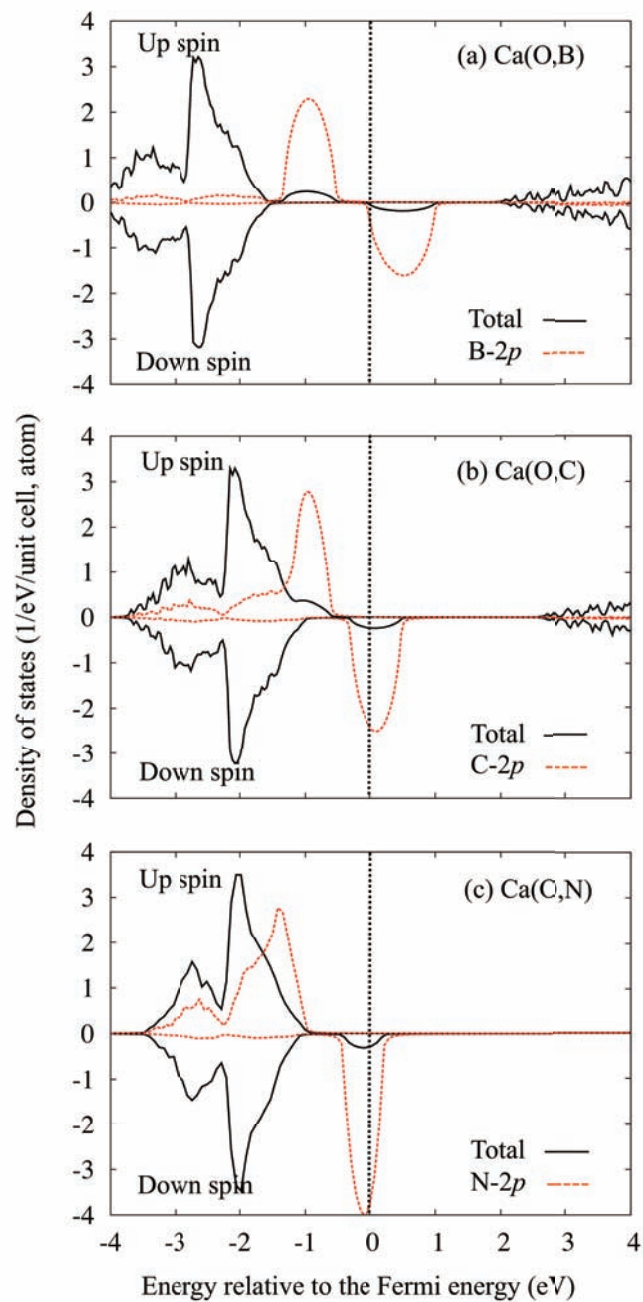
Figure 3.6: Total density of states per unit cell (solid line) and the partial $2p$ density of states at O site per atom (dashed line) in CaO-based $d^0$ DMSs in the ferromagnetic state. The impurity concentration is 5%. The horizontal axis denotes the energy relative to the Fermi energy. The upper and lower sides of the figures stand for the DOS of the up and down spin states respectively.
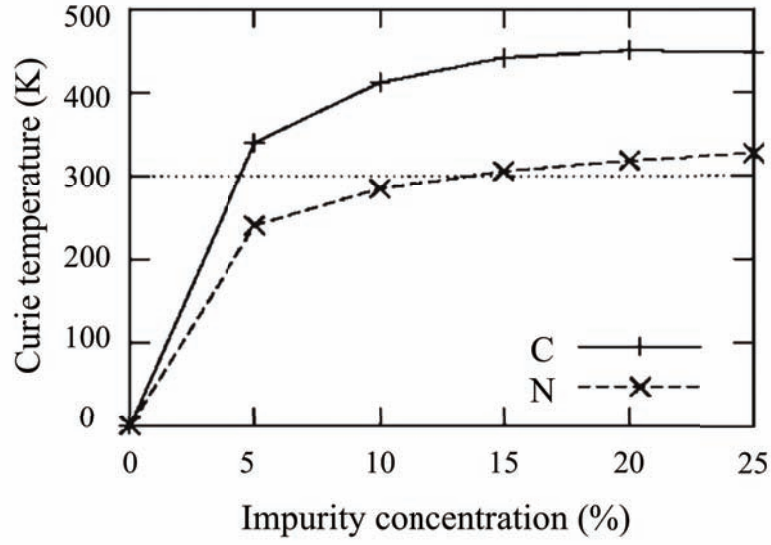
Figure 3.7: Curie temperature of Ca(O,C) and Ca(O,N) as a function of the concentration of C and N impurities. The dashed horizontal line indicates room temperature (300K).
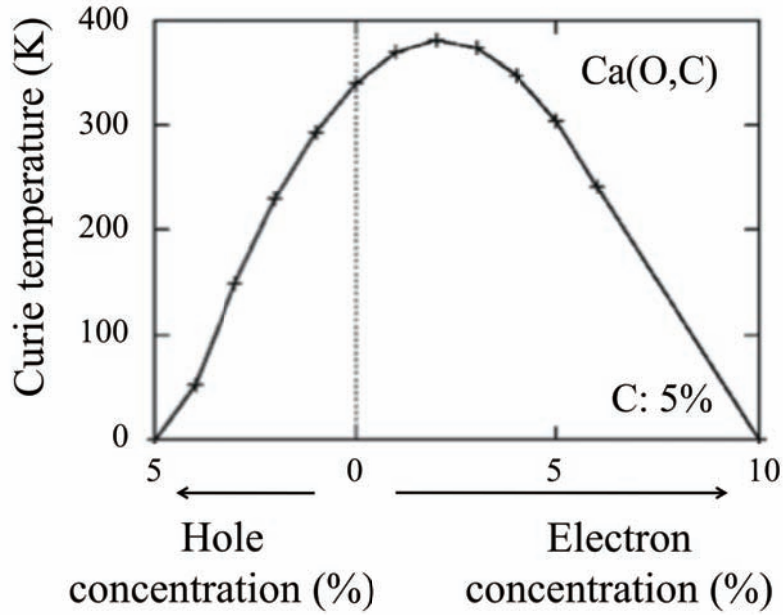


Figure 3.8: Curie temperature of Ca(O,C) with 5% C as a function of additional carrier concentration. Hole carriers are introduced by substituting O with B. Electrons are introduced by substituting Ca with Sc.
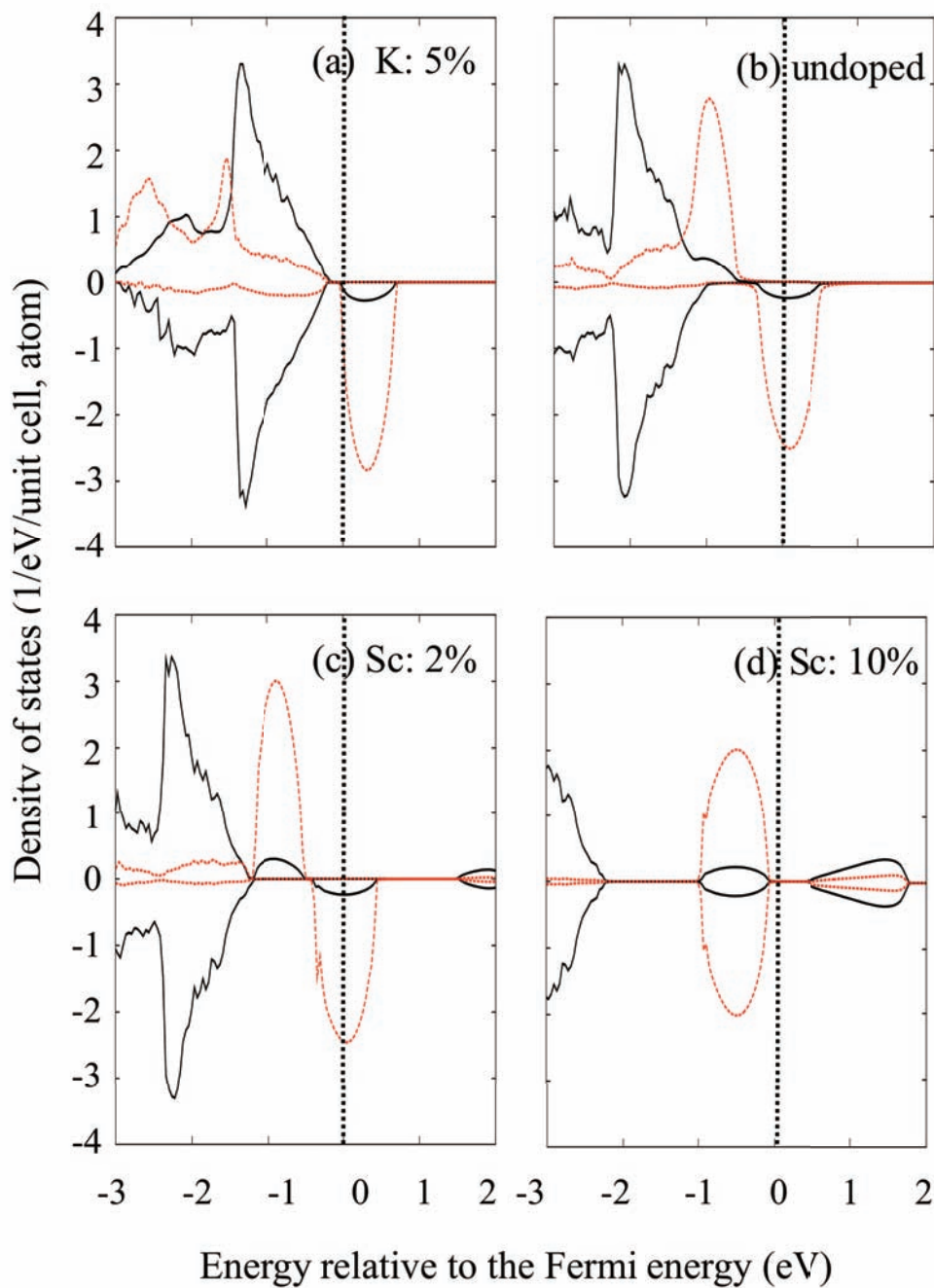
Figure 3.9: Total density of states per unit cell (solid line) and the partial density of C-$2p$ states per C atom (dashed line) in ferromagnetic Ca(O,C). (a) K: 5 %, (c) Sc: 2 %, (d) Sc: 10 % are additionally introduced into 5 %-C-doped CaO. In (b) no additional carrier doping treatment is performed. Their DOSs are plotted for the ferromagnetic states in (a)-(c) and for the non-magnetic states in (d). The horizontal axis denotes the energy relative to the Fermi energy.

# Chapter 4

# Comprehensive Analysis of Magnetic Properties in Alkaline-Earth-Metal-Oxide-Based $d^0$ Ferromagnets

Although significant works have demonstrated the potential route to $d^0$ ferromagnetism, the origin of the magnetism is not yet fully understood. MgO is one of the most attractive materials for investigating $d^0$ ferromagnetism because its wide bandgap yields a spin-polarized $p$ band and it is also important for industrial applications [68]. In addition, MgO-based $d^0$ ferromagnets will open a new route to creating environmentally friendly materials for spintronics without the use of magnetic elements. Thus, a comprehensive analysis including MgO-based $d^0$ ferromagnets is especially valuable.

In this chapter, the magnetic mechanisms and properties are investigated in Mg(O,N), Ca(O,N), and Sr(O,N) for an anion-substitution group and in $(Mg,V_{Mg})O$, $(Ca,V_{Ca})O$, and $(Sr,V_{Sr})O$ for a cation-substitution group. The magnetic properties are investigated from two major points of views, i.e., the properties under homogeneous distribution condition and those under inhomogeneous distribution if inhomogeneity is energetically favored.

## 4.1 Analysis under a Homogeneous Distribution Condition

In this section, the calculation procedure consists of three steps: (i) calculation of the electronic structure for a homogeneous DMS system with a random distribution of

dopants, (ii) calculation of the magnetic exchange interactions between two magnetic sites in an effective medium of the homogeneous system, and (iii) estimation of $T_C$ using the calculated exchange interactions. The significance of SIC is also discussed.

### 4.1.1  Electronic Structure

First, electronic structures of these DMSs were calculated using the KKR-CPA [60, 61] within the context of the pseudo-self-interaction-corrected LDA (PSIC-LDA) [32]. In this framework, dopants are randomly distributed at assigned sites in the host material, which can be described as $MO_{1-x}N_x$ or $M_{1-x}Vc_x$ wherein M represents the anion atoms of the host materials (Mg, Ca or Sr), Vc represents the vacancies, and x represents the dopant concentrations. In contrast to the supercell method, which calculates a single, periodic configuration of a system, the CPA method calculates a configuration average of a disordered system by using the single-site effective medium theory. Here, the PSIC is introduced to correct the error of the LDA. The SIC method was originally proposed by Perdew [33], and the PSIC method was developed by Filippetti and Spaldin [34]. The PSIC method has been shown to reasonably reproduce the electronic structures of ZnTe-, GaN- and ZnO-based DMSs [32] (see Appendix for more details).

For the KKR-CPA calculation, the simulation package of PSIC-implemented [32] MACHIKANEYAMA [62] was used. The experimentally determined lattice constants of the MgO, CaO and SrO host materials (a = 4.21, 4.81 and 5.16 Å, respectively [67]), which have a rock-salt structure, were used. Lattice relaxation was not taken into account. The form of the potential was restricted to the muffin-tin type.

To compare electronic structures in ferromagnetic states, we plotted the DOS of Mg(O,N), Ca(O,N), Sr(O,N), $(Mg,V_{Mg})O$, $(Ca,V_{Ca})O$ and $(Sr,V_{Sr})O$ with 5% doping concentration (Fig. 4.1 and 4.2). In terms of common characteristics of the N-doped systems, spin-polarized and half-metallic impurity bands were introduced in the band gap, and the impurity bands were partially filled by electrons. The main difference between the systems was observed in the band widths of the valence and impurity bands; the band widths decreased in the order of Mg(O,N), Ca(O,N) and Sr(O,N). Common characteristics in the vacancy-doped systems were that the valence bands mainly consisted of O $2p$-orbitals and exhibited spin-polarization. The main difference in these systems was observed in the valence-band widths, which had the same tendency as the N-doped DMSs. Interestingly, these total density of states of vacancy-doped sytems were similar to those of Fe and Ni in a ferromagnetic state.
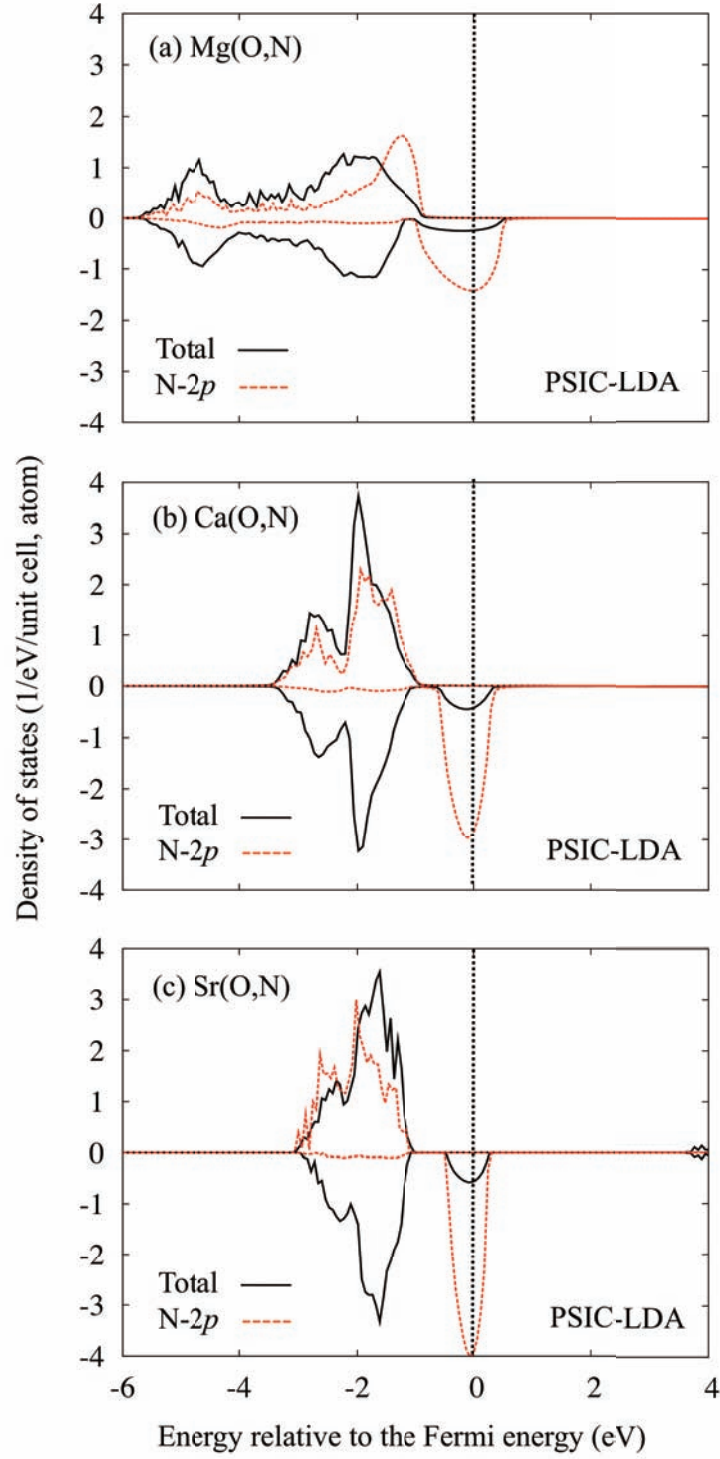
Figure 4.1: Total (solid line) and partial (dashed line) densities of states of N-doped systems calculated by PSIC-LDA. The solid lines and dotted lines represent the total DOS and N-2p partial DOS, respectively. The positive and negative values of the density of states represent those for up and down spins, respectively.
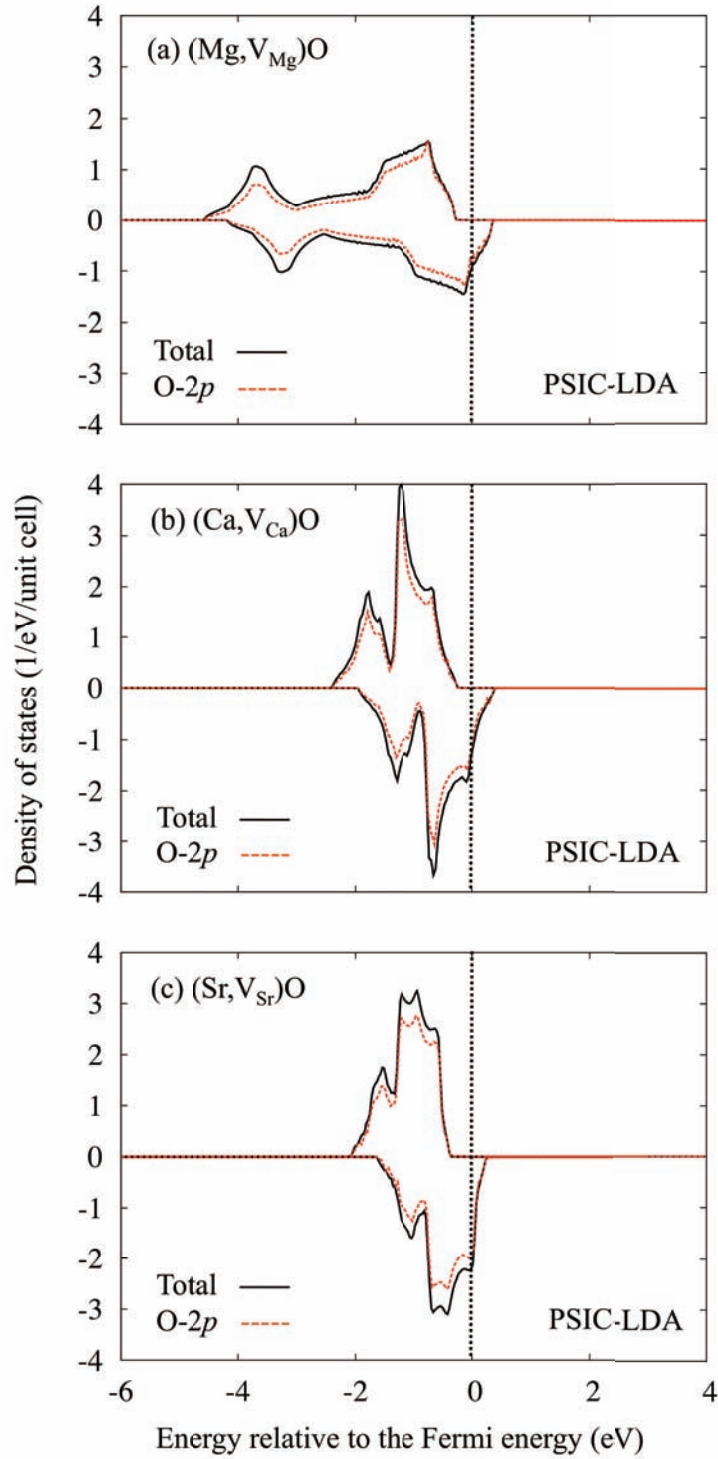
Figure 4.2: Total (solid line) and partial (dashed line) densities of states of vacancy-doped systems calculated by PSIC-LDA. The solid lines and dotted lines represent the total DOS and O-2p partial DOS, respectively. The positive and negative values of the density states represent those for up and down spins, respectively.

## 4.1.2 Significance of Self-Interaction Correction

To discuss the significance of the PSIC, electronic structures were also calculated within the LDA. PSIC-LDA was observed to produce higher stability of the magnetic ground state than the LDA (Figs. 4.1 - 4.7). The difference was especially notable in the vacancy-doped systems. For instance, in MgO with 10% $V_{Mg}$, the LDA yielded a non-magnetic ground state (Fig. 4.2 (a)), while the PSIC-LDA produced a spin-polarized and half-metallic ground state (Fig. 4.4 (a)). The total magnetic moments originated from the O-$2p$ band and increased linearly as a function of doping concentrations in the PSIC-LDA calculation (Fig. 4.5 (a)); this behavior was not observed in the LDA calculation for vacancy concentrations under 10% (Fig. 4.5 (b)). Satisfaction of the splitting condition ($U \geq W$) is an important guideline for the formation of a localized magnetic moment in materials with no magnetic elements; in the LDA calculation, the underestimation of $U$ causes the instability of the magnetic states. For this reason, beyond-LDA methods, such as the PSIC, is essential to calculation of the proper electronic structures.
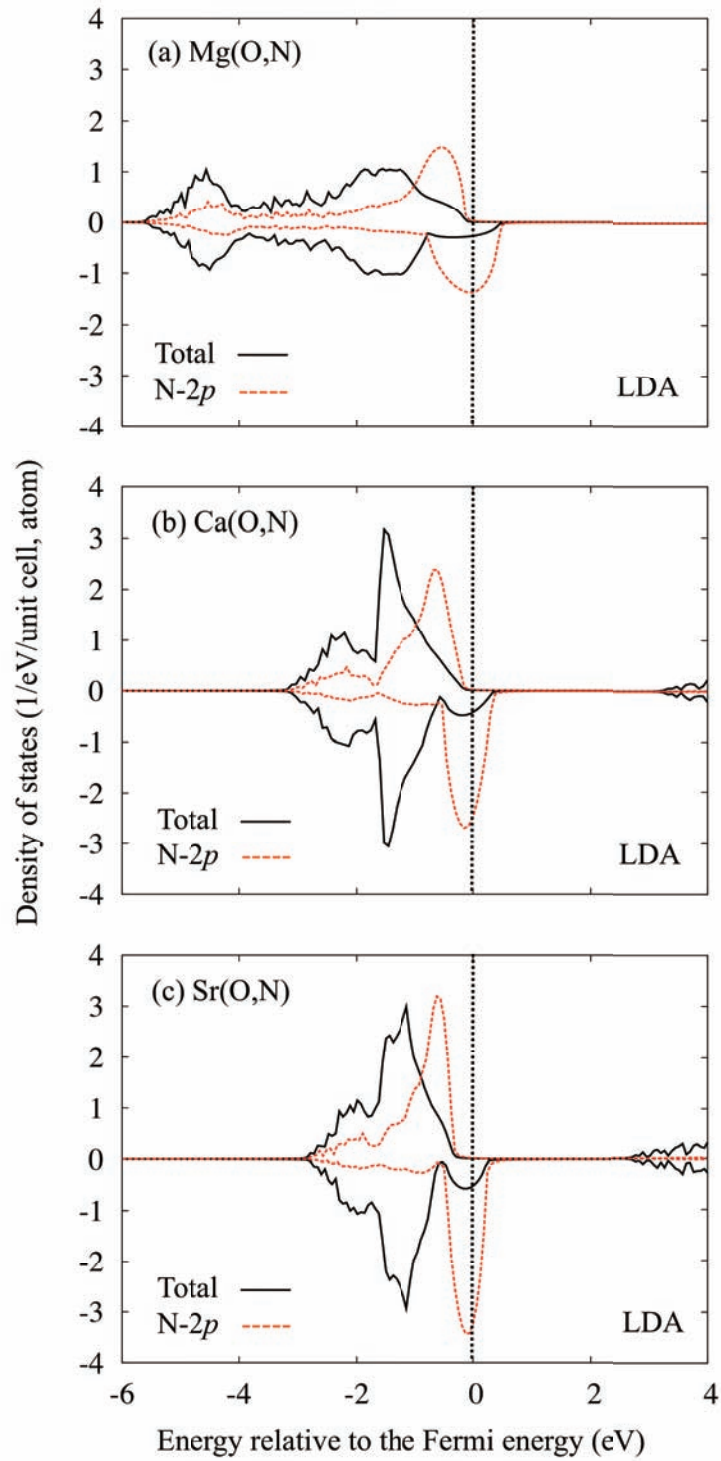
Figure 4.3: Calculated total (solid line) and partial (dashed line) density of states of
N-doped systems with 10% N by LDA.
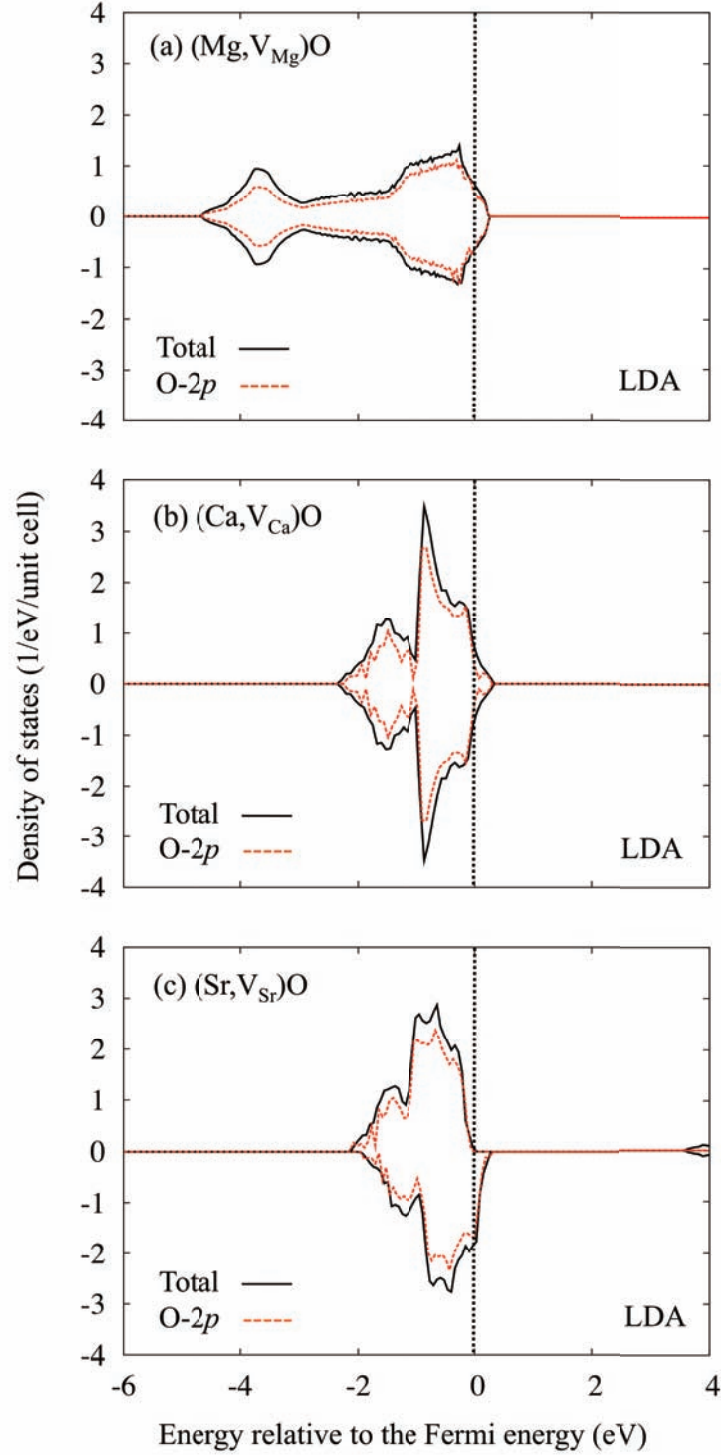
Figure 4.4: Calculated total (solid line) and partial (dashed line) density of states of vacancy-doped systems with 10% vacancies by LDA.
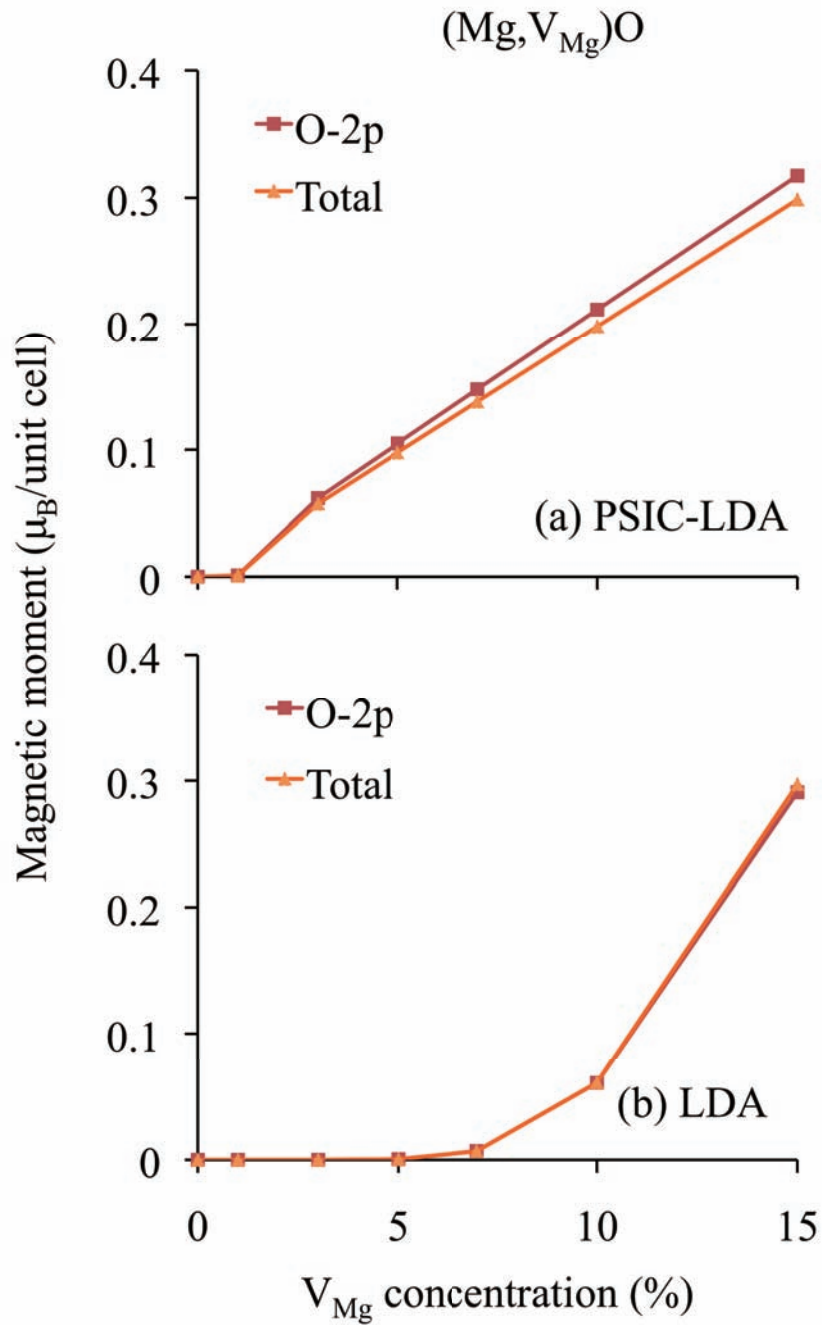
Figure 4.5: Calculated magnetic moments of $(Mg,V_{Mg})O$ by (a) PSIC-LDA and (b) LDA.
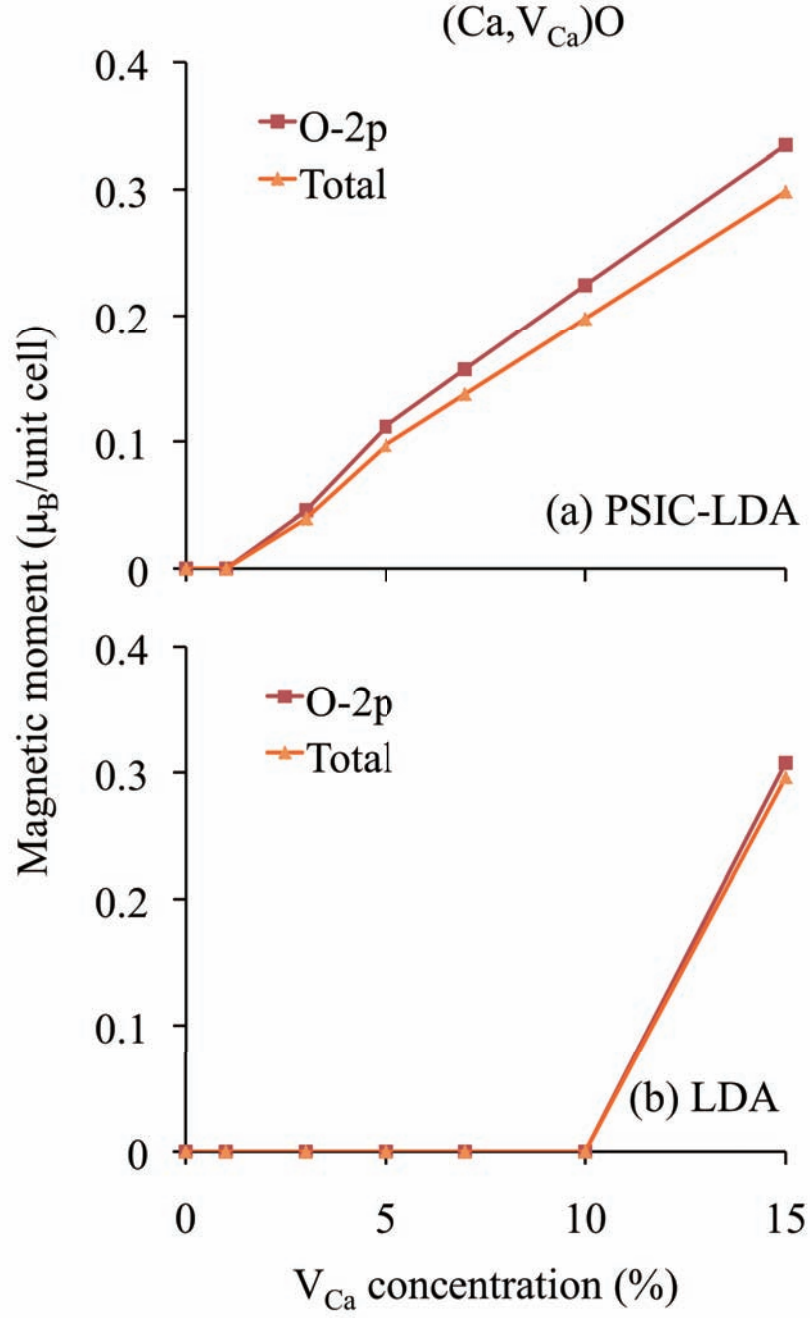
Figure 4.6: Calculated magnetic moments of $(Ca, V_{Ca})O$ by (a) PSIC-LDA and (b) LDA.
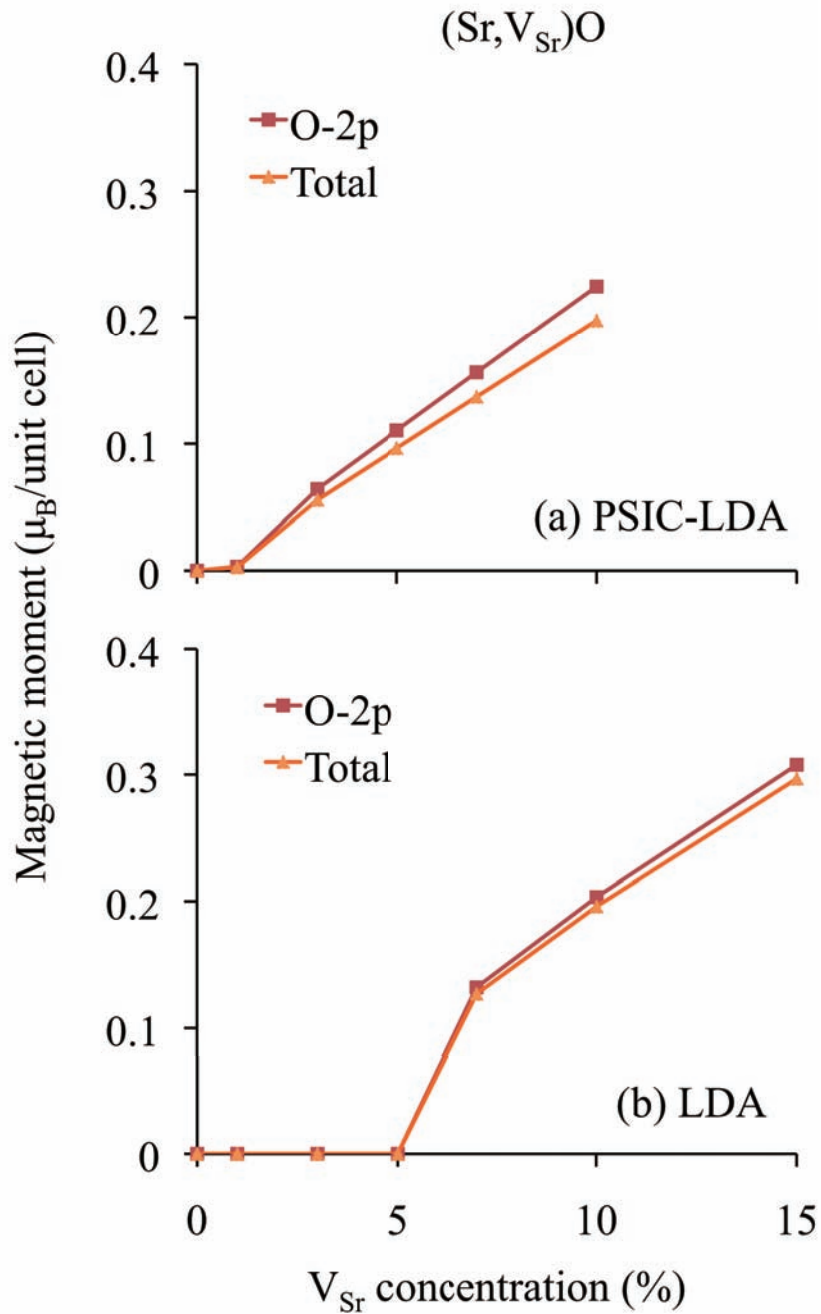
Figure 4.7: Calculated magnetic moments of $(Sr, V_{Sr})O$ by (a) PSIC-LDA and (b) LDA. The result of PSIC-LDA for 15% is not shown because of the calculation instablity.

### 4.1.3 Curie Temperature with Consideration of Magnetic Percolation

To evaluate the percolation effect of ferromagnetic coupling, the magnetic exchange coupling constants between sites $i$ and $j$ ($J_{ij}$) were calculated using Liechtenstein's formula [18]. This theory assumes a CPA effective medium as a reference to calculate the effective magnetic interactions mapped on the classical Heisenberg model. The $J_{ij}$s were calculated from the total energy change resulting from the rotation of the two magnetic moments at $i$ and $j$ in the effective medium, which was calculated in the previous section (see Appendix for more details).

In the present DMSs, effective exchange interactions between magnetic sites were short ranged and contributions mostly from those of the first- or second-nearest neighbors (Fig. 4.8 and 4.9). Interestingly, by increasing the lattice constant from MgO to CaO and SrO, the role of the second-nearest neighbors ($J_{02}$) became more important.

This result may be caused by the sufficiently large distances between the first-nearest neighbors, while the interactions between the second-nearest atoms easily occur through the mediating atoms with large ionic radii. A unique feature of the vacancy-doped systems is that they invoke long-range magnetic correlation while N-doped systems form short-range magnetic correlation. In magnetic-element-doped DMSs, such as (Ga,Mn)N, the local magnetic moments originate from dopants, and magnetic interactions are often short-ranged and dominated by nearest-neighbor exchange interactions [16]. This short-range magnetic interaction results in overestimation of $T_C$ by the MFA at low concentrations below a percolation threshold for DMSs [16, 20]. For instance, if we focus only on nearest-neighbor interactions, the percolation threshold is 20% for the face-centered cubic structure [16]. In (Mg,V$_{Mg}$)O, (Ca,V$_{Ca}$)O and (Sr,V$_{Sr}$)O, the calculated exchange interactions between O atoms are short ranged. However, unlike the magnetic-element-doped DMSs, in these systems, the local magnetic moments originate not from the dopants but from the O $2p$ orbitals of the host material. Therefore, due to the high O concentration, magnetic correlation in the present system should be long-ranged. This long-ranged correlation ensures validity of MFA applied in this study for the calculation of $T_C$.

Next, the $T_C$s were estimated using the calculated exchange interactions. For a system with long-range magnetic correlations, MFA was used to estimate $T_C$ in the following equation,

$$k_{\mathrm{B}} T_{\mathrm{C}}^{\mathrm{MFA}} = \frac{2x}{3} \sum_{i \neq 0} J_{0i}, \qquad (4.1)$$

where $k_{\mathrm{B}}$ is the Boltzmann constant and $x$ is the concentration of the magnetic atoms. For a system with long-range magnetic correlations, a MC simulation was performed [16] to account for magnetic percolation and thus avoid overestimation of $T_C$. In the simulation, the thermal average of magnetization M and its powers were calculated using the Metropolis algorithm. Due to the finite size of the super cells used in the simulation, determination of $T_C$ from the temperature dependence $<M(T)>$ is difficult. For this reason, we used the cumulant crossing method as proposed by Binder [19], because the fourth-order cumulant $U_4$ (a linear combination of $<M^4>/<M^2>^2$) have a size-independent and universal fix-point at $T_C$. This MC simulation has been shown to provide a practical estimation accuracy for DMSs with short-ranged magnetic correlation and homogenously distributed impurities, such as (Ga,Mn)As [20]. For the estimation of $T_C$ using MC simulation, $U_4$ for different cell sizes of $6 \times 6 \times 6$, $10 \times 10 \times 10$, and $14 \times 14 \times 14$ conventional fcc cells were calculated as a function of temperature. Part of the details of the calculation procedure employed in the present study [20], along with the calculated results of $d^0$ ferromagnets [69, 56, 57], are found in previously reported studies.

The estimated $T_C$ under the homogeneous distribution condition increased linearly as a function of doping concentrations and reached room temperature at sufficient doping concentrations; i.e., 15% for $(\mathrm{Mg},\mathrm{V}_{Mg})\mathrm{O}$, 20% for $\mathrm{Mg}(\mathrm{O},\mathrm{N})$ and 30% for $\mathrm{Ca}(\mathrm{O},\mathrm{N})$ and $\mathrm{Sr}(\mathrm{O},\mathrm{N})$ (Fig. 4.10). To estimate $T_C$, we used MC simulations for N-doped systems, where magnetic correlations are short-ranged, and the MFA for vacancy-doped systems, where magnetic correlations are long-ranged. The significance of considering the magnetic percolation effect in the estimation of $T_C$ was also confirmed; the $T_C$ values calculated using the MC simulation were much lower than those calculated with the MFA in the N-doped systems (Fig. 4.11). Since the atomic positions could be significantly shifted with high vacancy concentrations, and lattice relaxation was not taken into account by the KKR-CPA method used in this calculation, the maximum doping concentration for the vacancy-doped systems was set to relatively small values compared to those of the N-doped systems.
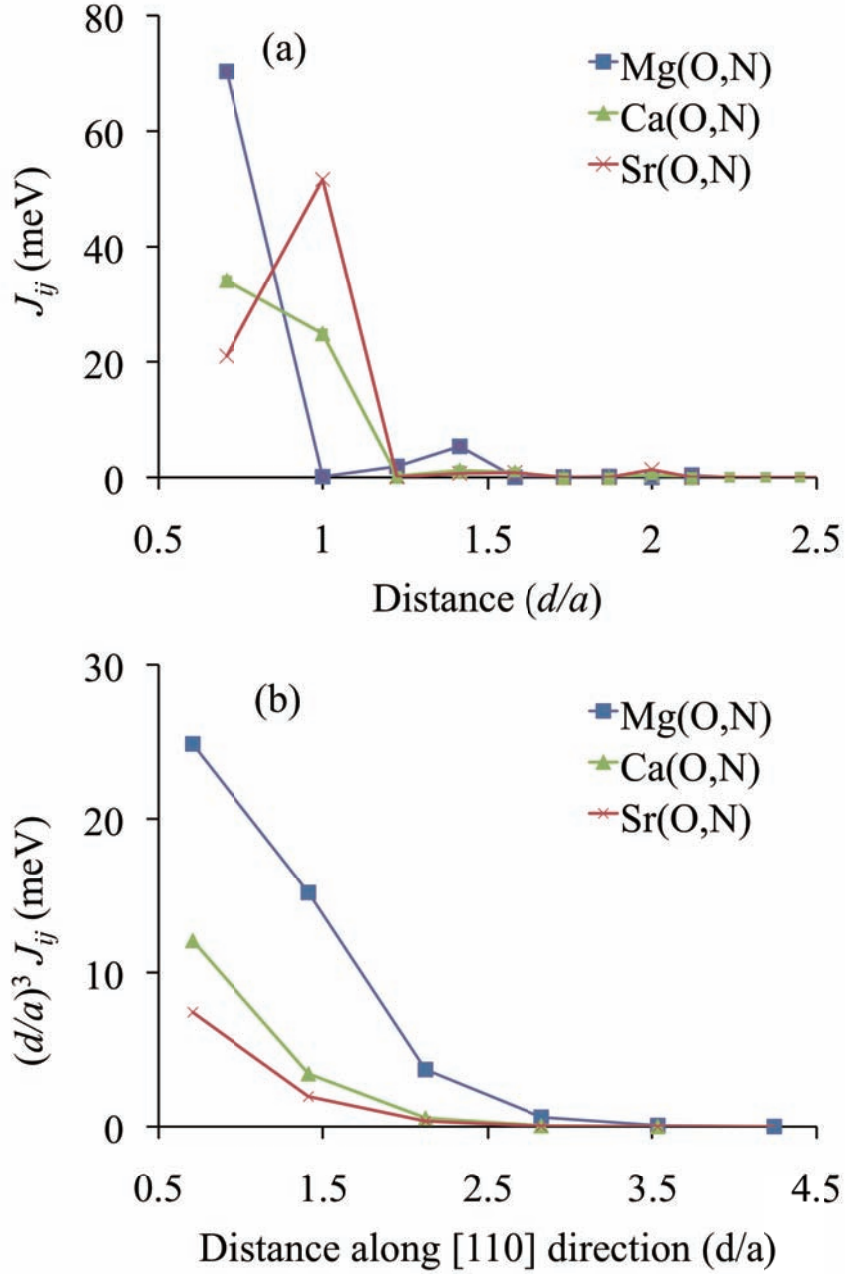
Figure 4.8: Effective exchange interaction between N atoms ($J_{ij}$) in Mg(O,N), Ca(O,N) and Sr(O,N). The exchange interactions (a) regardless of direction and (b) along the dominating [110] direction the exchange interactions scaled by the RKKY-like factor $(d/a)^3$ are shown.
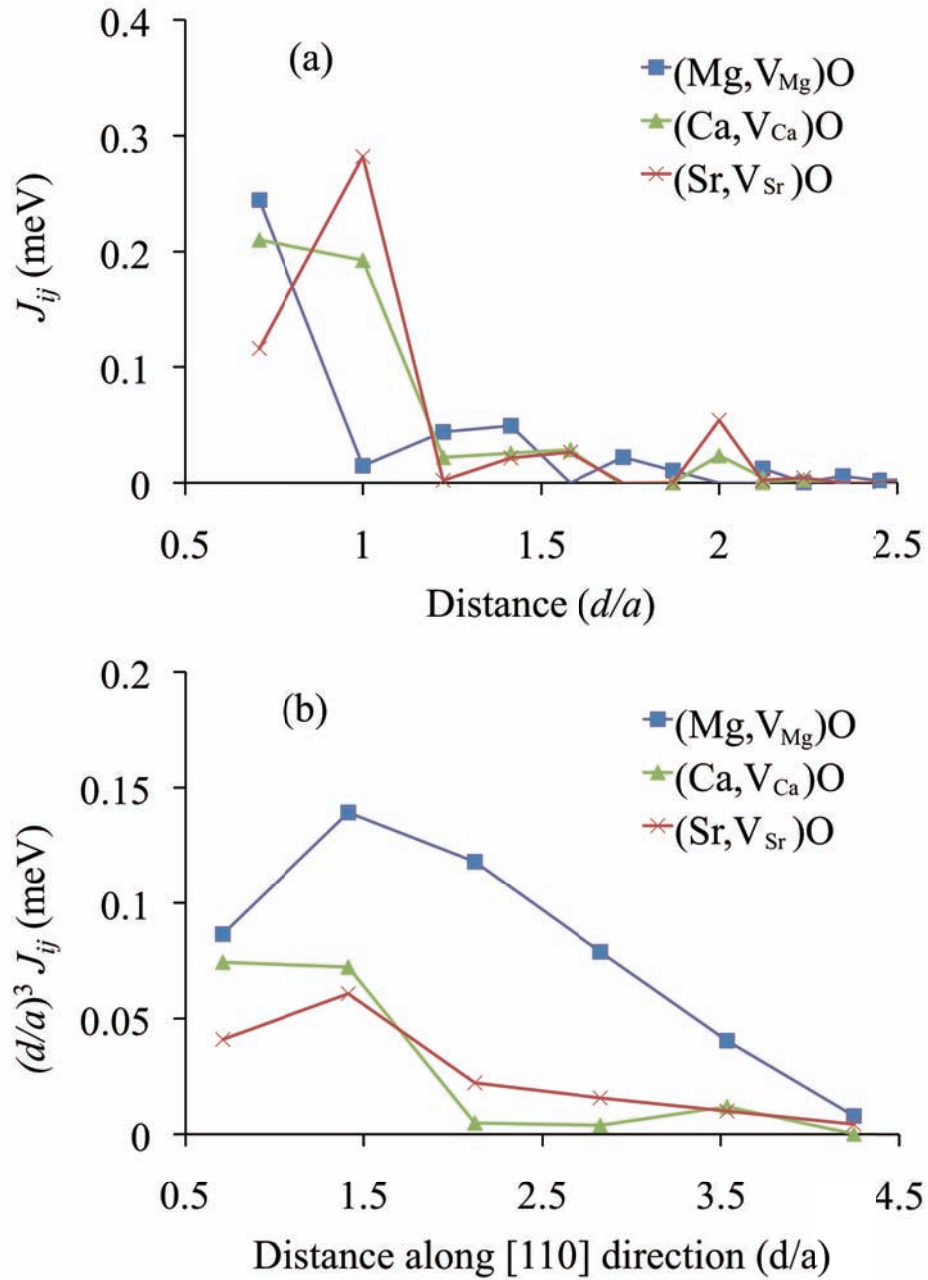
Figure 4.9: Effective exchange interaction between O atoms $(J_{ij})$ in $(Mg,V_{Mg})N$, $(Ca,V_{Ca})N$ and $(Sr,V_{Sr})N$. The exchange interactions (a) regardless of direction and (b) along the dominating [110] direction the exchange interactions scaled by the RKKY-like factor $(d/a)^3$ are shown.
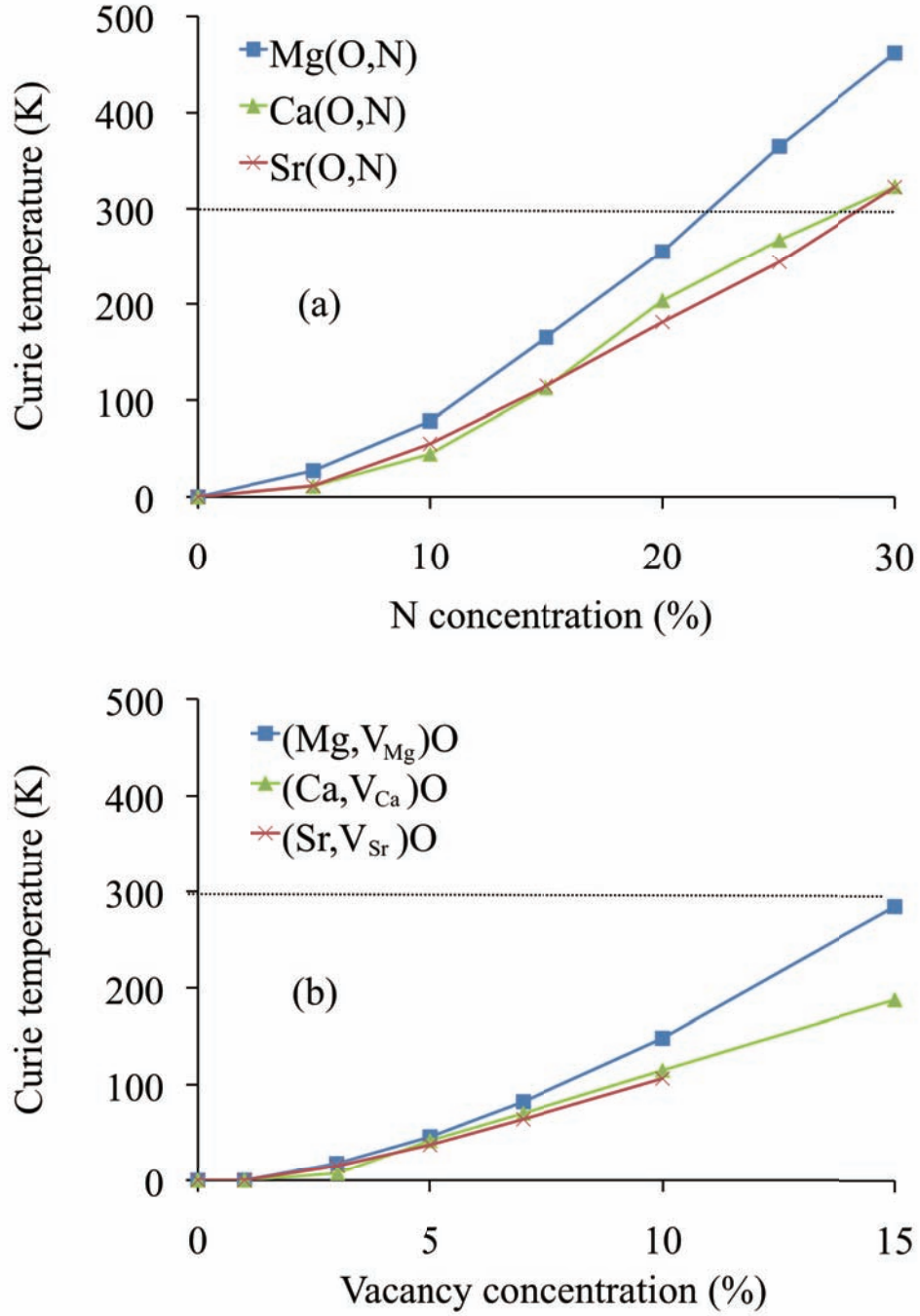
Figure 4.10: Estimated $T_C$ of (a) Mg(O,N), Ca(O,N) and Sr(O,N) using MC simulation and (b) $(Mg,V_{Mg})O$, $(Ca,V_{Ca})O$ and $(Sr,V_{Sr})O$ by the MFA.
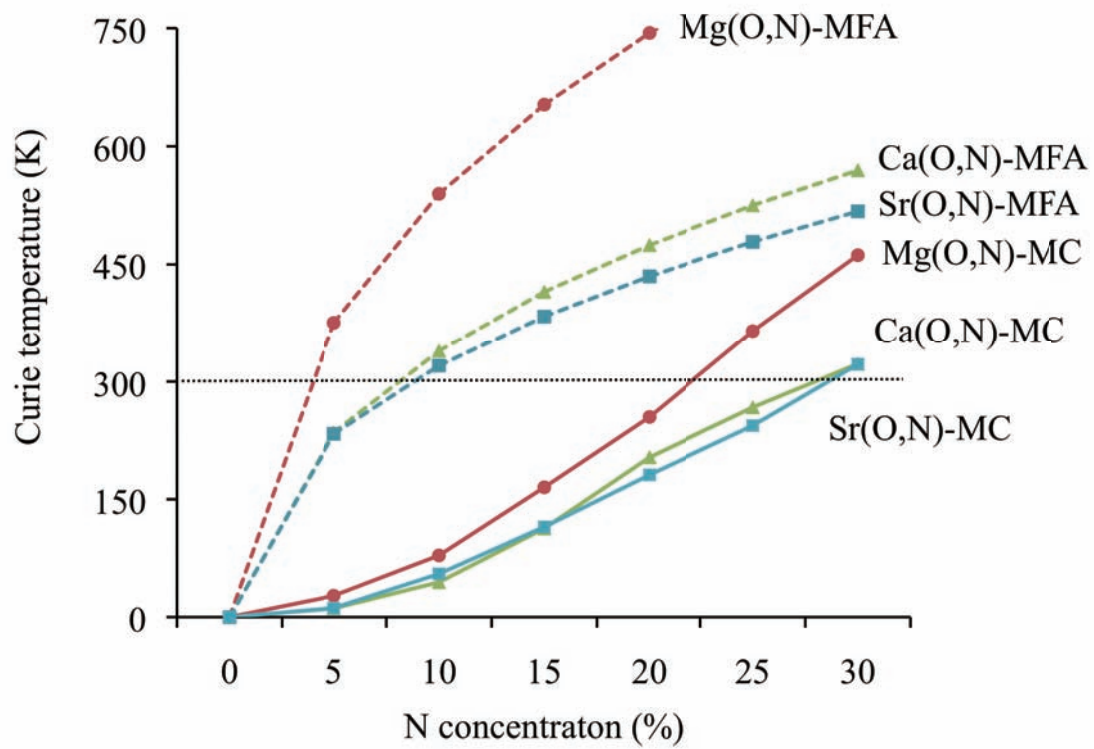
Figure 4.11: Estimated $T_C$ of Mg(O,N), Ca(O,N) and Sr(O,N) using MC simulation
and the MFA.

## 4.2 Analysis of Inhomogeneity

Thus far, we have discussed magnetic properties under the assumption that dopants are homogenously distributed at assigned sites. Hereafter, a favored configuration of dopant distribution is investigated. In this section, the calculation procedure consists of two steps: (i) calculation of chemical pair interactions between two dopants and (ii) simulation of the potential configuration of inhomogeneous dopant distribution, using the calculated chemical pair interactions.

### 4.2.1 Chemical Pair Interaction

To evaluate the homogeneity of dopant distribution, chemical pair interactions between dopants at sites $i$ and $j$ ($V_{ij}$) were calculated. A basic structure of a unit cell for the present calculation was constructed using a $2 \times 2 \times 2$ supercell, containing 32 M and 32 O atoms ($M_{32}O_{32}$) within a rock salt structure, where M represents Mg, Ca or Sr. To calculate the chemical pair interactions, the total energies of the host material ($E(X_{32}O_{32})$), the supercell with a single dopant ($E(M_{32}O_{31}N_1)$ and $E(M_{31}V_{M1}O_{32})$) and the supercell with two dopants ($E(M_{32}O_{30}N_{2-ij})$ and $E(M_{30}V_{M2-ij}O_{32})$) were calculated where $i$ and $j$ represent the dopant sites in the unit cell (Fig. 4.12). The chemical pair interactions between the dopants at sites $i$ and $j$ ($V_{ij}$) were calculated using the calculated total energies, defined as $E(M_{32}O_{32}) + E(M_{32}O_{30}N_{2-ij})$ - $2E(M_{32}O_{31}N_1)$ for N-doped systems and $E(M_{32}O_{32}) + E(M_{30}V_{M2-ij}O_{32})$ - $2E(M_{31}V_{M1}O_{32})$ for vacancy-doped systems. By definition of the total energies, a negative $V_{ij}$ indicates an attractive interaction, and a positive $V_{ij}$ indicates a repulsive interaction between the dopants. In the supercell with two dopants, five different configurations of dopant distributions may exist (configurations of the 1st, 2nd, 3rd, 4th and 6th nearest neighbors between dopants). The corresponding concentrations of the dopants were 3.125% for a single dopant and 6.25% for two dopants in the unit cell, respectively. The energies of the host material and the other configurations were calculated in a non-magnetic state and a ferromagnetic state, respectively. The energies of different configurations were calculated using the projector augmented wave (PAW) method [70] and the generalized gradient approximation (GGA) [71, 72] exchange-correlation functional (PAW-GGA). The VIENNA AB INITIO SIMULATION PACKAGE (VASP) was used for the PAW-GGA calculations [73, 74]. An experimentally determined lattice constant for the rock-salt structure (a = 4.21 Å [67]) was used. During optimization, all of the atoms were relaxed until the Hellman-Feynman force on each ion was less than 0.01 eV/Å. An energy cutoff of 400 eV was set for the plane-wave basis. For the Brillouin-zone

sampling, a Monkhorst-Pack $k$ mesh was used for structural optimization.

After relaxation, the atoms closest to the dopant moved outward, and the second closest atoms moved inward after relaxation. Relaxations from the original positions were relatively small, even for vacancy-doped systems at a concentration of 6.25% (Table 4.1). The maximum changes from the original atomic positions were approximately 0.1 Å in the N-doped systems and 0.3 Å in the vacancy-doped systems.

Strong attractive interactions occurred between the 1st nearest neighbors in Mg(O,N), the 1st and 2nd nearest neighbors in Ca(O,N) and Sr(O,N) and the 2nd nearest neighbors in $(Mg,V_{Mg})O$ (Fig. 4.13); these materials favored phase separation due to the attractive pair interactions. In contrast, interactions are relatively weak and mainly repulsive in $(Ca,V_{Ca})O$ and $(Sr,V_{Sr})O$.

These materials of Mg(O,N), Ca(O,N), Sr(O,N) and $(Mg,V_{Mg})O$ favor phase separation because of the attractive pair interactions. During crystal growth, self-organized nanoclusters can be formed via spinodal if related temperatures are high enough for a sufficiently long time. As a whole, pair interactions are strongest in MgO-based systems and smallest in SrO-based systems.

Once pair interactions are determined, we can simulate a potential configuration of dopant distributions under the decomposition process by using the standard MC algorithm [26, 27]. In the next section, we will discuss the simulation results of crystal growth for selected materials.
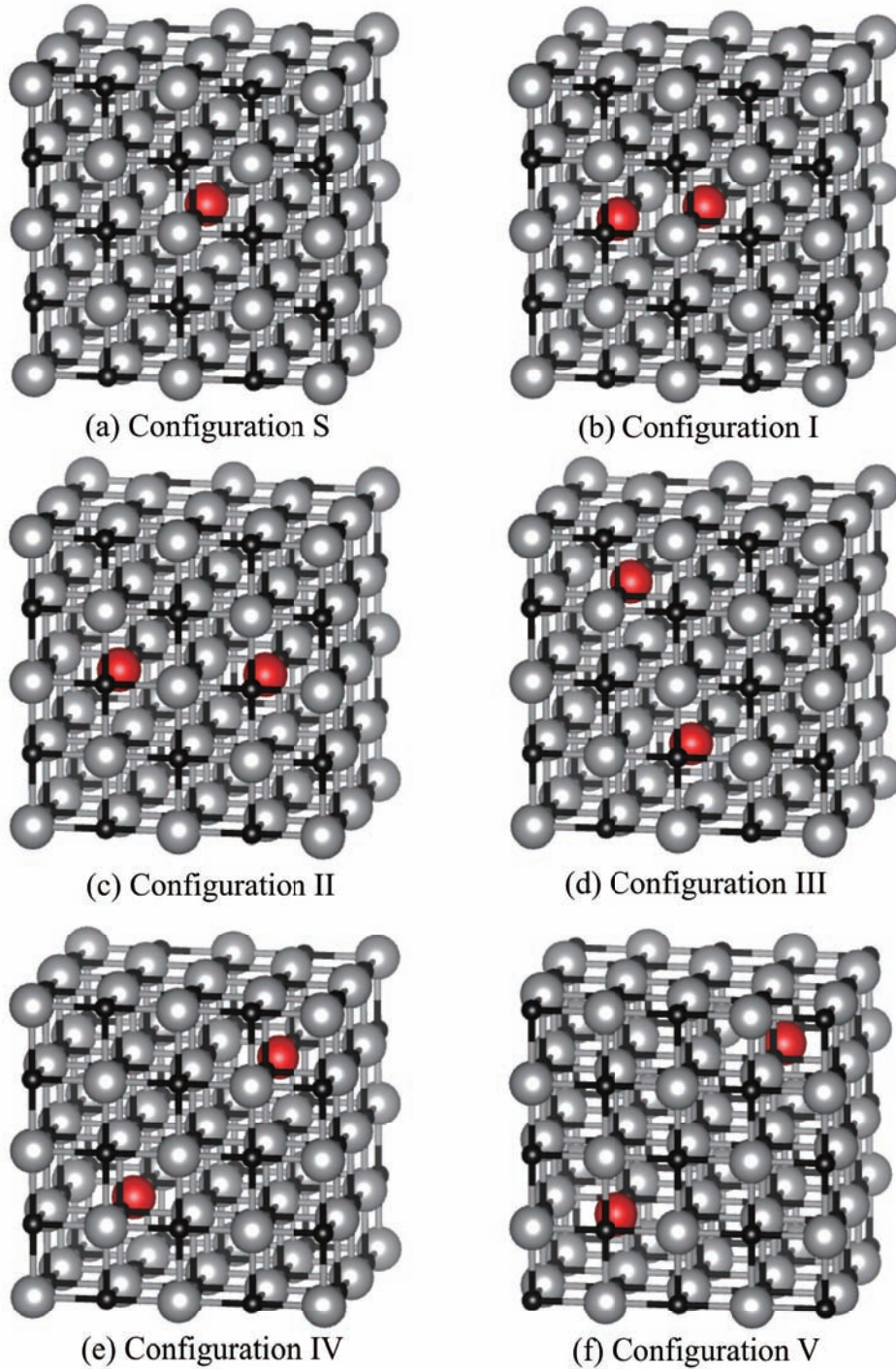
Figure 4.12: Dopant distribution of configurations consisting of 64 supercells. The red spheres represent a dopant. The small black and large gray spheres represent cations or anitons, respectively. S represents a configuration with a single dopant in the unit cell. I, II, III, IV and V represent configurations with two dopants in the unit cell. Smaller numbers imply a smaller distance between dopants. The VESTA visualization program [59] was used to prepare this image.

| | Configuration | | | | | |
|---|---|---|---|---|---|---|
| | **S** | **I** | **II** | **III** | **IV** | **V** |
| Mg(O,N) | 0.51% (0.02Å) | 1.77% (0.07Å) | 0.72% (0.03Å) | 1.09% (0.04Å) | 0.56% (0.02Å) | 0.45% (0.01Å) |
| Ca(O,N) | 0.58% (0.02Å) | 1.86% (0.08Å) | 0.80% (0.03Å) | 0.73% (0.03Å) | 0.73% (0.03Å) | 0.52% (0.02Å) |
| Sr(O,N) | 0.62% (0.03Å) | 1.12% (0.05Å) | 0.86% (0.04Å) | 0.76% (0.03Å) | 0.54% (0.02Å) | 0.56% (0.02Å) |
| $(Mg,V_{Mg})O$ | 2.53% (0.10Å) | 3.77% (0.15Å) | 2.03% (0.08Å) | 2.54% (0.10Å) | 2.32% (0.09Å) | 2.34% (0.09Å) |
| $(Ca,V_{Mg})O$ | 3.16% (0.15Å) | 4.74% (0.22Å) | 3.03% (0.14Å) | 3.27% (0.15Å) | 3.27% (0.15Å) | 3.07% (0.14Å) |
| $(Sr,V_{Mg})O$ | 3.58% (0.18Å) | 5.50% (0.28Å) | 3.69% (0.19Å) | 3.82% (0.19Å) | 3.62% (0.18Å) | 3.55% (0.18Å) |

Table 4.1: Maximum changes from the original atomic positions after relaxation are shown as a ratio to the lattice constant (%) and as an absolute value (Å). Configuration S represents a configuration with a single dopant in the unit cell. Configurations I, II, III, IV and V represent configurations with two dopants in the unit cell and smaller numbers imply a smaller distance between dopants, i.e., configuration I has dopants at nearest neighbor sites.
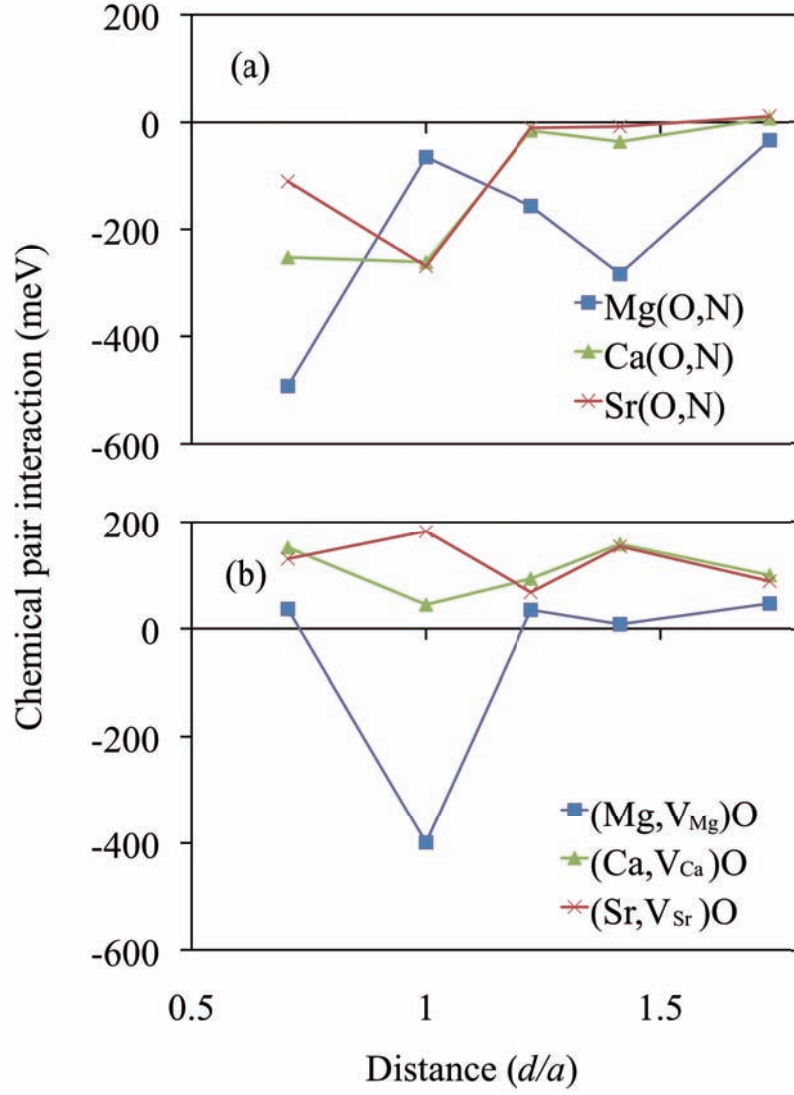
Figure 4.13: Chemical Pair Interaction (a) between N atoms in Mg(O,N), Ca(O,N) and Sr(O,N) and (b) between vacancies in $(Mg,V_{Mg})O$, $(Ca,V_{Ca})O$ and $Sr(V_{Sr},O)$.

## 4.2.2 Self-Organized Nanostructures

MC simulations of crystal growth under a layer-by-layer condition were performed based on the calculated chemical pair interactions and by using a previously proposed scheme [27]. For this simulation, the Ising model was used to describe the energetics of the systems,

$$H = (-1/2) \sum_{i \neq j} V_{ij} \sigma_i \sigma_j, \tag{4.2}$$

where $\sigma_i$ is the occupation number of the dopant at site $i$. In layer-by-layer crystal growth, as realized in molecular-beam epitaxy (MBE), metal-organic vapor-phase epitaxy (MOVPE) and metal-organic chemical-vapor deposition (MOCVD), atomic diffusion is restricted to the surface layer. Assuming ideal layer-by-layer growth, atomic diffusion was restricted to the surface in the present simulation; i.e., only the nearest neighbor sites on the same surface were used as candidate trial sites (e.g., one of the four sites in the fcc (100) plane). The first layer was deposited with a random distribution of component atoms and was annealed at a certain temperature using the Metropolis algorithm. In the algorithm, the probability of a certain dopant moving to a randomly selected trial site was determined by an energy difference between the original position and the trial position, i.e., the trial motion is accepted with a probability ($P$) defined as

$$P(\Delta E) = \min \left(1, \exp \left(-\Delta E / k_{\mathrm{B}} T\right)\right), \tag{4.3}$$

where $\Delta E$ is the energy difference caused by the trial motion. One MC step required movement to every dopant site. After starting a MC loop, the system relaxed toward thermal equilibrium. The MC sequence was interrupted after a certain step to predict a potential configuration of dopant distribution in a non-equilibrium state. After simulation of the first layer, the configuration of the layer was fixed. Next, the second layer was deposited. Simulation of the 2nd layer configuration was performed under the condition that only the 2nd layer was annealed (or diffused). After simulation of the second layer, the configuration of the second layer was fixed, and the third layer was deposited. By repeating this process for the required number of layers, potential configurations for layer-by-layer growth conditions were predicted. The initial positions of atoms in each surface layer were randomly set before annealing, and only substi-

tutional doping was considered in the present calculations. The doping concentration was fixed to 5% for all of the calculations, and $20 \times 20 \times 20$ conventional fcc cells with 1600 dopants were defined as a simulation box. Simulations were performed at a scaled temperature of $k_B T / \max(V_{ij}) = 0.4$ for each calculation. This corresponded to approximately 2300 K for Mg(O,N), 1200K for Ca(O,N), 1250K for Sr(O,N) and 2050 K for (Mg,$V_{Mg}$)O. The $V_{ij}$ from the 1st to 4th nearest neighbors were taken into account. The Monte Carlo sequence to anneal each layer was interrupted after 5000 steps for N-doped systems and after 50000 steps for (Mg,$V_{Mg}$)O.

The MC simulation showed that self-organized nanostructures of the dopants can be formed under the layer-by-layer growth condition. In Mg(O,N), Ca(O,N), Sr(O,N) and (Mg,$V_{Mg}$)O, nano-scale clusters with quasi-one-dimensional structures appeared (Fig. 4.14). Under the layer-by-layer condition, dopants could not leave their initial planes due to the attractive interactions between dopants; thus, the shape of the cluster was spontaneously controlled resulting in a quasi-one-dimensional shape. Reflecting the characteristics of the strongest attractive pair interactions, the spatial occupation of a Konbu phase was larger for (Mg,$V_{Mg}$)O than for N-doped systems. We call this a one-dimensional-Konbu phase, where Konbu means seaweed in Japanese.
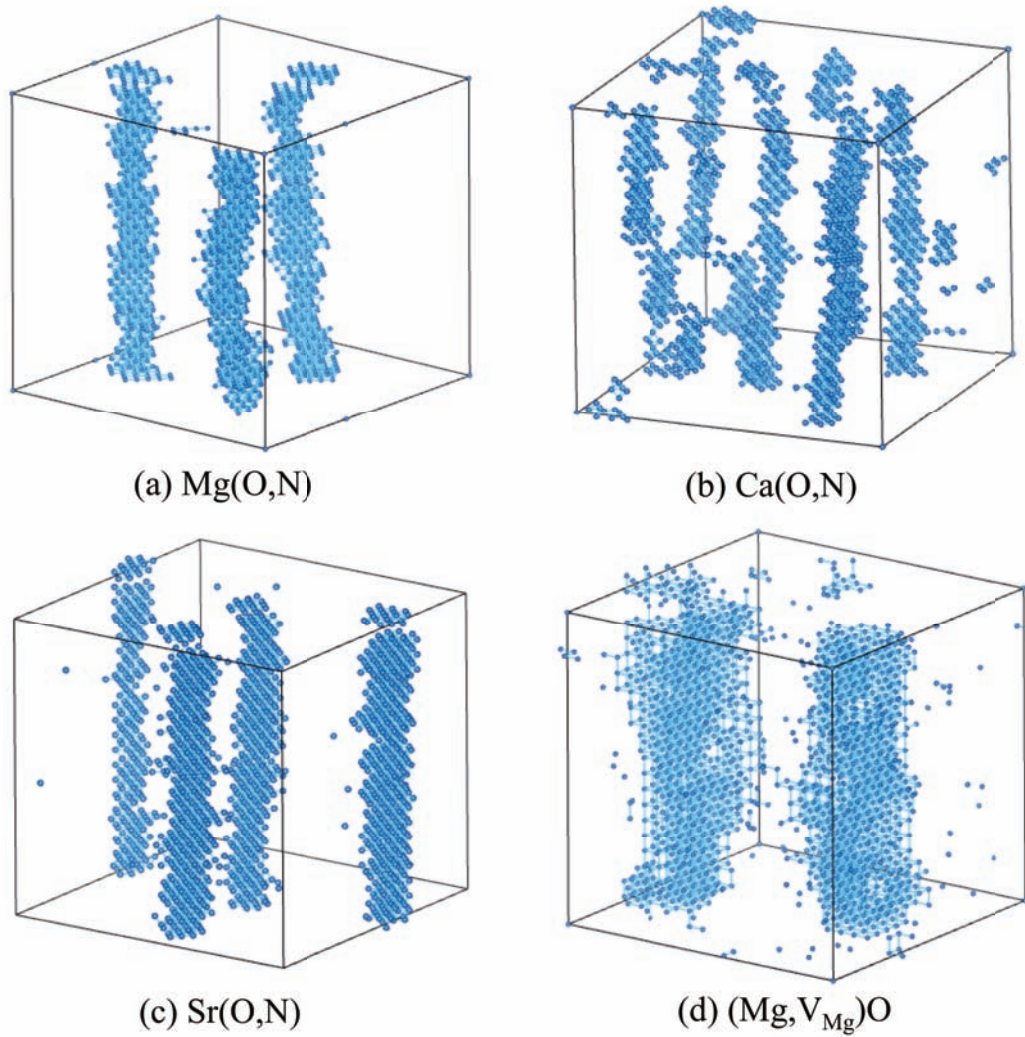
Figure 4.14: Predicted configurations under the layer-by-layer crystal growth condition for (a) Mg(O,N), (b) Ca(O,N), (c) Sr(O,N) and (d) (Mg,V$_{Mg}$)O. Only the distribution of dopants is shown in the figure. The lines between dopants represent 1st nearest neighbor bonds for the N-doped systems and 2nd nearest neighbor bonds for (Mg,V$_{Mg}$)O. The dopant concentration is 5%. The VESTA visualization program [59] was used to prepare this image.

### 4.2.3 Superparamagnetism

Formation of the Konbu-phase nanoclusters allowed high dopant concentrations to be achieved within these clusters. The Konbu-phase clusters became ferromagnetic even if the ferromagnetic exchange interaction was short-ranged. In contrast, the dopant concentrations outside the clusters were lower than the average doping concentration, and the ferromagnetic interaction between the clusters weakened as a result of the short-range exchange interaction. In this type of Konbu-phase system, when clusters are large enough, a super-paramagnetic blocking phenomenon dominates the magnetization process. High blocking temperatures (high-$T_B$) can be achieved, as a result [25, 26, 27, 28].

To flip the magnetization direction of the cluster, the magnetic anisotropy energy must be overcome. An energy barrier due to magnetic (or shape) anisotropy results in a finite relaxation time for reversal of the magnetization. The relaxation time, $\tau$, follows the relation $1/\tau \propto exp(\text{-}KV/k_BT)$, where $K$, $V$, $T$, and $k_B$ are the anisotropy constant, volume of the cluster, temperature and Boltzmann constant, respectively. This relation shows that the relaxation time increases with cluster size. When the relaxation time is longer than the observation time for the magnetization process, a hysteresis loop is observed in the magnetization curve, even in the absence of ferromagnetic correlation between clusters, and $T_C$ of the entire system is practically zero. This phenomenon is called super-paramagnetic blocking [25].

Temperature dependence of magnetization can be calculated by increasing temperature under a small external magnetic field for (i) parallel and (ii) anti-parallel, with respect to the external field, initial configurations of the magnetization [75, 28]. $T_B$ is defined as the temperature at which the magnetization flips from an initially anti-parrallel to a parrallel configuration. In Fig. 4.15, $T_B$ corresponds to the temperature at which the lines representing each configuration coincide with each other. It has been shown that $T_B$ is significantly enhanced by the formation of magnetic clusters (Fig. 4.15).

Recent experiments have reported room-temperature ferromagnetic behavior in MgO thin films with no magnetic elements. For example, ferromagnetism in 13%-N-doped MgO prepared via MBE has been observed [50]. Ferromagnetism induced by a few percent of Mg vacancies in MgO, prepared with sputtering in an O atmosphere, has also been reported [76, 77]. However, as shown in our previous studies [57, 56], doping concentrations of 13% for Mg(O,N) and a few percent for $(Mg,V_{Mg})O$ are not sufficient enough to induce ferromagnetism under homogenous distribution conditions; under homogeneous conditions, 20% and 15% doping concentrations are required for

room-temperature ferromagnetism in Mg(O,N) and (Mg,$V_{Mg}$)O, respectively. Since these systems energetically favor to form nanoclusters of dopants and there are large discrepancies in $T_C$ between our theoretical estimations under the homogeneous conditions and the aforementioned experiments, it is strongly suggested that the magnetic properties observed in the hysteresis curves obtained for Mg(O,N) and (Mg,$V_{Mg}$)O in previous experimental studies originate from the super-paramagnetic blocking phenomenon.
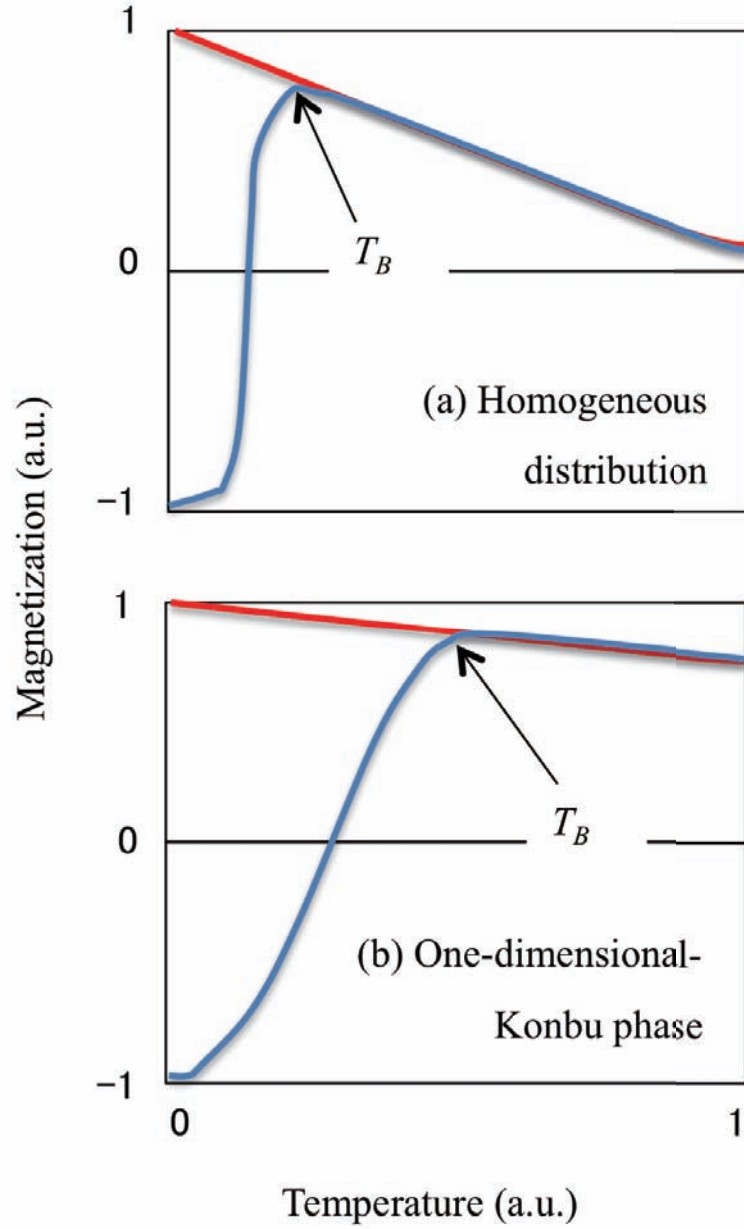
Figure 4.15: Schematic picture of the super-paramagnetic blocking phenomenon. Magnetization is shown as function of temperature. The initial configuration of magnetization is either parallel (red lines) or anti-parallel (blue lines) with respect to the external field for the cases of (a) homogeneous distribution and (b) one-dimensional-Konbu phase. Temperature and external field are scaled in arbitral units.

## 4.3 A Unified Picture of Mechanism for $d^0$ Ferromagnetism

This study reveals that the origin of $d^0$ ferromagnetism can be understood as follows: (i) local magnetic moments are spontaneously formed by $p$ bands narrow enough to satisfy the splitting condition ($U \geq W$), and (ii) ferromagnetic states are stabilized due to the kinetic-energy gain of itinerant spin-polarized electrons, which results from partial occupation of the $p$ bands (Fig. 4.16). The $d^0$ ferromagnets can be classified into anion-substituted and cation-substituted groups [63]. In anion-substituted group, anions of semiconductors or insulators are substituted by impurities of smaller valency, and spin-polarized impurity $p$ bands are introduced into the band gap. The magnetic properties of this group are characterized by strong exchange interactions between dopants and short-ranged magnetic correlation. In cation-substituted group, cations are substituted by vacancies or impurities of smaller valency, and valence bands are mainly composed of $p$-orbitals that exhibit spin-polarization. In contrast to the anion-substituted group, the magnetic properties of cation-substituted group are characterized by weak exchange interactions between dopants and long-ranged magnetic correlation. Although their electronic structure and magnetic properties of the two groups are quite different, the mechanism of $d^0$ ferromagnetism can be understood from the same point of view.
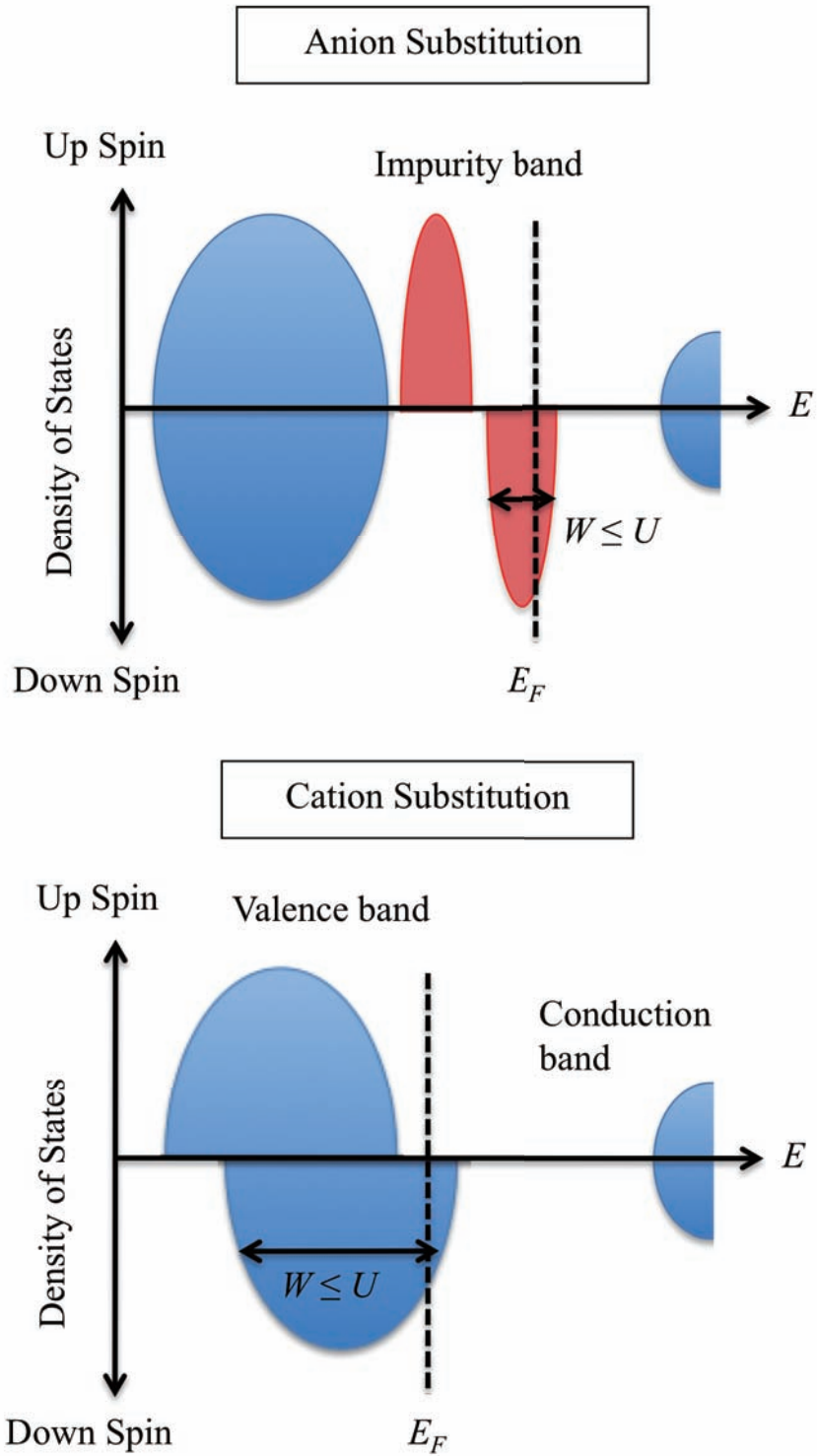
Figure 4.16: Schematic diagram of the electronic structures of $d^0$ ferromagnets

# Chapter 5

# Summary

$d^0$ ferromagnetism refers to a new class of magnetism, wherein the ferromagnets contain no magnetic elements, and has created significant interest in DMSs. Based on first-principles calculations, this study showed that materials such as Si- or Ge-doped $K_2S$ and C- or N-doped CaO, MgO or SrO can exhibit ferromagnetism. As the earliest candidates, $K_2$(S,Si) and $K_2$(S,Ge) were proposed for $d^0$ ferromagnets, in which their deep impurity bands consisted of $3p$ orbitals introduced in the bandgap with partially filled $3p$ shells and stabilized ferromagnetic states. This idea was also applied to $2p$ orbitals in Ca(O,C) and Ca(O,N), and the idea was generalized to design other alkaline-chalcogenide- or alkaline-earth-metal-oxides-based $d^0$ ferromagnets, including the C- or N-doped MgO, SrO and BaO. Thereafter, experimental work has validated that room-temperature ferromagnetic behavior is exhibited by N-doped MgO. In the latest comprehensive analysis, MC simulations of the dopant distribution based on the calculated chemical pair interactions between dopants revealed that Mg(O,N), Ca(O,N), Sr(O,N) and $(Mg,V_{Mg})O$ can form nanoscale superparamagnetic clusters of dopants with strong ferromagnetic coupling in the clusters. and these materials can exhibit high-$T_B$. Furthermore, by considering the estimated Curie temperatures under a condition of homogeneous dopant distribution, the room-temperature magnetic hysteresis in MgO thin films with 13% N impurities and a few percent of Mg vacancies observed in previous experimental reports was shown to originate from the super-paramagnetic blocking phenomenon resulting from self-organized nanostructures. The significance of the SIC is also shown: to calculate the proper electronic structures of $d^0$ ferromagnets, beyond-LDA methods such as the PSIC are essential because the LDA underestimates $U$, and this underestimation causes an instability of the magnetic states. Finally, this study revealed that the origin of $d^0$ ferromagnetism can be understood as follows: (i) local magnetic moments are spontaneously formed by narrow $p$ bands, and (ii) ferromagnetic states are stabilized due to the kinetic energy gained from itinerant

spin-polarized electrons, which result from partial occupation of the $p$ bands.

The significance of this study is in (i) pioneering the computational materials design of $d^0$ ferromagnets, which has greatly contributed to developments in this novel research field, (ii) presenting the materials design of $d^0$ ferromagnets aimed at achieving high-$T_B$ and (iii) elucidating the magnetic properties and mechanisms associated with $d^0$ ferromagnetism. These series of research outcomes not only provide an essential understanding of $d^0$ ferromagnetism but also open a new route to creating environmentally friendly materials for spintronics without the use of magnetic elements.

# Appendix

## A.1   Self-Interaction Correction

The Kohn-Sham approach to density-functional theory (DFT-KS) using the LDA has been surprisingly successful in investigating the electronic structures of various classes of materials. However, the LDA is known to have systematic errors, such as the overbinding error and the underestimation of bandgaps. These errors become marked especially noticeable in the calculation of highly correlated systems, such as oxide-based DMSs, and can lead to even qualitative misunderstandings of the systems. For accurate investigations of DMS systems, an approach that improves upon these errors is required.

These errors can be significantly improved by introducing a simple correction to the DFT-KS-LDA calculation scheme. In this study, we employed the pseudo-SIC (PSIC) method, which was originally developed by Filippetti and Spaldin [34]. This method was modified and implemented in a code based on the KKR method by Toyoda [32] because the KKR method combined with CPA is useful for investigating disordered systems such as DMS systems.

In the DFT-KS-LDA scheme, the states considered are those of the non-interacting particles moving in a one-body effective potential. The Coulomb interaction acting among the real electrons is taken into account in the effective potential, which is given by the variation of the electron-electron interaction energy described as

$$E_{ee}[n] = U[n] + E_{XC}[n]. \tag{A.1}$$

Here, the first term is the Hartree (electrostatic Coulomb interaction) term and the second term is the exchange-correlation term. The Hartree term is given by

$$U[n] = \frac{1}{2} \iint \frac{n(\boldsymbol{r})n(\boldsymbol{r}')}{|\boldsymbol{r} - \boldsymbol{r}'|} \, d^3r d^3r'. \tag{A.2}$$

Because the exact description as a function of the local densities is unknown, the

exchange-correlation term is replaced by an approximated function that is often obtained from the LDA.

The exact electron-electron interaction energy, $E_{ee}$, with the exchange-energy, $E_{XC}$, must yield precisely zero energy whenever the density n(r) represents a density of one-electron states. The Hartree term and the exchange-correlation term for one-electron states must cancel each other out. Within the LDA, however, this cancellation cannot be treated properly, and a spurious interaction energy is produced. This unphysical energy is called the self-interaction error (SIE). The SIE for an orbital labeled by index $i$ with the charge density $n_i(r)$ is given by

$$\delta_i = U[n_i] - E_{XC}^{LDA}[n_i] \tag{A.3}$$

where $E_{XC}^{LDA}[n]$ is the approximated LDA exchange-correlation energy.

In the original SIC method proposed by Perdew and Znuger [33], the unphysical SIE of all the occupied orbitals are simply subtracted from $E_{ee}[n]$:

$$E_{ee}^{SIC}[n] \equiv U[n] + E_{XC}^{LDA}[n] - \sum_{i}^{occ.} \delta_i, \tag{A.4}$$

where $\sigma$ is the index of spin and $i$ is the site index. The SIC total energy is then minimized by solving the following equations:

$$\left[ -\nabla^2 + v_i^{SIC} \right] \phi_i(\boldsymbol{r}) = \epsilon_{a,\sigma}\phi_i(\boldsymbol{r}), v_i^{SIC} \equiv v^{LDA}[n] - \left( u[n_i] + v_{XC}^{LDA}[n_i] \right), \tag{A.5}$$

where $v^{LDA}[n]$ is the LDA effective potential, $u[n]$ is the Hartree potential (given by the variation of $U$) and $v_{XC}^{LDA}[n]$ is the exchange-correlation potential (given by the variation of $E_{XC}^{LDA}[n]$).

The straightforward application of the SIC method to extended systems, however, requires large computational efforts because the SIC charge density is solved in real space to use localized orbitals, while the electronic structure is solved in reciprocal space; i.e., back-and-forth transformations between real and reciprocal space are required for every iteration. Furthermore, because the screening effect on the Coulomb interaction is not taken into account, the full correction by the SIC method generally results in an overcorrection, e.g., the band-gaps become too large, and the eigenvalues of the localized orbitals are too low in energy. In the pseudo-SIC method, these problems are avoided by modifying the SIC potential to be expressed in terms of nonlocal projector operators and by introducing a pre-scaling factor to the SIC potential. In the

implementation combined with the KKR-CPA method, the SIC potential is calculated using the angular-momentum-decomposed charge density in the muffin-tin spheres of each site:

$$n_L^i(\boldsymbol{r}) = \frac{1}{\pi} lm \int^{E_F} G_{LL'}^{ii}(\boldsymbol{r}, \boldsymbol{r}', \epsilon)\ d\epsilon, \tag{A.6}$$

where $L = (l,m)$ is the composite index of angular momentum, $i$ is the site index, and $G_{LL'}^{ii}(\boldsymbol{r}, \boldsymbol{r}', \epsilon)$ are Green's functions. The corresponding SIE for an angular momentum channel $L$ at a site $i$ is given as

$$\delta_i = U[\widetilde{n}_L^i] - E_{XC}^{LDA}[\widetilde{n}_L^i]. \tag{A.7}$$

Here, $\widetilde{n}_L^i$ is the normalized orbital charge density of the orbital:

$$\widetilde{n}_L^i = \frac{n_L^i}{p_L^i}, \tag{A.8}$$

where $p_L^i$ is the orbital occupancy

$$p_L^i \equiv \int_{\text{sphere}} n_L^i(\boldsymbol{r})\ d^3r. \tag{A.9}$$

The SIC potential becomes

$$v_L^{\text{PSIC},i} \equiv v^{\text{LDA}}[n] - \frac{1}{2} p_L^i \left( u[\widetilde{n}_i] + v_{XC}^{\text{LDA}}[\widetilde{n}_i] \right) \tag{A.10}$$

where $1/2$ is the pre-scaling factor. The total energy becomes the LDA total energy with a SIE correction for the electron-electron interaction energy and the double-counting of the effective potential energy:

$$E^{\text{PSIC}} = E^{\text{LDA}} - \frac{1}{2} \sum_i \sum_L \int n_L^i(\boldsymbol{r}) v_L^{\text{PSIC},i}(\boldsymbol{r}) d^3r - \sum_i^{\text{occ.}} \delta_i. \tag{A.11}$$

## A.2 Liechtenstein's Formula for an Estimation of Exchange Coupling Constants

In a classical effective Heisenberg model, the magnetic interaction is described as

$$\mathcal{H} = -\frac{1}{2}\sum_{i \neq j} J_{ij}\boldsymbol{e}_i \cdot \boldsymbol{e}_j, \tag{A.12}$$

where $J_{ij}$ is an exchange coupling constant between the local moments at sites $i$ and $j$, and $\boldsymbol{e}_i$ and $\boldsymbol{e}_j$ are the unit vectors that point in the directions of the local moments. The magnitude of the local moments is included in $J_{ij}$. in the Liechtenstein's method [18], to estimate the exchange constants, $J_{ij}$, the energy change caused by a small change in the directions of the local moments at sites $i$ and $j$ is calculated under the condition that all the other moments are fixed. The pair of moments are first supposed to be parallel to each other, then they are tilted in opposite directions by the same amount $\theta/2$. The energy change is

$$\delta\mathcal{H} = J_{ij}\left(1 - \cos\theta\right) \simeq \frac{1}{2}J_{ij}\theta^2. \tag{A.13}$$

The same energy change is evaluated from first-principles calculations using the local force theorem

$$\delta E = \int^{E_{\mathrm{F}}} d\epsilon\,\delta N(\epsilon), \tag{A.14}$$

where $N(\epsilon)$ is the number of electrons and $\delta N(\epsilon)$ is its difference after the rotation of local moments. In multiple scattering theory, the number of electrons $N(\epsilon)$ is given as

$$N(\epsilon) = N_0(\epsilon) + \frac{1}{\pi}\Im\mathrm{Tr}\ln\hat{T}(\epsilon), \tag{A.15}$$

where $N_0(\epsilon)$ is the number of free electrons and $\hat{T}$ is the scattering path operator that describes the scattering by crystal potentials. This operator is symbolically written as

$$\hat{T} = \left(\hat{t}^{-1} - \hat{G}\right)^{-1}. \tag{A.16}$$

where $\hat{t}$ are single-scattering $t$-matrices and $\hat{G}$ are Green's functions. These $\hat{t}$ of sites $i$ and $j$ are then replaced by new $t$-matrices $\hat{t}'$ for the rotated spin moments,

$$\hat{T}' = \left(\hat{t}'^{-1} - \hat{G}\right)^{-1} = \hat{T}\left(1 + \delta\hat{t}^{-1} \cdot \hat{T}\right)^{-1} \tag{A.17}$$

$$\delta\hat{t}^{-1} = \begin{cases} \hat{t}_i'^{-1} - \hat{t}_i^{-1} & (i = 1, 2, \cdots, n) \\ 0 & \text{otherwise} \end{cases} \tag{A.18}$$

Substitution of eqs. (A.14) and (A.15) results in the following expression:

$$\delta E = \frac{1}{\pi} \int^{E_{\mathrm{F}}} d\epsilon \, \Im \mathrm{Tr} \ln\left(1 + \delta\hat{t}^{-1} \cdot \hat{T}\right) \tag{A.19}$$

The $\delta\hat{t}^{-1}$ matrix, the spinor structure of the $t$-matrix is used and described as

$$\hat{t}_i = \frac{1}{2}\left(\hat{t}_{i\uparrow} + \hat{t}_{i\downarrow}\right) \times \hat{1} + \frac{1}{2}\left(\hat{t}_{i\uparrow} - \hat{t}_{i\downarrow}\right) \times (\boldsymbol{e}_i \cdot \hat{\sigma}), \tag{A.20}$$

where $t_{i\uparrow}, t_{i\downarrow}$ are the $t$-matrices for the up and down spin channel, $\boldsymbol{e}_i$ is the direction of the spin moment, and $\hat{\sigma}$ is the Pauli spin matrix. The rotation of the moments is

$$\delta\boldsymbol{e}_\xi = \left(\pm\sin\theta/2, 0, \cos\theta/2 - 1\right), \tag{A.21}$$

and then,

$$\delta\hat{t}_\xi^{-1} = \frac{1}{2}\left(\hat{t}_{\xi\uparrow}^{-1} - \hat{t}_{\xi\downarrow}^{-1}\right) \times (\delta\boldsymbol{e}_\xi \cdot \hat{\sigma}) \tag{A.22}$$

$$= \frac{1}{2}\left(\hat{t}_{\xi\uparrow}^{-1} - \hat{t}_{\xi\downarrow}^{-1}\right) \times \begin{pmatrix} \cos\theta/2 - 1 & \pm\sin\theta/2 \\ \mp\sin\theta/2 & 1 - \cos\theta/2 \end{pmatrix}, \tag{A.23}$$

where $\xi$ represents $i$ or $j$, and the double signs $\pm$ specify the relation between $\xi$ and $i$ or $j$; i.e., plus for $\xi = i$ and minus for $\xi = j$. The energy difference within the second order of $\theta$ is

$$\delta E \simeq \frac{1}{4\pi} \int^{E_{\mathrm{F}}} d\epsilon \, \Im \mathrm{Tr}\left(\Delta_i \hat{T}_\uparrow^{ij} \Delta_j \hat{T}_\downarrow^{ji}\right) \frac{\theta^2}{2} \tag{A.24}$$

where $\Delta_\xi = \hat{t}_{\xi\uparrow}^{-1} - \hat{t}_{\xi\downarrow}^{-1}$. By comparing (A.13) and (A.24), the following relationship is formed,

$$J_{ij} = \frac{1}{4\pi} \int^{E_{\mathrm{F}}} d\epsilon \, \Im \mathrm{Tr}\left(\Delta_i \hat{T}_\uparrow^{ij} \Delta_j \hat{T}_\downarrow^{ji}\right), \tag{A.25}$$

which is known as Liechtenstein's formula [18].

# Acknowledgements

# Reference

[1] S. A. Wolf, D. D. Awschalom, R. A. Buhrman, J. M. Daughton, S. von Molnár, M. L. Roukes, A. Y. Chtchelkanove, and D. M. Treger. "Spintronics: A Spin-based Electronics - Vision for the Future". *Science*, Vol. 294, p. 1488, 2001.

[2] H. Munekata, H. Ohno, S. von Molnar, A. Segmüller, L. L. Chang, and L. Esaki. "Diluted Magnetic III-V Semiconductors". *Phys. Rev. Lett.*, Vol. 63, p. 1849, 1989.

[3] H. Ohno, A. Shen, F. Matsukura, A. Oiwa, A. Endo, S. Katsumoto, and Y. Iye. "(Ga,Mn)As: A New Diluted Magnetic Semiconductor Based on GaAs". *Appl. Phys. Lett.*, Vol. 69, p. 363, 1996.

[4] T. Dietl, H. Ohno, F. Matsukura, J. Cibert, and D. Ferrand. "Zener Model Description of Ferromagnetism in Zinc-blende Magnetic Semiconductors". *Science*, Vol. 287, p. 1019, 2000.

[5] H. Sato and H. Katayama-Yoshida. "Material Design for Transparent Ferromagnets with ZnO-based Magnetic Semiconductors". *Jpn. J. Appl. Phys.*, Vol. 39, p. L555, 2000.

[6] K. Sato and H. Katayama-Yoshida. "Electronic Structure and Ferromagnetism of Transition-metal-impurity-doped Zinc Oxide". *Physica B: Condensed Matter*, Vol. 308-310, p. 904, 2001.

[7] K. Sato and H. Katayama-Yoshida. "Materials Design of Transparent and Half-metallic Ferromagnets in V- or Cr-doped ZnS, ZnSe and ZnTe without P- or N-type Doping Treatment". *Jpn. J. Appl. Phys.*, Vol. 40, p. L651, 2001.

[8] K. Sato and H. Katayama-Yoshida. "Material Design of GaN-based Ferromagnetic Diluted Magnetic Semiconductors". *Jpn. J. Appl. Phys.*, Vol. 40, p. L485, 2001.

[9] K. Sato, P. H. Dederics, and H. Katayama-Yoshida. "Curie Temperatures of III-V Diluted Magnetic Semiconductors Calculated from First principles". *Europhys. Lett.*, Vol. 61, p. 403, 2003.

[10] K. Sato and H. Katayama-Yoshida. "First Principles Materials Design for Semiconductor Spintronics". *Semicond. Sci. Technol.*, Vol. 17, p. 367, 2002.

[11] K. Ueda, H. Tabata, and T. Kawai. "Magnetic and Electric Properties of Transition-metal-doped ZnO Films". *Appl. Phys. Lett.*, Vol. 79, p. 988, 2001.

[12] H. Saeki, H. Tabaka, and T. Kawai. "Magnetic and Electric Properties of Vanadium Doped ZnO Films". *Solid State Commun.*, Vol. 120, p. 439, 2001.

[13] H. Saito, V. Zayets, S. Yamagata, and K. Ando. "Room-Temperature Ferromagnetism in a II-VI Diluted Magnetic Semiconductor $Zn_{1-x}Cr_xTe$". *Phys. Rev. Lett.*, Vol. 90, p. 207202, 2003.

[14] M. Hashimoto, Y. K. Zhou, M. Kanamura, and H. Asahi. "High Temperature (> 400K) Ferromagnetism in III-V-Based Diluted Magnetic Semiconductor GaCrN Grown by ECR Molecular-Beam Epitaxy". *Solid State Commun.*, Vol. 122, p. 37, 2002.

[15] L. Bergqvist, O. Eriksson, J. Kudrnovský, V. Drchal, P. Korzhavyi, and I. Turek. "Magnetic Percolation in Diluted Magnetic Semiconductors". *Phys. Rev. Lett.*, Vol. 93, p. 137202, 2004.

[16] K. Sato, W. Schweika, P. H. Dederichs, and H. Katayama-Yoshida. "Low-temperature ferromagnetism in (Ga, Mn)N: Ab initio calculations". *Phys. Rev. B*, Vol. 70, p. 201202(R), 2004.

[17] T. Fukushima, K. Sato, and H. Katayama-Yoshida. "Theoretical Prediction of Curie Temperature in (Zn,Cr)S, (Zn,Cr)Se and (Zn,Cr)Te by First Principles Calculations". *Jpn. J. Appl. Phys.*, Vol. 43, p. L1416, 2004.

[18] A. I. Liechtenstein, M. I. Katsnelson, V. P. Antropov, and V. A. Gubanova. "Local Spin Density Functional Approach to the Theory of Exchange Interactions in Ferromagnetic Metals and Alloys". *J. Magn. Magn. Mater.*, Vol. 67, p. 65, 1987.

[19] K. Binder and D. W. Heermann. *Monte Carlo Simulation in Statistical Physics*. Springer, Berlin, Heidelberg, New York, 2002.

[20] K. Sato, L. Bergqvist, J. Kudrnovský, P. H. Dederichs, O. Eriksson, I. Turek, B. Sanyal, G. Bouzerar, H. Katayama-Yoshida, V. A. Dinh, T. Fukushima, H. Kizaki, and R. Zeller. "First-Principles Theory of Dilute Magnetic Semiconductors". *Rev. Mod. Phys.*, Vol. 82, p. 1633, 2010.

[21] M. L. Reed, N. A. El-Masry, H. H. Stadelmaier, M. K. Ritums, M. J. Reed, C. A. Parker, J. C. Roberts, and S. M. Bedair. "Room Temperature Ferromagnetic Properties of (Ga, Mn)N". *Appl. Phys. Lett.*, Vol. 79, p. 3473, 2001.

[22] H. Hori, S. Sonoda, T. Sasaki, Y. Yamamoto, S. Shimizu, K. Suga, and K. Kindo. "High-$T_C$ Ferromagnetism in Diluted Magnetic Semiconducting GaN:Mn films". *Physica B: Condensed Matter*, Vol. 324, p. 142, 2002.

[23] M. Zając, R. Doradziński, J. Gosk, J. Szczytko, M. Lefeld-Sosnowska, M. Kamińska, A. Twardowski, M. Palczewska, E. Grzanka, and W. Gębicki. "Magnetic and Optical Properties of GaMnN Magnetic Semiconductor". *Appl. Phys. Lett.*, Vol. 78, p. 1276, 2001.

[24] K. Ando. "Magneto-optical Studies of s,p-d Exchange Interactions in GaN:Mn with Room-Temperature Ferromagnetism". *Appl. Phys. Lett.*, Vol. 82, p. 100, 2003.

[25] A. Aharoni. *Introduction to the Theory of Ferromagnetism*. Oxford University Press, 2000.

[26] K. Sato, H. Katayama-Yoshida, and P. H. Dederichs. "High Curie Temperature and Nano-Scale Spinodal Decomposition Phase in Dilute Magnetic Semiconductors". *Jpn. J. Appl. Phys.*, Vol. 44, p. L948, 2005.

[27] T. Fukushima, K. Sato, H. Katayama-Yoshida, and P. H. Dederichs. "Spinodal Decomposition under Layer by Layer Growth Condition and High Curie Temperature Quasi-One-Dimensional Nano-Structure in Dilute Magnetic Semiconductors". *Jpn. J. Appl. Phys.*, Vol. 45, p. L416, 2006.

[28] K. Sato, T. Fukushima, and H. Katayama-Yoshida. "Super-Paramagnetic Blocking Phenomena and Room-Temperature Ferromagnetism in Wide Band-Gap Dilute Magnetic Semiconductor (Ga, Mn)N". *Jpn. J. Appl. Phys.*, Vol. 46, p. L682, 2007.

[29] L. Gu, S. Y. Wu, H. X. Liu, R. K. Singh, N. Newman, and D. J. Smith. "Characterization of Al(Cr)N and Ga(Cr)N Dilute Magnetic Semiconductors". *J. Magn. Magn. Mater.*, Vol. 290-291, p. 1395, 2005.

[30] M. Jamet, A. Barski, T. Devillers, V. Poydenot, R. Dujardin, P. Bayle-Guillemaud, J. Rothman, E. Bellet-Amalric, A. Marty, J. Cibert, R. Mattana,

and S. Tatarenko. "High-Curie-Temperature Ferromagnetism in Self-Organized $Ge_{1-x}Mn_x$ Nanocolumns". *Nat. Mater.*, Vol. 5, p. 653, 2006.

[31] S. Kuroda, N. Nishizawa, K. Takita, M. Mitome, Y. Bando, K. Osuch, and T. Dietl. "Origin and Control of High-Temperature Ferromagnetism in Semiconductors". *Nat. Mater.*, Vol. 6, p. 440, 2007.

[32] M. Toyoda, H. Akai, K. Sato, and H. Katayama-Yoshida. "Electronic Structures of (Zn,V)O and (Zn,Co)O in the Self-Interaction- Corrected Calculation". *Physica B*, Vol. 376, p. 647, 2006.

[33] J. P. Perdew and A. Zunger. "Self-Interaction Correction to Density-Functional Approximations for Many-Electron Systems". *Phys. Rev. B*, Vol. 23, p. 5048, 1981.

[34] A. Filippetti and N. A. Spaldin. "Self-interaction-Corrected Pseudopotential Scheme for Magnetic and Strongly-Correlated Systems". *Phys. Rev. B*, Vol. 67, p. 125109, 2003.

[35] M. Seike, A. Yanase, K. Sato, and H. Katayama-Yoshida. "Materials Design of $4d$-Transition-Metal-Doped Transparent and Half-Metallic Ferromagnets with $K_2S$-Based Diluted Magnetic Semiconductors". *Jpn. J. Appl. Phys.*, Vol. 42, p. L1061, 2003.

[36] M. Seike, K. Sato, A. Yanase, and H. Katayama-Yoshida. "Design of Transparent, Half-Metallic Ferromagnetic $4d$-Transition-Metal-Doped $K_2S$ with High Curie Temperature". *Jpn. J. Appl. Phys.*, Vol. 43, p. 3367, 2004.

[37] M. Seike, K. Sato, A. Yanase, and H. Katayama-Yoshida. "Material Design of Transparent, Half-Metallic and Room-Temperature Ferromagnets in $I_2$-VI Semiconductors with $4d$ Transition Metal Element". *Jpn. J. Appl. Phys.*, Vol. 43, p. L834, 2004.

[38] H. Yoshida, M. Seike, K. Sato, and A. Yanase. "Transparent Ferromagnetic Alkali/Chalcogenide Compound Comprising Solid Solution of Transition Metal and Method of Regulating Ferromagnetism Thereof". P2003-127602, WO2004/097081 A1, US 2006/0231789 A1.

[39] M. Seike, K. Kenmochi, K. Sato, A. Yanase, and H. Katayama-Yoshida. "New Route to Fabricate Ferromagnetic Semiconductors without Transition Metal Elements". *Jpn. J. Appl. Phys.*, Vol. 43, p. L579, 2004.

[40] K. Kenmochi, M. Seike, K. Sato, K. Sato, and H. Katayama-Yoshida. "New Class of Diluted Ferromagnetic Semiconductors based on CaO without Transition Metal Elements". *Jpn. J. Appl. Phys.*, Vol. 43, p. L934, 2004.

[41] H. Yoshida, K. Kenmochi, M. Seike, K. Sato, and A. Yanase. "Transparent Ferromagnetic Compound Containing no magnetic impurity such as transition metal or rare earth metal and forming solid solution with element having imperfect shell, and method for adjusting ferromagnetic characteristics thereof". P2004-55017, WO2005/083161 A1, P2006-510484(registered in Japan, 2011.3.25), US 2007/0178032 A1.

[42] K. Kenmochi, V. A. Dinh, K. Sato, A. Yanase, and H. Katayama-Yoshida. "Materials Design of Transparent and Half-Metallic Ferromagnets of MgO, SrO and BaO without Magnetic Elements". *J. Phys. Soc. Jpn.*, Vol. 73, p. 2952, 2004.

[43] H. Katayama-Yoshida, K. Sato, M. Toyoda, V. A. Dinh, T. Fukushima, and H. Kizaki. *A New Class of Dilute Magnetic Semiconductors without Transition Metal Elements*, pp. 60–71. Pan Stanford Publishing Pte. Ltd, Singapore, 2010.

[44] V. A. Dinh, K. Sato, and H. Katayama-Yoshida. "Dilute magnetic semiconductors based on wide bandgap $SiO_2$ with and without transition metal elements". *Solid State Commun.*, Vol. 136, p. 1, 2005.

[45] K. Kenmochi, K. Sato, A. Yanase, and H. Katayama-Yoshida. "Materials Design of Ferromagnetic Diamond". *Jpn. J. Appl. Phys.*, Vol. 44, p. L51, 2005.

[46] J. M. D. Coey. "$d^0$ Ferromagnetism". *Solid State Sci.*, Vol. 7, p. 660, 2005.

[47] A. L. Ivanovskii. "Magnetic Effects Induced by *sp* Impurities and Defects in Nonmagnetic *sp* Materials". *Phys. Usp.*, Vol. 50, p. 1031, 2007.

[48] O. Volnianska and P. Boguslawski. "Origin of $d^0$ Magnetism in II-VI and III-V Semiconductors by Substitutional Doping at Anion Site". *J. Phys.: Condens. Matter*, Vol. 22, p. 073202, 2010.

[49] K. Yang, R. Wu, L. Shen, Y. P. Feng, Y. Dai, and B. Huang. "Magnetism of Solids Resulting From Spin Polarization of *p* Orbitals". *Phys. Rev. B*, Vol. 81, p. 125211, 2010.

[50] C.-H. Yang, M. Samant, and S. Parkin. "Ferromagnetism in MgO by Nitrogen Doping". *APS March Meeting Abstract*, Vol. p. V22.00004, p. (/http://meetings.Aps.org/Meeting/MAR09/Event/98745S), 2009.

[51] H. Pan, J. B. Yi, L. Shen, R. Q. Wu, J. H. Yang, J. Y. Lin, Y. P. Feng, J. Ding, L. H. Van, and J. H. Yin. "Room-Temperature Ferromagnetism in Carbon-Doped ZnO". *Phys. Rev. Lett.*, Vol. 99, p. 127201, 2007.

[52] C.-F. Yu, T.-J. Lin, S.-J. Sun, and H. Chou. "Origin of Ferromagnetism in Nitrogen Embedded ZnO : N Thin Films". *J. Phys. D*, Vol. 40, p. 6497, 2007.

[53] M. Venkatesan, C. B. Fitzgerald, and J. M. D. Coey. "Unexpected Magnetism in a Dielectric Oxide". *Nature*, Vol. 430, p. 630, 2004.

[54] N. H. Hong, J. Sakai, N. Poirot, and V. Brizé. "Room-Temperature Ferromagnetism Observed in Undoped Semiconducting and Insulating Oxide Thin Films". *Phys. Rev. B*, Vol. 73, p. 132404, 2006.

[55] N. H. Hong, N. Poirot, and J. Sakai. "Ferromagnetism Observed in Pristine $SnO_2$ Thin Films". *Phys. Rev. B*, Vol. 77, p. 033205, 2008.

[56] M. Seike, K. Sato, K. Sato, and H. Katayama-Yoshida. "The Magnetic Properties of Hole-Doped MgO". *Jpn. J. Appl. Phys.*, Vol. 50, p. 090204, 2011.

[57] M. Seike, V. A. Dinh, K. Sato, K. Sato, and H. Katayama-Yoshida. "First-principles Study of the Magnetic Properties of Nitrogen-Doped Alkaline Earth Metal Oxides". *to be published in Physica B*, p. DOI: 10.1016/j.physb.2011.08.044, 2011.

[58] M. Seike, V. A. Dinh, T. Fukushima, K. Sato, and H. Katayama-Yoshida. "Spinodal Nanodecomposition and High Blocking Temperature in MgO-based $d^0$ Ferromagnets". APEX (submitted).

[59] K. Momma and F. Izumi. "VESTA 3 for Three-Dimensional Visualization of Crystal, Volumetric and Morphology Data". *J. Appl. Crystallogr.*, Vol. 44, p. 1272, 2011.

[60] H. Akai and P. H. Dederichs. "Local Moment Disorder in Ferromagnetic Alloys". *Phys. Rev. B*, Vol. 47, p. 8739, 1993.

[61] H. Akai. "Ferromagnetism and Its Stability in the Diluted Magnetic Semiconductor (In,Mn)As". *Phys. Rev. Lett.*, Vol. 81, p. 3002, 1998.

[62] H. Akai. "http://sham.phys.sci.osaka-u.ac.jp/kkr/".

# Reference

[63] P. Mavropoulos, M. Ležaić, and S. Blügel. "Ferromagnetism in Nitrogen-Doped MgO: Density-Functional Calculations". *Phys. Rev. B*, Vol. 80, p. 184403, 2009.

[64] D. P. Young, D. Hall, M. E. Torelli, Z. Fisk, J. L. Sarrao, J. D. Thompson, H.-R. Ott, S. B. Oseroff, R. G. Goodrich, and R. Zysler. "High-Temperature Weak Ferromagnetism in a Low-Density Free-Electron Gas". *Nature*, Vol. 397, p. 412, 1999.

[65] K. Matsubayashi, M. Maki, T. Tsuzuki, T. Nishioka, and N. K. Sato. "Magnetic properties (Communication arising): Parasitic Ferromagnetism in a Hexaboride?". *Nature*, Vol. 420, p. 143, 2002.

[66] I. S. Elfimov, S. Yunoki, and G. A. Sawatzky. "Possible Path to a New Class of Ferromagnetic and Half-Metallic Ferromagnetic Materials". *Phys. Rev. Lett.*, Vol. 89, p. 216403, 2002.

[67] The Chemical Society of Japan. *Kagakubinran Kisohen, fourth ed.* Maruzen, Tokyo, 1993.

[68] S. S. P. Parkin, C. Kaiser, A. Panchula, P. M. Rice, B. Hughes, M. Samant, and S.-H. Yang. "Giant Tunnelling Magnetoresistance at Room Temperature with MgO (100) Tunnel Barriers". *Nat. Mater.*, Vol. 3, p. 862, 2004.

[69] V. A. Dinh, M. Toyoda, K. Sato, and H. Katayama-Yoshida. "Exchange Interaction and $T_C$ in Alkaline-Earth-Metal-Oxide-Based DMS without Magnetic Impurities: First Principle Pseudo-SIC and Monte Carlo Calculation". *J. Phys. Soc. Jpn.*, Vol. 75, p. 093705, 2006.

[70] G. Kresse and D. Joubert. "From Ultrasoft Pseudopotentials to the Projector Augmented-Wave Method". *Phys. Rev. B*, Vol. 59, p. 1758, 1999.

[71] J. P. Perdew and W. Yue. "Accurate and Simple Density Functional for the Electronic Exchange Energy: Generalized Gradient Approximation". *Phys. Rev. B*, Vol. 33, p. 8800, 1986.

[72] J. P. Perdew, K. Burke, and M. Ernzerhof. "Generalized Gradient Approximation Made Simple". *Phys. Rev. Lett.*, Vol. 77, p. 3865, 1996.

[73] G. Kresse and J. Furthmüller. "Efficient Iterative Schemes for ab initio Total-Energy Calculations Using a Plane-Wave Basis Set". *Phys. Rev. B*, Vol. 54, p. 11169, 1996.

[74] G. Kresse and J. Furthmüller. "Efficiency of ab-initio Total Energy Calculations for Metals and Semiconductors Using a Plane-Wave Basis Set". *Comput. Mater. Sci.*, Vol. 6, p. 15, 1996.

[75] D. A. Dimitrov and G. M. Wysin. "Magnetic Properties of Superparamagnetic Particles by a Monte Carlo Method". *Phys. Rev.*, Vol. B 54, p. 9237, 1996.

[76] C. Martínez-Boubeta, J. I. Beltrán, L. I. Balcells, Z. Konstantinović, S. Valencia, D.Schmitz, J.Arbiol, S.Estrade, J.Cornil, and B.Martínez. "Ferromagnetism in Transparent thin Films of MgO". *Phys. Rev. B*, Vol. 82, p. 024405, 2010.

[77] C. M. Araujo, M. Kapilashrami, X. Jun, O. D. Jayakumar, S. Nagar, Y.Wu, C. Århammar, B. Johansson, L. Belova, R. Ahuja, and G. A. Gehring andK. V. Rao. "Room Temperature Ferromagnetism in Pristine MgO Thin Films". *Appl. Phys. Lett.*, Vol. 96, p. 232505, 2010.

# List of Publications

## L.1 Paper

1. M. Seike, V. A. Dinh, T. Fukushima, K. Sato, and H. Katayama-Yoshida, "Self-Organized Nanostructures and High Blocking Temperature in MgO-based $d^0$ Ferromagnets" (submitted).

2. M. Seike, V. A. Dinh, K. Sato, H. Katayama-Yoshida, "First-Principles Study of the Magnetic Properties of Nitrogen-Doped Alkaline Earth Metal Oxides", *to be published in Physica B*

   [DOI: 10.1016/j.physb.2011.08.044].

3. M. Seike, K. Sato, and H. Katayama-Yoshida, "The Magnetic Properties of Hole-Doped MgO", Jpn. J. Appl. Phys. Vol. 50, p. 090204, 2011.

4. M. Seike, T. Saitou, Y. Kouchi, T. Ohara, M. Matsuhisa, K. Sakaguchi, K. Tomita, K. Kosugi, A. Kashiwagi, M. Kasuga, M. Tomita, Y. Naito, H. Nakajima, "Computational Assessment of Insulin Secretion and Insulin Sensitivity From 2-h Oral Glucose Tolerance Tests for Clinical Use for Type 2 Diabetes", *J. Physiol. Sci.*, Vol. 61, p. 321, 2011.

5. M. Seike and K. Sakaguchi, "Diabetes Systems Biology", *Diabetes Frontier* Vol. 21 No.2, p. 171, 2010.

6. J. Lu, M. Seike, W. Liu, P. Wu, L. Wang, Y. Wu, Y. Naito, H. Nakajima and Y. Kouchi, "Extrapolation of Clinical Data from an Oral Glucose Tolerance Test Using a Support Vector Machine", *World Academy of Science, Engineering and Technology, Conf. Proc.*, Issue 53, p. 1271, May 2009.

7. K. Kemmochi, M. Seike, K. Sato, A. Yanase and H. Katayama-Yoshida, "New Class of High-$T_C$ Diluted Ferromagnetic Semiconductors Based on CaO without Transition Metal Elements", *J. Supercond.*, Vol. 18, p. 37, 2005.

8. M. Seike, K. Kenmochi, K. Sato, A. Yanase and H. Katayama-Yoshida, "New Class of High-Tc Diluted Ferromagnetic Semiconductors Based on $K_2S$ without Transition Metal Elements", *AIP Conf. Proc.*, Vol. 772, p. 317, 2005.

9. M. Seike, K. Sato, A. Yanase and H. Katayama-Yoshida, "Design of Transparent, Half-Metallic Ferromagnetiic 4d-Transition-Metal-Doped K2S with High Curie Temperature", *Jpn. J. Appl. Phys.*, Vol. 43, p. 3367, 2004.

10. K. Kenmochi, M. Seike, K. Sato, A. Yanase and H. Katayama-Yoshida, "New Class of Diluted Ferromagnetic Semiconductors based on CaO without Transition Metal Elements", *Jpn. J. Appl. Phys.*, Vol. 43, p. L934, 2004.

11. M. Seike, K. Sato, A. Yanase and H. Katayama-Yoshida, "Materials Design of Transparent, Half-Metallic and Room-Temperature Ferromagnets in $I_2$-VI Semiconductors with $4d$ Transition Metal Element", *Jpn. J. Appl. Phys.*, Vol. 43, p. L834, 2004.

12. M. Seike, K. Kenmochi, K. Sato, A. Yanase and H. Katayama-Yoshida, "New Route to Fabricate Ferromagnetic Semiconductors without Transition Metal Elements", *Jpn. J. of Appl. Phy.*, Vol. 43, p. L579, 2004.

13. M. Shirai, M. Seike, K. Sato, H. Katayama-Yoshida, "Theoretical Study on Anti-Site Defects in Half-Metallic Zinc-Blend Ferromagnets", *J. Magn. Magn. Matt.*, Vol. 272, p. 344, 2004.

14. M. Seike, A. Yanasse, K. Sato and H. Katayama-Yoshida, "Materials Design of 4d-Transition-Metal-Doped Transparent and Half-Metallic Ferromagnets with $K_2S$-Based Diluted Magnetic Semiconductors", *Jpn. J. Appl. Phys.*, Vol. 42, p. L1061 (2003).

15. K. Takai, M. Seike, K. Tanaka and Y. Hayafuji, "New Pseudo-Binary Titanium Silicide Systems for Lowering Phase Transformation Temperature", *Adv. in Quantum Chem.*, Vol. 42, p. 239 (2003).

## L.2   International Conference

1. M. Seike, T. Fukuchima, K. Sato and H. Katayama-Yoshida, "Defect-Induced High-$T_C$ Ferromagnetism and Spinodal Nanodecomposition in MgO", APS March Meeting 2012, Boston, US, Feb. 27 - Mar. 2, 2012.

2. M. Seike, P. Wu, W. Liu, L. Wang, X. Teng, J. Lu, Y. Kouchi, Y. Naito, H. Nakajima, "Mathematical Model-based Prediction of Responders to Biguanides or Glinides in Type 2 Diabetes Patients", World Diabetes Congress 2011 (IDF 2011), Dubai, United Arab Emirates, Dec. 4-8, 2011.

3. M. Seike, P. Wu, W. Liu, L. Wang, X. Teng, J. Lu, Y. Kouchi, Y. Naito, H. Nakajima, "Prediction of Responders to Oral Hypoglycemic Agents in Type 2 Diabetes Patients using a Mathematical Model", The 12th International Conference on Systems Biology, Heidelberg/Mannheim, Germany, Aug.28-Sep.1, 2011.

4. M. Seike, K. Sato and H. Katayama-Yoshida, "The Origin of the Magnetism in Undoped MgO", E-MRS 2011 Fall Meeting, Warsaw, Poland, Sep.19-23, 2011.

5. M. Seike, V. A. Dinh, K. Sato and H. Katayama-Yoshida, "First-Principles Study of the Magnetic Properties of Nitrogen-doped Alkaline Earth Metal Oxides", The 26th International Conference on Defects in Semiconductors (ICDS-26), Nelson, New Zealand, July 17 22, 2011.

6. . Seike, M. Matsuhisa, Y. Tashima, J. Lu, Y. Kouchi, Y. Naito, K. Sakaguchi, K. Tomita, K. Kosugi, H. Nakajima, A. Kashiwagi, "Demonstration of a Mathematical Model Predicting the Splanchnic Glucose Output: Evaluation by Glucose Clamp", American Diabetes Association, The 70th Scientific Sessions, Florida, USA, June 25-30 (2010).

7. M. Seike, "Modelling for Diagnostics Application: Diversity of disease states", Building the VPH Community Satellite Symposium of IUPS 2009, Shiga, Japan, July 26, 2009 (Invited).

8. M. Seike, T. Saitou, Y. Kouchi, Y. Naito and H. Nakajima, "A Mathematical Model for Estimating Pathophysiologic Conditions and Supporting Decision of Optimaized Therapeutic Strategies in the Treatment of Type 2 Diabetes", American Diabetes Association The 69th Scientific Sessions, New Orleans, USA, June 5-9, 2009.

9. J. Lu, M. Seike, W. Liu, P. Wu, L. Wang, Y. Wu, Y. Naito, H. Nakajima and Y. Kouchi, "Extrapolation of Clinical Data from an Oral Glucose Tolerance Test Using a Support Vector Machine", International Conference on Computer, Electrical, and Systems Science, and Engineering, Tokyo, Japan, May 26-28, 2009.

10. M. Seike, T. Saito, T. Takahata, Y. Kouchi, Y. Naito, H. Nakajima and K. Asano, "Reproduction of Drug Effect by the Use of Diabetes Management System", MBI workshop 7, Ohio, USA, May 21-24, 2007.

11. M. Seike, T. Saitou, Y. Kouchi, K. Asano, T. Ohara, Y. Naito, H. Nakajima, "Diabetes Management System Based on Systems Biology Aimed at Offering a Therapeutic Strategy for Each Patient", The 7th International Conference on Systems Biology, Yokohama Japan, Oct. 9-11 2006.

12. K. Kemmochi, M. Seike, V. A. Dinh, K. Sato, A. Yanase, H. Katayama-Yoshida, "Materials Design of Transparent and Half-Metallic Ferromagnetic Semiconductors without Transition Metal Elements", 3rd International School and Conference on Spintronics and Quantum Information Technology (Spintech III), Awaji, Japan, August 1-5, 2005.

13. M. Seike, K. Kenmochi, K. Sato, A. Yanase, H. Katayama-Yoshida, "New class of High-$T_C$ Diluted Ferromagnetic Semiconductors Based on K2S without Transition Metal Elements", The 27th International Conference on the Physics of Semiconductors (ICPS-27), Flagstaff, Arizona, USA, July 26-30, 2004.

14. K. Kenmochi, M. Seike, K. Sato, A. Yanase, H. Katayama-Yoshida, "New Class of high-$T_C$ Diluted Ferromagnetic Semiconductors Based on CaO without Transition Metal Elements", The 3rd International Conference on Physics and Applications of Spin-Related Phenomena in Semiconductors (PASPS-III), Santa Barbara, California, USA, July 21-23, 2004.

15. M. Seike, A. Yanase, K. Sato and H. Katayama-Yoshida, "Design of High-$T_C$ Curie Temperature with Transparent and Half Metallic Ferromagnetism in Zr and Nb-doped $K_2S$ Diluted Magnetic Semiconductors", International Symposium on Scientific and Industrial Nanotechnology 2003, Osaka, Japan, Dec. 8-9, 2003.

16. M. Seike, A. Yanase, K. Sato and H. Katayama-Yoshida, "Materials Design of 4$d$-transition-metal Doped $K_2S$ Diluted Magnetic Semiconductors with Transparent and Half-metallic", SPINTECH2: International Conference and School Semiconductor Spintronics and Quantum Information Technology, Brugge, Belgiujm, Aug. 4-8, 2003.

17. M. Shirai, M. Seike, K. Sato and H. Katayama-Yoshida, "Theoretical Study on Anti-site Defects in Half-metallic Zinc-blende Ferromagnets", International Conference on Magnetism (ICM2003), Roma, Italy, Jul. 27-Aug.1, 2003.

18. M. Shirai, M. Seike, K. Sato, H. Katayama-Yoshida, "Effects of Anti-site Defects on Half-metallicity in Zinc-blends CrAs", The 9th Symposium on the Physics and Application of Spin-Related Phenomena in Semiconductors (PASPS-9), Tokyo, Japan, Jun. 11-12, 2003.

19. M. Seike, A. Yanase, K. Sato and H. Katayama-Yoshida, "Materials Design of 4d-Transition-Metal Doped Transparent and Half-metallic Ferromagnetism with Diluted Magnetic Semiconductors in Anti-CaF$_2$ structures of K$_2$S", The 9th Symposium on the Physics and Application of Spin-Related Phenomena in Semiconductors (PASPS-9), Tokyo, Japan, Jun. 11-12, 2003.

## L.3   Patent

1. H. Yoshida, K. Kenmochi, M. Seike, K. Sato, A. Yanase: Transparent Ferromagnetic Compound Containing no magnetic impurity such as transition metal or rare earth metal and forming solid solution with element having imperfect shell, and method for adjusting ferromagnetic characteristics thereof. P2004-55017, WO2005/083161 A1, P2006-510484(registered, 2011), US 2007/0178032 A1.

2. H. Yoshida, M. Seike, K. Sato, A. Yanase: Transparent Ferromagnetic Alkali / Chalcogenide Compound Comprising Solid Solution of Transition Metal and Method of Regulating Ferromagnetism Thereof. P2003-127602, WO2004/097081 A1, US 2006/0231789 A1.